

**Reciprocity between Emission and Absorption for Rare Earth
Ions in Glass**

by

Rodica M. Martin

A Dissertation

Submitted to the Faculty

of the

WORCESTER POLYTECHNIC INSTITUTE

In partial fulfillment of the requirements for the

Degree of Doctor of Philosophy

in

Physics

April 25, 2006

APPROVED:

Professor Richard S. Quimby, WPI - Major Thesis Advisor

Professor Thomas H. Keil, WPI

Professor Cosme Furlong-Vazquez, WPI

*To my parents,
who have given me everything they could possibly give
and to whom there is no way of repaying back.*

Acknowledgements

There are so many people who helped me along the way, and contributed to this unique chapter in my life, to whom I am so thankful and indebted.

First of all, I would like to thank my advisor Professor Richard S. Quimby, for his wonderful guidance and support during these years. It was a great experience to be his student, and I have learned so much about the experimental physics and the techniques involved in photonics experiments. His assistance, patience and encouragement have led me constantly throughout this work.

I would also like to thank WPI and Physics Department, especially the two department heads, John Norbury and Thomas Keil for providing financial support. Special thanks go to Professor Keil and Professor Cosme Furlong-Vazquez for serving in my thesis committee.

I am also very thankful to many professors in Physics Department with whom I interacted during my studies at WPI and who contributed enormously to my development as graduate student. They were my directed research advisors, course professors or professors for whom I was a TA, and everything I know it is a blend of what I learned from each of them. I mention here Prof. N. A. Burnham, Prof. G. S. Iannacchione, Prof. P. K. Aravind, Prof. G. D. Phillips, Prof. A. Zozulya and Prof. R. Garcia.

I appreciate all the help that I received from our secretaries Jackie Malone and Earline Rich during these years at WPI, not only regarding administrative aspects, but

also valuable advice I needed at any time. I would also like to thank Roger Steele for providing experimental supplies for my experiments, and Fred Hutson for his assistance with the freshmen labs.

On a personal level, I would like to thank my friends Lumi and Calin, Dana and Adi, Margareta and Florin, Maria and Mircea, for their support and help, especially during this last year while I was in Florida.

I would like to thank my parents for their unbounded love and support, and also my brother and my sister for their encouragements, honesty and trust.

Most of all, I thank the most special people in my life, my loving husband Catalin and my wonderful daughter Andreea, for their unconditioned love, support and understanding during these years. There are no words that can describe how thankful I am for having you along at my side in this journey.

Above all, I thank God for strengthening me every day to overcome myself, and pursue in achieving this dream.

Abstract

The power of the McCumber theory [D. E. McCumber, Phys. Rev. **136**, A954-957 (1964)] consists in its ability to accurately predict emission cross section spectra from measured absorption, and vice versa, including both absolute values and spectral shapes. While several other theories only allow the determination of integrated cross sections, the McCumber theory is unique in generating the spectral shape of a cross section without any direct measurements regarding that cross section. The present work is a detailed study of the range of validity of the McCumber theory, focussing particularly on those aspects that most critically affect its applicability to transitions of rare earth ions in glasses. To analyze the effect of the spectral broadening on the accuracy of the technique, experiments were performed at room and low temperature. The theory was tested by comparing the cross sections calculated using the McCumber relation with those obtained from measurements. At room temperature, a number of ground state transitions of three different rare earth ions (Nd, Er and Tm) in oxide and fluoride glass hosts have been studied. Special attention was paid to the consistency of the measurements, using the same experimental setup, same settings and same detection system for both absorption and fluorescence measurements. Other aspects of the experimental procedure that could generate systematic errors, like fluorescence reabsorption and baseline subtraction uncertainties in the absorption measurements, were carefully investigated. When all these aspects are properly accounted for, we find in all cases an excellent agree-

ment between the calculated and the measured cross section spectra. This suggests that the McCumber theory is not limited to crystallinne hosts, but describes quite well the reciprocity between emission and absorption for the broader transitions of rare earths in glassy hosts.

This good agreement does not hold, however, for the low temperature results. The distortion observed in this case follows the theoretically predicted behavior, and corresponds to the amplification of the gaussian wings that describes the inhomogeneous type of broadening. Our results suggest that the McCumber theory must be used with caution for temperatures below 200 K.

Contents

1	Introduction	2
2	Theoretical background	12
2.1	Interaction between light and atomic systems	13
2.1.1	Broadband excitation: Einstein A and B coefficients	15
2.1.2	Narrowband excitation. Transition rates	18
2.2	Gain in active media	20
2.3	Optical properties of rare earth ions in fluoride and silicate glasses	23
2.3.1	General Characteristics	24
2.3.2	Intensities of optical transitions	27
2.3.3	Spectral shape of the 4f-4f transitions	30
3	Relationship between absorption and stimulated emission cross sections	35
3.1	Judd-Ofelt theory	36
3.1.1	Determination of the Judd-Ofelt parameters using standard fitting procedure	37
3.1.2	Analytical determination of Judd-Ofelt parameters including branching ratios	38
3.2	Fuchtbauer-Ladenburg (FL) theory	42

3.2.1	Derivation of the FL relation	42
3.2.2	Equivalent forms of the FL relation	43
3.3	McCumber theory	47
3.3.1	Generalization of Einstein relations for broadband spectra	47
3.3.2	Range of validity of the McCumber theory	53
4	Experimental method used for room temperature measurements	60
4.1	Emission cross section measurements	61
4.2	Absorption cross section measurements	62
4.3	Experimental setup	63
4.3.1	Experimental setup for fluorescence measurements	64
4.3.2	Experimental setup for absorption measurements	74
5	Experimental investigations of the validity of the McCumber theory at room temperature	76
5.1	<i>Nd</i> ³⁺ doped samples	77
5.1.1	Nd:silicate glass	78
5.1.2	Nd:fluorozirconate glass	87
5.2	<i>Tm</i> ³⁺ doped samples	91
5.2.1	Tm:fluorozirconate glass	92
5.2.2	Tm:fluorophosphate glass	98
5.2.3	Tm:silicate glass	102
5.3	<i>Er</i> ³⁺ doped samples	104
5.3.1	Er:silicate glass	106
5.3.2	Er:fluorozirconate glass	110

6 Low temperature study of the McCumber theory	116
6.1 Expectations	116
6.1.1 Single peak distortion	117
6.1.2 Multiple peak distortion	121
6.2 Experimental setup	129
6.3 Measurements and results	133
6.3.1 Nd:fluorozirconate sample	134
6.3.2 Nd:silicate sample	140
6.4 Quantitative analysis	144
6.4.1 Exploring the peak shift	144
6.4.2 Exploring the critical points of the distortion function	146
6.4.3 Modeling the spectral shape by fitting with a function describing the type of broadening	148
7 Concluding remarks and Future directions	156
7.1 Concluding remarks	156
7.2 Future directions	161
A Time-dependent perturbation theory. Absorption and stimulated emis- sion transition rates.	163
A.1 Electric Dipole Interaction	164
A.2 Magnetic Dipole Interaction	170

List of Figures

2.1	Absorption, stimulated emission and spontaneous decay	14
2.2	Blackbody Spectrum Compared to a Typical Lorentzian Linefunction for RE in Glass	16
2.3	Light Amplification in a Gain Medium	21
2.4	The Hamiltonian of Rare Earth Ions in Solids	26
2.5	Gaussian and Lorentzian functions	33
3.1	Branching Ratios Representation	39
3.2	McCumber Diagram	48
3.3	Spectral shape of absorption and emission cross sections	55
3.4	Distortion of a Lorentzian and Gaussian lineshape functions	58
4.1	Experimental setup for emission	65
4.2	Optimum slit widths of the monochromator	67
4.3	Beam diameter	70
4.4	Positioning the filament with the lasers	72
4.5	Calibration of the color temperature of the filament	73
4.6	Experimental setup for absorption	75
5.1	Nd energy levels	78
5.2	Effect of sample tilt on measured absorption	80

5.3	Effect of baseline subtraction on the calculated emission spectrum at 890 nm in Nd:silicate	81
5.4	Scattering and reabsorption of light at the edge of the sample	83
5.5	Effect of scattering and reabsorption of light on the measured fluorescence spectrum	84
5.6	Effect on the BB correction on measured fluorescence	85
5.7	Comparation between calculated and measured spectra for NdSilicate glass	86
5.8	Determination of the absorption cross section for NdZBLAN	88
5.9	Description of the fluorescence reabsorption	89
5.10	Illustration of the effect of reabsorption on the fluorescence spectrum . .	90
5.11	Comparation between calculated and measured cross section spectra for Nd:fluorozirconate sample	92
5.12	Energy level diagram for the low-lying levels of Tm^{3+}	93
5.13	Absorption spectrum for Tm^{3+} in fluorozirconate glass.	94
5.14	Effect of the different baseline fit curves on the calculated emission cross section spectra in Tm:fluorozirconate sample	95
5.15	Fluorescence reabsorption in Tm:fluorozirconate glass	96
5.16	Comparison between the calculated and measured cross section spectra for Tm:fluorozirconate sample pumped at 784 nm	97
5.17	Comparison between the calculated and measured cross section spectra for Tm:fluorozirconate sample pumped at 808 nm	98
5.18	Effect of the different long wavelength tails of the absorption cross section on the calculated spectra for Tm:fluorophosphate sample	99
5.19	Illustration of the effect of reabsorption on the fluorescence spectrum of Tm in fluorophosphate glass.	100

5.20 Effect of the fluorescence reabsorption on the calculated emission cross section spectrum of Tm in fluorophosphate glass.	101
5.21 Comparison between calculated and measured cross section spectra for Tm:fluorophosphate	102
5.22 Comparison between calculated and measured cross section spectra for Tm:silicate	103
5.23 Fluorescence reabsorption in Tm:silicate	104
5.24 Effect of the reabsorption on the calculated absorption cross section in Tm:silicate	105
5.25 Er energy levels	106
5.26 Determination of measured absorption spectra for Er:silicate	107
5.27 Fluorescence reabsorption in Er:silicate	109
5.28 Comparison of calculated and measured absorption spectra for the 1550 nm in Er:silicate	110
5.29 Effect of the background choice on the calculated emission for the 1550 nm transition in Er:fluorozirconate glass	111
5.30 Fluorescence reabsorption at 1550 nm in Er:fluorozirconate glass	112
5.31 Determination of measured absorption spectra for Er:fluorozirconate	113
5.32 Comparison between calculated and measured cross sections for the 1550 nm transition in fluorozirconate glass	114
5.33 Comparison between calculated and measured cross sections for the 980 nm transition in Nd:fluorozirconate glass	115
6.1 Distortion introduced by the McCumber formula on a single line homogeneously broadened	118
6.2 Comparison between the distortions introduced by the McCumber formula at 150 K and 300 K on a spectral line homogeneously broadened	119

6.3	Distortion introduced by the McCumber formula at 150 K and 300 K on a single line inhomogeneously broadened	121
6.4	Distortion introduced by the McCumber formula at T=150 K on a multipeaked spectral line homogeneously broadened	122
6.5	Distortion introduced by the McCumber formula at T=150 K on a multipeaked spectral line inhomogeneously broadened	124
6.6	Distortion introduced by the McCumber formula at T=150 K on a multipeaked spectral line consisting of inhomogeneously broadened peaks of different amplitudes	126
6.7	Distortion introduced by the McCumber formula at T=150 K on a multi-peaked spectral line consisting of inhomogeneously broadened peaks with different spectral widths	128
6.8	Experimental setup for low temperature measurements	129
6.9	Sample view for the low temperature measurements	131
6.10	Cooling system	132
6.11	Temperature effect on the shape of the spectral line	134
6.12	Temperature effect on the shape of the 870 nm transition in Nd:fluorozirconate	135
6.13	Determination of the calculated emission spectra with the McCumber formula at T~ 132 K in Nd:fluorozirconate	136
6.14	Comparison between the measured and the McCumber calculated cross section spectra at T~ 132 K in Nd:fluorozirconate	138
6.15	Distortion introduced by the McCumber formula on the calculated spectra at T~ 145 K in Nd:fluorozirconate	139
6.16	Distortion introduced by the McCumber formula on the calculated spectra at different temperatures in Nd:fluorozirconate	140

6.17 Effect of uncertainties in baseline subtraction and measured temperature on the calculated spectra in Nd:silicate	141
6.18 Distortion introduced by the McCumber formula on the calculated spectra at $T \sim 156$ K in Nd:silicate	142
6.19 Comparison between the calculated and the measured spectra at $T \sim 143$ K and $T \sim 136$ K in Nd:silicate	143
6.20 Simulation of the emission spectrum of the 870 nm transition in Nd:fluorozirconate at $T=132$ K with a set of 6 Gaussian peaks	149
6.21 Simulation of the absorption spectrum of the 870 nm transition in Nd:fluorozirconate at $T=132$ K with a set of 8 Gaussian peaks	151
6.22 Simulation of the emission spectrum of the 870 nm transition in Nd:fluorozirconate at $T=132$ K with a set of 6 Lorentzian peaks	152
6.23 Simulation of the absorption spectrum of the 870 nm transition in Nd:fluorozirconate at $T=132$ K with a set of 8 Lorentzian peaks	153
6.24 Comparison between the three distortion functions for Gaussian fit, Lorentzian fit and real data at 132 K in Nd:fluorozirconate.	154
6.25 Simulation of the room temperature absorption spectrum of the 870 nm transition in Nd:fluorozirconate with a set of 6 Voigt peaks	155

Chapter 1

Introduction

With the continuing growth and diversification of the telecommunication industry, more new materials are explored, having the purpose of creating more efficient, high quality optical devices, both active and passive. The field of optical amplifiers and fiber lasers has reached peaks that maybe few decades ago were unthinkable. Research in these fields is pushing the limits everyday and bandwidths that few years ago were avoided for the study of amplification are now explored with new viewpoints, since many of the problems have been overcome. An example is the bandwidth at 1400 nm where the OH absorption is very strong but shows very promising perspectives for expanding the telecommunication window in this region, after the treatment for OH absorption. To prepare for the change and expansion in the field, new techniques are developed and old ones are appropriately adjusted, to better describe and characterize particular systems and situations of increasing complexity. More accuracy is required every day as the load of information transported is growing in an exponential manner.

The parameter that has the greatest importance when designing an optical amplifier is the *optical gain*. It describes the fractional amplification of the light as it travels

a certain distance in an active medium. The optical gain can be expressed as

$$\gamma(\lambda) = N_2 \sigma_{em}(\lambda) - N_1 \sigma_{abs}(\lambda) = N_1 \left[\frac{N_2}{N_1} \sigma_{em}(\lambda) - \sigma_{abs}(\lambda) \right] \quad (1.1)$$

where N_1 and N_2 are the populations of the levels between which the transition occurs, and $\sigma_{em}(\lambda)$ and $\sigma_{abs}(\lambda)$ are the stimulated emission and absorption cross sections of the transition. The cross section is a fundamental property of the atom in a particular environment and, in general terms is defined as a fictitious area within which the atom interacts (absorbs or emits) electromagnetic field incident on it.

The first term in the above equation gives the amplification of light due to stimulated emission, and the second one represents losses due to photons absorbed by the active medium to be promoted to the excited state. Stimulated emission and absorption of light are both induced processes, depending on the intensity of the incident radiation (pump light). For large enough pump intensities, population inversion is achieved, N_2 becoming greater than N_1 . The stimulated emission term may exceed the absorption one, and light amplification can occur. Amplification of light is described by a positive net gain. How much the light can be amplified is directly related to the stimulated emission cross section of the particular atom or ion generating the emission. In order to design an optical amplifier, it is not only important to determine absolute values of the gain, but also the spectral distribution, which is critical especially for wave division multiplexing (WDM) transmission systems.

There are many methods to measure the optical gain directly, either in longitudinal geometry [1]-[5], where the fluorescence is recorded in the same direction as the pump light (measurements in optical fibers), or in transverse geometry [6], where fluorescence measurements are done in a direction perpendicular to the direction of radiation (measurements in bulk samples, especially for high concentration of doping ions, where the reabsorption of the emitted light becomes an issue). Measurement are done for small gain as well as saturated gain [7]. More recently, a method of measuring the dynamic

gain tilt (representing the ratio of the change in gain at a given wavelength to the change in gain at a reference wavelength for two different pump levels) has been developed [8] and successfully used for Er doped fibers [9]. The method consists in attenuation and gain measurements, and optimization of the crossover wavelength (for which the gain coefficient has the same value as the absorption coefficient) by iterating the calculated gain until it matches the one measured previously. This technique makes possible determinations of absolute values of the gain coefficient without the limitations in accuracy concerning relative scaling of the gain and the absorption coefficients.

Although measuring the gain directly gives the most reliable results, in most situations this is difficult to achieve. This is the case in bulk samples where absolute values of the input/output optical powers are difficult to estimate with common devices, or optical fibers where the coupling efficiencies and light escaped in the cladding are not evaluated or modeled accurately. Even when both absorption and stimulated emission cross sections can be measured directly, it is in general difficult to determine the population of the levels involved in transition while the sample is being pumped, generating uncertainties in determining the gain coefficient according to Eq.(1.1).

There are also situations when either absorption or emission cross sections are difficult to measured directly. In bulk samples, absolute values of the absorption cross section are straightforward to determine, if the concentration of the doping ions is known. This not the case for optical fibers, where absorption measurements do not give very accurate results and the procedure can become more complicated [10]. Also a problem is to measure absorption cross section between higher energy levels, which cannot be excited with simple lamp sources. On the other hand, fluorescence spectra seem more convenient to measure in optical fibers, although other complications like spectral reabsorption or very weak emission, may considerably limit the accuracy of the measurements. In these situations it would be convenient if one of the cross sections could be predicted if the

other one is known from measurements.

Several theories are available at this moment that allow cross section modeling, and the more complex the system is, the more difficult it is to model. Many popular active media are based on transitions of trivalent rare earth ions in crystalline or glassy hosts and the optical properties of three of them make the subject of the present work, so the discussion will be focused on their optical properties, particularly the behavior in glasses.

Ions with a large number of transitions for which absolute values of the absorption cross sections can be measured, can be further studied with the **Judd-Ofelt analysis** [11], [12]. This theory allows the prediction of the stimulated emission cross section peaks [13], [14] and integrated values for transitions between any levels. It is based on the assumption that the energy difference between the 4f and 5d levels is much larger than the energy spread of the 4f levels due to (L,S) coupling. Also, each J level is considered $2J+1$ fold degenerate. The main idea of the Judd-Ofelt theory is that the strength of any transition can be determined by a set of three parameters Ω_2 , Ω_4 and Ω_6 , that completely define the effect of the host on the radiative properties of the ion. These parameters are calculated by performing a least-square fit of the measured oscillator strengths to the theoretical ones, that contain the dependence on the reduced matrix elements $U_{\{2,4,6\}}$. The more transitions included in the fitting procedure, the more reliable the calculated Judd-Ofelt coefficients are. Once determined, they permit the calculation of the strength of any transition, and consequently the integrated cross section (which is directly proportional, as we will see in the next chapter).

The theory is limited however to providing only transition intensities or integrated cross sections, but not spectral shape. In order to determine spectral distributions, measurements of relative emission spectra are required. In addition, for some ions like Pr^{3+} the above assumption is not valid and large uncertainties have been reported [15],

[16], particularly when so-called "hypersensitive" transitions have been included in the analysis [17], [18]. Apart from these limitations, the theory is particularly valuable for predicting strengths of transitions for which direct measurements are difficult. When properly implemented, the degree of accuracy of the Judd-Ofelt analysis is about 10-15% for most rare earth ions [19], [20]. A detailed treatment of the theory, as well as its successes and failures when applied to rare earth ions, is given by Gorller-Walrand and Binnemans in [21]. New methods to improve the accuracy of the Judd-Ofelt analysis have been developed, either by minimizing the normalized differences in the oscillator strengths [24], or by including the branching ratios [18] in the fitting procedure.

Another accepted approach is based on the relationship between Einstein A and B coefficients, generalized for transitions with finite line width. This is the so called **Einstein or Fuchtbauer-Ladenburg (FL) relation** [25]-[27], which relates the integrated absorption and the stimulated cross sections. In most general form, the FL relation can be written as [31]

$$g_1 \int \nu^2 \sigma_{abs}(\nu) d\nu = g_2 \int \nu^2 \sigma_{em}(\nu) d\nu \quad (1.2)$$

where $g_1 = 2J_1 + 1$ and $g_2 = 2J_2 + 1$ are the degeneracies of the levels 1 and 2. The approach is based on two main assumptions, of which at least one must be satisfied in order to be successful. Either the individual Stark levels of the manifolds involved in transitions are equally populated, or the transitions between them have the same strength of oscillation. The same approximation is used in the Judd-Ofelt theory. Since neither of these are true for the rare earth doped glasses, the applicability of this method is very limited in modeling amplifying systems, deviations of 20% or more being reported [20], [28]-[32].

In the literature however, there are various forms of the FL relation, only one of them (eq.(1.2)) expressing the relationship between the absorption and emission cross sections. As we saw, this is **not an exact relation**, resulting in poor predictions,

particularly for wide transitions of the rare earth ions where the distribution of the atoms is not uniform among the individual levels and for which the strength is different for different individual levels (e.g. 1500 nm transition of Er^{3+} in silicate glass, or 865 nm of Nd^{3+} in fluorozirconate glass).

The form that is maybe most widely used, relates the emission cross section to the radiative lifetime of the manifold. For transitions between two sharp individual levels 1 and 2, it can be written as [33]-[35]

$$\sigma_{em}(\nu) = \frac{A_{21}c^2}{8\pi n^2\nu_0^2} g_{em}(\nu) \quad (1.3)$$

where $A_{21} = 1/(radiative\ lifetime)$ is the Einstein A coefficient, $g_{em}(\nu)$ is the *emission lineshape function* of the transition (normalized to unity over the entire frequency range), ν_0 is the peak frequency and n is the refractive index. This is an **exact relation** and is a reliable way of determining the emission cross section from fluorescence measurements for rare earth doped crystals. In integral form, the above relation can describe accurately the emission cross section for transitions in glasses, between manifolds that are wide splitted by the crystal field of the host [13], [14], [31], [36]-[40]. When the fluorescence is difficult to measure, the radiative lifetime is determined by the Judd-Ofelt technique [13], [14]. Equation (1.3) can lead to similar expressions allowing the stimulated emission cross section be calculated exactly in terms of the intensity of the fluorescence and the lifetime of the manifold [33], [36], [41]-[45]. In these methods, the radiative lifetime of the manifold is assumed to be the same as the measured fluorescence lifetime, neglecting any other processes that may reduce the quantum efficiency of the transition (like nonradiative decay).

A third distinctive form of the FL relation connects the absorption cross section to the radiative lifetime as follows:

$$\sigma_{abs}(\nu) = \frac{g_2}{g_1} \frac{A_{21}c^2}{8\pi n^2\nu_0^2} g_{abs}(\nu) \quad (1.4)$$

which is again valid for sharp transitions described by the *absorption lineshape* $g_{abs}(\nu)$. The presence of the two degeneracy terms g_1 and g_2 reveals immediately the fact that this is an **approximate relation**. In principle, the absorption cross section can be determined measuring the spontaneous lifetime and the relative absorption spectra, using the above equation [42]. This may be an extreme situation when the exact concentration of the sample is not known, and absolute values of the absorption cross section can not be determined. However, the above equation was mainly used to determine the radiative lifetimes from already measured absorption cross sections [13], [15], [19], and the failures of the method in providing reliable values have been expressed by the same authors.

For the most general situations, there is no simple way of relating the absorption and emission cross sections, unless the detailed Stark structure is known. Since the absorption and emission spectra of rare earths differ from host to host, low temperature measurements are required for each ion-host combination, in order to resolve the individual peaks. This is however not very useful for glassy hosts, since the large inhomogeneous broadening of the spectral lines due to nonuniformities in the local environment of the ion limits the spectral resolution.

However, if the width of the individual Stark level is small compared to $k_B T$ (k_B is Boltzmann's constant and T is the temperature), and for ions in thermal equilibrium with the lattice, the two cross sections are connected by the **McCumber or reciprocity relation** [46]:

$$\sigma_{em}(\nu) = \sigma_{abs}(\nu) \exp\left(\frac{\epsilon - h\nu}{k_B T}\right) \quad (1.5)$$

where ϵ is the excitation energy between the two levels, k_B is Boltzmann's constant and T is the absolute temperature. The theory of McCumber is a very powerful tool that permits, according to these two very general assumption, accurate calculations of one of the cross sections, when the other one is known from measurements. In contrast with the FL relation (1.2), which relates integrated cross sections, the McCumber relation

connects the absorption cross section to the emission one at a particular wavelength. According to this, the absorption and emission cross section are uniquely related at any wavelength across the spectrum. This way, it provides absolute values, as well as spectral information.

When the above conditions are not met, distortions from the actual value and spectral shape are expected. For the case of rare earth doped systems, the assumption that ions are in thermal equilibrium with the host holds very well, since the induced phonon relaxations within a certain Stark manifold occur in a much shorter time (less than picoseconds) than the lifetime of the manifold (milliseconds). The other assumption however, regarding the narrow width of the individual Stark levels compared to $k_B T$, has been doubted in some situations. Numerical studies [47], [48] have shown that the homogeneous broadening has a greater effect on the predicted lineshape than the inhomogeneous broadening. The homogeneous broadening is described by a Lorentzian function, which has longer wings compared to the Gaussian function that describes the inhomogeneous broadening. When the wings of these functions are multiplied by a growing or decaying exponential according to Eq.(1.5), specific distortions from the real shape may be generated for each type of broadening.

The amount of distortion is expected to be small at room temperature for typical values of the homogeneous and inhomogeneous widths of rare earth ion transitions in glasses, although it can become significant at low or high temperatures [47]. The homogeneous broadening increases with the temperature as T^2 , so at sufficiently high temperatures, the first assumption of the McCumber theory will not be satisfied, and the theory will eventually break down. The inhomogeneous broadening, which is temperature independent, dominates at low temperature, and as the temperature decreases, the value of $k_B T$ becomes smaller while the spectral width stays constant. Here again we expect that the McCumber theory will not give correct predictions of the cross sections.

Experimental tests performed on the McCumber theory show very contradictory results. When the calculated cross sections have been compared with the measured ones, excellent or reasonably good agreement has been found at room temperature, for both crystalline hosts [32], [34], [49], [50] and glassy hosts [3], [31], [39], [40], [43], [44], [51], [52] and also at low temperature [37]. However, a number of experimental studies have reported discrepancies of various degrees for glasses [45], [48], [53] and crystals [35], [54], particularly in the wings of the lineshape.

The present work is a detailed study of the range of validity of the McCumber theory, focussing particularly on those aspects that most critically affect its applicability to transitions of rare earth ions in glasses. To analyze the effect of the spectral broadening on the accuracy of the technique, experiments were performed at room and low temperature. The theory was tested by comparing the cross sections calculated using the McCumber relation (1.5) with those obtained from measurements. At room temperature, a number of ground state transitions of three different rare earth ions (Nd, Er and Tm) in oxide and fluoride glass hosts have been studied. The results at room temperature show excellent agreement between the calculated and the measured cross section spectra. This is also in good agreement with the theoretical predictions previously reported [47]. This good agreement does not hold for the low temperature results, however. The distortion observed in this case agrees with that expected theoretically, and corresponds to the amplification of the gaussian wings. We will show that the McCumber theory must be used with caution at low than room temperature.

This thesis is structured into seven chapters. Chapter one presented the landscape and gives the motivation of this study. In chapters two and three, the theoretical background is gradually emphasized, from the basic concepts needed in understanding the physical phenomena studied experimentally, to the development of the three theories that allow cross section predictions. More detailed derivations are presented to make

it easy to follow the particular approximations made within each theory. This is for understanding the limits and performances of each theory when used to predict cross section values of rare earth ions in glassy hosts. Chapters 4, 5 and 6 are dedicated to experimental method, results and discussions at room and low temperature, while chapter 7 concludes the entire work and presents some suggestions on improving the experimental method and also future directions

Chapter 2

Theoretical background

This chapter contains the basic information, principles and concepts necessary in the proper understanding of the physical phenomena developed in the later parts of this work. As a starting point, a brief review of the Einstein treatment is presented, describing the interaction between a physical system in equilibrium with blackbody radiation at the absolute temperature T . Since the experiments are performed under two types of excitation, simple calculations are carried for both, broadband and narrowband excitations. Although this makes the topic of any modern physics course, it is worth reviewing it here to show the progressive development of the relationship between absorption and emission as applied to more and more complex systems. As the focus of my work is on the applicability of the McCumber theory to optical transitions of rare earth doped glasses, a short description of the optical properties of the rare earth ions in fluoride and silicate glass is also given.

2.1 Interaction between light and atomic systems

Consider an atomic system with a number of discrete energy levels. Let 1 and 2 be any two of them, with the corresponding energies E_1 and E_2 such that $E_1 < E_2$. The number of atoms per unit volume in each of the two states are N_1 and N_2 respectively. In thermal equilibrium, the distribution of the population among the levels is described by Boltzmann statistics. The number of atoms per unit volume in the excited state 2 is given by the Boltzmann factor

$$N_2 = N_1 e^{-(E_2 - E_1)/k_B T} \quad (2.1)$$

where k_B is Boltzmann's constant and T is the absolute temperature.

When the system interacts with light, atoms in the lower state 1 can be promoted to the higher state 2 by *absorbing* a photon of energy equal to the energy difference between the two levels. Atoms found in the higher level 2 can relax spontaneously to level 1 either emitting a photon of the same energy, or in a nonradiative manner, by losing their energy in interactions with other atoms or the surrounding medium. *Spontaneous emission* is a process governed by the *Einstein A coefficient*, A_{21} . This represents the probability per unit time that the atom decays spontaneously from level 2 to level 1.

Another process involved in the interaction between light and the atomic system is *stimulated* or *induced emission*, where a photon forces an atom in the excited state to decay by emitting another photon, in the same direction and with the same phase as the incident photon. This process contributes to the amplification of the light in an active medium. Stimulated emission and absorption are both induced processes¹ and their transition probabilities W_{21}^{ind} and W_{12}^{ind} are proportional to the spectral energy density of the incident radiation.

$$W_{12}^{ind} = B_{12} \times \text{Spectral Energy Density} \quad (2.2)$$

¹These processes are studied in more detail in Appendix A

$$W_{21}^{ind} = B_{21} \times \text{Spectral Energy Density} \quad (2.3)$$

The proportionality constants are B_{21} and B_{12} , the *Einstein B coefficients*. To make the discussion quantitative, it is necessary to introduce two concepts, one to describe the spectrum of the radiation, another to characterize the atomic transition. The spectral

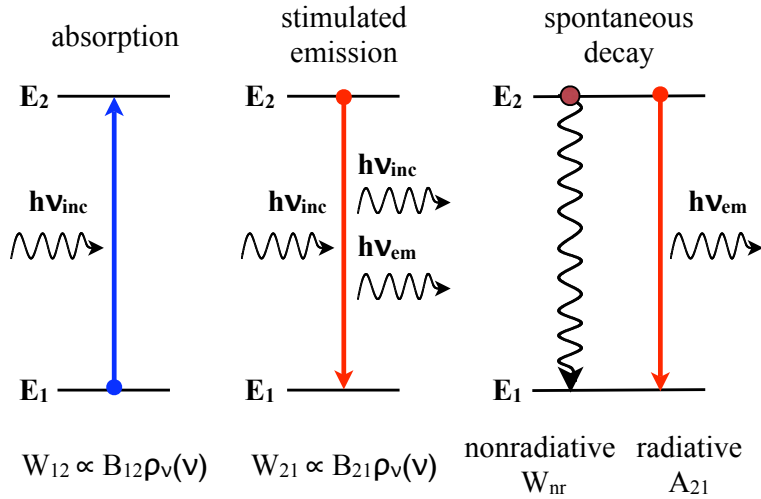


Figure 2.1: Representation of absorption, stimulated emission and spontaneous decay

distribution function $\rho_\nu(\nu)$ is defined as the radiation energy density per unit frequency interval. It describes the number of photons with the frequencies between ν and $\nu + \Delta\nu$. The total energy density ρ of the radiation is obtained by integrating the spectral distribution over the entire frequency range. The atomic transition is described by the lineshape function $g(\nu)$. This gives the relative probability per unit time that the atom absorbs or emits a photon of frequency ν . The lineshape function is normalized over all the frequencies, such that $\int g(\nu)d\nu = 1$. In general, the induced probability that an atom executes a transition between two states 1 and 2 is calculated by integrating the contribution of both factors [55] over the entire frequency range. The above equations

can be written for the general case as

$$W_{12}^{ind} = \int B_{12}\rho_\nu(\nu)g(\nu)d\nu \quad (2.4)$$

$$W_{21}^{ind} = \int B_{21}\rho_\nu(\nu)g(\nu)d\nu \quad (2.5)$$

In order to discuss these processes, two approaches are used, Einstein's treatment for broadband excitation and semiclassical approach for excitation with a narrowband source. Although the relationship between the Einstein coefficients stays the same in both situations, the latter situation is very important in describing laser pumped systems, where the incident radiation is almost monochromatic.

2.1.1 Broadband excitation: Einstein A and B coefficients

Einstein's treatment assumes that the system interacts with blackbody radiation at absolute temperature T in thermal equilibrium. The system consists of isolated atoms, where the nonradiative processes are neglected, having simple, nondegenerate energy levels. The spectral density for the blackbody spectrum is given by the Plank's formula

$$\rho_\nu(\nu) = \frac{8\pi h\nu^3}{c_n^3} \frac{1}{e^{h\nu/k_B T} - 1} \quad (2.6)$$

where h is the Plank's constant, c_n is the speed of light in the medium and T is the absolute temperature. As shown in Fig.(2.2), the blackbody radiation spectrum is very broad compared to the lineshape of the atom. Across the frequency range of the atomic transition, the spectral density does not vary much, and can be considered as having constant value, $\rho_\nu(\nu_0)$, where $\nu_0 = (E_2 - E_1)/h$ is the center frequency of the lineshape function. The induced transition probabilities in this case become

$$W_{12}^{ind} = B_{12}\rho_\nu(\nu_0) \int g(\nu)d\nu = B_{12}\rho_\nu(\nu_0) \quad (2.7)$$

$$W_{21}^{ind} = B_{21}\rho_\nu(\nu_0) \int g(\nu)d\nu = B_{21}\rho_\nu(\nu_0) \quad (2.8)$$

Historically, Einstein defines the B coefficients in an ad-hock way in 1917, as proportionality constants between the induced transition probabilities and spectral density of the blackbody radiation. This is when he introduced the concept of stimulated emis-

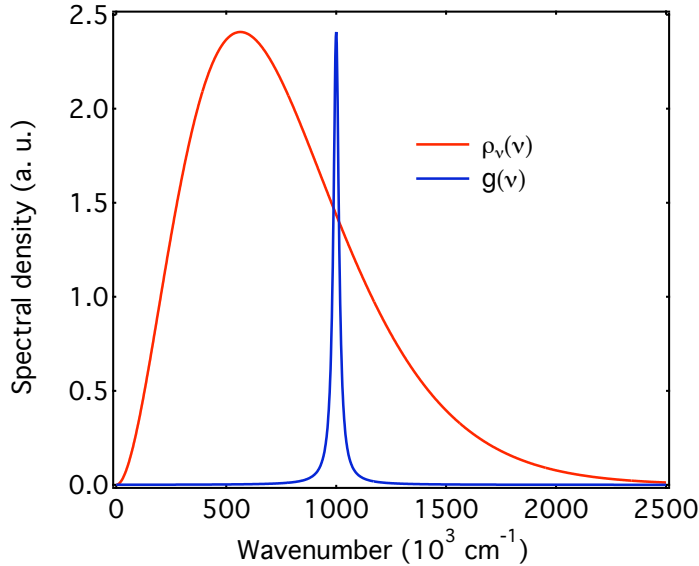


Figure 2.2: Spectral density of the blackbody spectrum at $T \sim 300$ K compared to the Lorentzian lineshape function of an atomic transition with full width of half maximum equal to 30 cm^{-1} . Both functions are normalized to the same peak value.

sion as the third important radiative process in the interaction between the system and blackbody radiation in thermal equilibrium.

The rate of change in the population of a level is given by the number of atoms per unit volume per unit time entering the level minus the atoms leaving that level. Taking all three radiative processes into account (absorption, stimulated emission and spontaneous emission), the rate equation for the level 2 can be written as

$$\frac{dN_2}{dt} = N_1 B_{12} \rho_\nu(\nu_0) - N_2 B_{21} \rho_\nu(\nu_0) - N_2 A_{21} \quad (2.9)$$

In thermal equilibrium, $dN_2/dt = 0$. The above equation becomes

$$\frac{N_2}{N_1} = \frac{B_{12} \rho_\nu(\nu_0)}{B_{21} \rho_\nu(\nu_0) + A_{21}} \quad (2.10)$$

Replacing N_2/N_1 from Eq.(2.1), we can write

$$e^{-h\nu_0/k_B T} = \frac{B_{12}\rho_\nu(\nu_0)}{B_{21}\rho_\nu(\nu_0) + A_{21}} \quad (2.11)$$

Solving for $\rho_\nu(\nu_0)$, we obtain

$$\rho_\nu(\nu_0) = \frac{A_{21}}{B_{21}} \frac{1}{\left(\frac{B_{12}}{B_{21}}\right) e^{h\nu_0/(k_B T)} - 1} \quad (2.12)$$

This is the expression of the spectral density of the blackbody radiation as a function of the Einstein A and B coefficients, which are properties of the atom that interacts with the light, in thermal equilibrium. If we compare this with the Plank formula from Eq.(2.6), they should be equivalent at any temperature. This is indeed the case if

$$B_{21} = B_{12} \quad (\text{Einstein B coefficients}) \quad (2.13)$$

$$A_{21} = \frac{8\pi h\nu^3}{c_n^3} B_{21} \quad (\text{Einstein Relation}) \quad (2.14)$$

These equations are very important in describing the relationship between the three radiative processes discussed in an optical medium. Eq.(2.13) states the equivalence between the absorption and stimulated emission. That is, a transition that has a high absorption probability will have an equally high stimulated emission probability. The second equation, Eq.(2.14), relates the stimulated and spontaneous emission rates. The stimulated emission rate is proportional to the spontaneous emission rate, so higher amplification can be obtained for transitions with stronger spontaneous emission. Also, for practical purposes, measurements of spontaneous emission (or absorption) can provide information about the amplification of the light for a particular transition.

These two equations, relating stimulated emission to spontaneous emission and absorption of light for a simple atomic system with nondegenerate energy levels, make the starting point of my work. More complex systems will be discussed later in this chapter, like systems with degenerate energy levels and atoms in dense optical media

where the the degeneracy is removed by the crystal field of the surrounding medium and the atomic transitions are affected by spectral broadening.

2.1.2 Narrowband excitation. Transition rates

For optical media pumped with laser light, the spectral density $\rho_\nu(\nu)$ is very narrow compared to the lineshape of the atomic transition. In this situation the lineshape is assumed constant across the frequency range of the pump light, its value $g(\nu_p)$ being taken at the pump frequency ν_p . The induced transition rates from Eq.(2.4) and Eq.(2.5) in this case become

$$W_{12}^{ind} = B_{12} g(\nu_p) \int \rho_\nu(\nu) d\nu = B_{12} g(\nu_p) \rho \quad (2.15)$$

$$W_{21}^{ind} = B_{21} g(\nu_p) \int \rho_\nu(\nu) d\nu = B_{21} g(\nu_p) \rho \quad (2.16)$$

Here the induced transition rates are proportional to the total energy density of the laser radiation. As shown in Appendix A, the processes of stimulated emission and absorption are perfectly equivalent. Under the effect of monochromatic radiation, the system can make a transition between any two quantum states k and l if the frequency of the field ω_p matches perfectly the atomic frequency $\omega_{kl} = (E_k - E_l)/\hbar$, where E_k and E_l are the energies of the two states. If initially the system is in state k , for those frequencies of the field $\omega_p \simeq +\omega_{kl}$, the system will decay to a lower energy state $E_l = E_k - \hbar\omega_p$ by emitting the energy $\hbar\omega_p$, though by stimulated emission. For $\omega_p \simeq -\omega_{kl}$, the system is promoted to a higher energy state $E_l = E_k + \hbar\omega_p$ by absorbing the energy $\hbar\omega$. So the processes of absorption and stimulated emission are both induced processes, one being the reverse of the other. The induced transition rates being then equal, from Eq.(2.15) and Eq.(2.16) we conclude, as for the previous situation, that the coefficients B_{12} and B_{21} are equal.

Written as a function of the matrix elements μ_{21} of the electric dipole moment of the atom, coupling the states 2 and 1, the induced emission transition rate was derived

in Appendix A, Eq.(A.26) as

$$W_{21}^{el} = \frac{\pi}{6\hbar^2} |\mathbf{E}_0|^2 |\mu_{21}^e|^2 \delta(\Delta\omega) \quad (2.17)$$

where $|\mathbf{E}_0|$ is the real part of the amplitude of the electric field and $\Delta\omega = \omega_p - \omega_{kl}$ is the frequency mismatch between the frequency of the field and the atomic frequency. The delta-function dependence shows that there is no interaction between the field and the system unless the two frequencies coincide. This is not the representation of a real situation, and we can adjust the above formula by replacing the delta-function with the lineshape function $g(\nu_p)$ to describe the probability that the atom emits or absorbs within the range $d\nu$ about the frequency ν_p . The induced transition rate becomes

$$W_{21}^{el} = \frac{\pi}{6\hbar^2} |\mathbf{E}_0|^2 |\mu_{21}^e|^2 \frac{1}{2\pi} g(\nu_p) \quad (2.18)$$

where $\nu_p = \omega_p/2\pi$ represents the center frequency of the electromagnetic radiation.

For plane, monochromatic radiation, the total energy density can be written in terms of the amplitude of the electric field $|\mathbf{E}_0|$ as

$$\rho = \frac{1}{2} n^2 \epsilon_0 |\mathbf{E}_0|^2 \quad (2.19)$$

where ϵ_0 is the permittivity of free space and n is the refractive index of the medium. Using this into E.(2.18), we can write the induced transition rate as

$$W_{21}^{el} = \frac{2\pi^2}{3\epsilon_0 h^2 n^2} |\mu_{21}^e|^2 \rho g(\nu_p) \quad (2.20)$$

Comparing equations (2.16) and (2.20), the Einstein B_{21} coefficient can be written as

$$B_{21} = \frac{2\pi^2}{3\epsilon_0 h^2 n^2} |\mu_{21}^e|^2 \quad (2.21)$$

The spontaneous transition rate A_{21} as derived by Svelto [69] is

$$A_{21} = \frac{16\pi^3 \nu^3 n}{3\epsilon_0 h c^3} |\mu_{21}^e|^2 \quad (2.22)$$

From Eq(2.21) and Eq.(2.22) we see that the relationship between the Einstein A and B coefficients stays the same when the system is excited with nearly monochromatic radiation as for broadband excitation Eq.(2.14), where $c_n = c/n$ has been used for the speed of light in the medium of refractive index n.

If the levels 1 and 2 are $g_1 = 2J_1 + 1$ and $g_2 = 2J_2 + 1$ fold degenerate respectively, the relationship between the Einstein B coefficients becomes

$$g_2 B_{21} = g_1 B_{12} \quad (2.23)$$

where J_1 and J_2 are the total angular momenta of the two levels. The Einstein relation (2.14) is unchanged by the degeneracy of the two levels since stimulated and spontaneous emission originate from the same manifold and, as long as all individual levels emit on the same frequency, this is an exact relation. However, for atoms in environments like crystals and glasses, the crystal field removes partially or completely the degeneracy of the manifold, and Einstein's relation (although valid for two individual levels) is not suitable to describe the relationship between spontaneous and stimulated emission. Also, Eq.(2.23) is not a good way of describing the relationship between the stimulated emission and absorption for those systems. These are very important relations that characterize well the interaction of the electromagnetic radiation with ideal two-level systems, or individual levels. For more complex situations like rare earth ions in crystalline or glassy hosts, these relationships need to be modified and generalized adequately.

2.2 Gain in active media

As monochromatic light traverses an amplifying medium of a finite length, a fraction of it may get either absorbed by the atoms of the medium, or may induce light emission by forcing atoms in the excited state to decay to a lower energy state. Also some atoms may

decay by spontaneous emission, but since photons are emitted with equal probability in all directions, this process does not contribute to the amplification of the beam, the fraction emitted in the direction of the beam being negligible. If the intensity of the beam

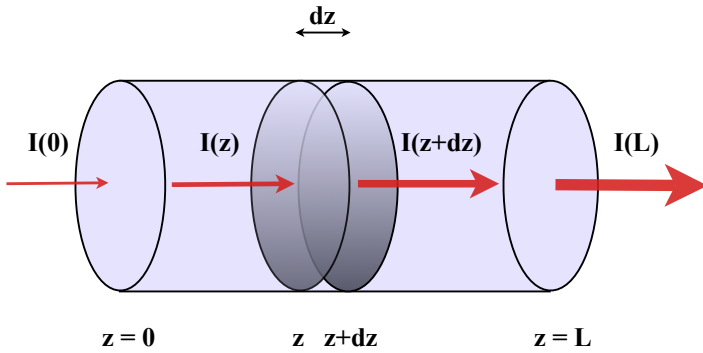


Figure 2.3: Amplification of light as it propagates in a gain medium of length L

at a certain location z in the medium is $I(z)$, the change in intensity per unit length for small signal amplifications, satisfies a *Beer's Law-like* relation $dI(z)/dz = \gamma(\nu)I(z)$ with the gain coefficient $\gamma(\nu)$ defined to contain both emission amplification and absorption losses. The photons added to the signal per unit time per unit volume can be written as

$$\frac{dN}{Vdt} \equiv \frac{dN_2}{dt} = N_2 W_{21}^{ind} - N_1 W_{12}^{ind} \quad (2.24)$$

where N_1 and N_2 are respectively the populations of the lower and upper manifolds involved in transition, and W_{12}^{ind} and W_{21}^{ind} are the corresponding induced transition probabilities. These are proportional to the intensity of the beam and the atomic line-shape function $g(\nu)$, the proportionality constants being the Einstein coefficients B_{12} and B_{21} . Equation (2.24) can then be written as

$$\frac{dN}{dt} = [B_{21}g_{em}(\nu)N_2 - B_{12}g_{abs}(\nu)N_1] \frac{I}{c/n} \quad (2.25)$$

Here c is the speed of light, n is the refractive index of the amplifying material, and the energy density ρ was expressed in terms of the light intensity as $I/(c/n)$. The change (increase for light amplification) in the energy density per unit time is

$$\frac{d\rho}{dt} \equiv \frac{dN}{dt}h\nu = \frac{d}{dt}\left(\frac{I}{c/n}\right) \quad (2.26)$$

With this, we can write the change in the beam intensity per unit length as

$$\frac{dI}{dz} = (B_{21}g_{em}(\nu)N_2 - B_{12}g_{abs}(\nu)N_1)h\nu\frac{I}{c/n} = \gamma(\nu)I(z) \quad (2.27)$$

where the optical gain $\gamma(\nu)$ can be expressed in terms of the populations of the two manifolds as

$$\gamma(\nu) = (B_{21}g_{em}(\nu)N_2 - B_{12}g_{abs}(\nu)N_1)\frac{h\nu}{c/n} \quad (2.28)$$

Writing the stimulated emission and absorption cross sections of the transition as

$$\sigma_{21}(\nu) = B_{21}g_{em}(\nu)\frac{h\nu}{c/n} \quad (2.29)$$

$$\sigma_{12}(\nu) = B_{12}g_{abs}(\nu)\frac{h\nu}{c/n} \quad (2.30)$$

the gain coefficient can be expressed in terms of the two cross sections as

$$\gamma(\nu) = \sigma_{21}(\nu)N_2 - \sigma_{12}(\nu)N_1 \quad (2.31)$$

Amplification of light occurs when the term containing stimulated emission overcomes the one containing absorption, resulting in a positive net gain. The gain is determined by the two cross sections and the populations of the two levels. To design optical amplifiers and lasers, good knowledge of these parameters is required. Absolute values of the cross sections as well as spectral distributions are extremely important.

The cross section is a fundamental property of the atom in a particular environment and represents a fictitious area within which the atom interacts (absorbs or emits) with an electromagnetic field incident on it. In general terms, the cross section can be written

as the area of the beam divided by the number of atoms interacting with the field per unit time, times the probability of induced transition (absorption or stimulated emission). This is

$$\sigma_{em/abs}(\nu) = \frac{Area}{\text{N/time}} W_{21/12}^{ind} = \frac{Area}{Energy/(h\nu \text{ time})} W_{21/12}^{ind} = \frac{h\nu}{I} W_{21/12}^{ind} \quad (2.32)$$

where I is the intensity of the incident beam. Replacing $W_{21/12}^{ind}$ from Eq.(2.15) and Eq.(2.16), and using the relationship between the energy density and the intensity of light $\rho = I/(c/n)$, we obtain the same expressions for the cross sections as those used in the expression of the gain Eq. (2.29) and Eq.(2.30).

For a system with two nondegenerate levels, the absorption and emission cross sections are equal, since the Einstein B coefficients B_{12} and B_{21} are equal. We can then write

$$\sigma_{ij}(\nu) = \sigma_{ji}(\nu) \quad (2.33)$$

for any two individual levels i and j within a manifold. This is based on the equivalency between the absorption and stimulated emission discussed in Appendix A and the principle of detailed balance which assumes that the total number of atoms distributed among the two levels is conserved (and equal to the concentration of the doping ions).

2.3 Optical properties of rare earth ions in fluoride and silicate glasses

Among the more popular active media are the rare-earth doped glasses and crystals. Because of their very special optical properties, many rare earths have been used in designing lasers and amplifiers [20], [56] in almost all spectral regions from ~ 450 nm to ~ 2900 nm. In crystalline hosts, high cross sections (and therefore high gain) can be achieved, making these systems great candidates for lasers, while in glassy environments,

the ability of obtaining amplification across a wider range of frequencies for a large variety of chemical compositions and with high optical quality transmission make them more suitable for optical amplifiers in the telecommunication industry.

2.3.1 General Characteristics

The rare earths of interest are the lanthanides, which are chemical elements characterized by the filling of the $4f$ shell. They are placed in the 6th period of the periodic table with the atomic number Z varying from 58 (cerium) to 71 (lutetium). They have the following electronic configuration: $1s^2 2s^2 2p^6 3s^2 3p^6 4s^2 3d^{10} 4p^6 5s^2 4d^{10} 5p^6 6s^2 4f^x (5d^1)^2$, where x varies from 1 to 14 in the series. The $4f$ electrons have almost no contribution to the chemical valence, therefore the atom can easily lose the $6s$ and $5d$ electrons and also one electron from the $4f$ shell, so they are most stable as trivalent ions. Their configuration is

$$1s^2 2s^2 2p^6 3s^2 3p^6 4s^2 3d^{10} 4p^6 \mathbf{5s^2 4d^{10} 5p^6 4f^y} \quad (2.34)$$

where y represents the number of electrons in the $4f$ shell. The trivalent rare earth ions are the basic elements in optical devices, and their optical properties will be investigated further in this section.

The optical properties of the rare earth ions are determined by the $4f$ electrons, which are well shielded from the environment by the outer $5s$ and $5p$ electrons. As a consequence, the interaction between these electrons and the surrounding medium is very weak, both with the crystal field of the host, and with the lattice phonons. This results in a narrow spread of the Stark structure (compared to transition metals, for example, which involve $3d$ electrons that are only shielded by two outer $4s$ electrons), spectra that do not present large variations from host to host, and low nonradiative decay rates of the excited states. The Hamiltonian for the ion-host combination can be

²Only cerium, gadolinium and lutetium have an electron in the $5d$ shell

written as

$$H = H_0 + H_{el} + H_{SO} + H_{cf} \quad (2.35)$$

where H_0 represents the central field Hamiltonian due to the interaction between the electrons and nucleus, H_{el} represents the electrostatic interaction between electrons, and H_{SO} is the spin-orbit interaction term. These three terms represent the Hamiltonian of the free ion. The other term H_{cf} describes the interaction between the ion and the crystal field of the environment. The total Hamiltonian should also include the interaction with the lattice phonons $V_{phonons}$ and with the electromagnetic field V_{elmg} . Since these two terms are time dependent, they do not affect the eigenenergies of the system, but rather generate transitions between different levels by absorption and emission of photons and lattice phonons (see discussion in Appendix A).

As already mentioned, the interaction of the $4f$ electrons with the surrounding medium is very weak and the last term in Eq.(2.35) is treated as perturbation. The solution to the free ion Hamiltonian is described by a set of $2J + 1$ -fold degenerate states labeled using the spectroscopic notation $^{2S+1}L_J$, where S is the total spin, L is total orbital angular momentum and $\mathbf{J} = \mathbf{S} + \mathbf{L}$ is total angular momentum due to all $4f$ electrons of the ion. The states with different L and S quantum numbers are mixed by the spin-orbit interaction (Russell-Saunders coupling), which lifts the degeneracy in the total angular momentum into J levels, separated by few thousand cm^{-1} . The mixed states represent eigenstates of J but not of L or S , so L and S are not good quantum numbers for describing the state of the free ion. The crystal field splits each J level into $2J + 1$ Stark components, generally separated by few hundred cm^{-1} . In glassy environments, the degeneracy is completely lifted, except for the Kramers degeneracy which is still present for ions with odd number of electrons. The effect of the above terms of the Hamiltonian on the energy splitting is shown in Fig.(2.4). Observed spectra in visible, infrared and even in ultraviolet are determined, for most rare earth

ions, by transitions between different Stark components $\{L, S, J, M_J\}$ of the same $(4f)^n$ electronic state $\{L, S, J\}$, where M_J runs in integer steps from $-J$ to J . However, for

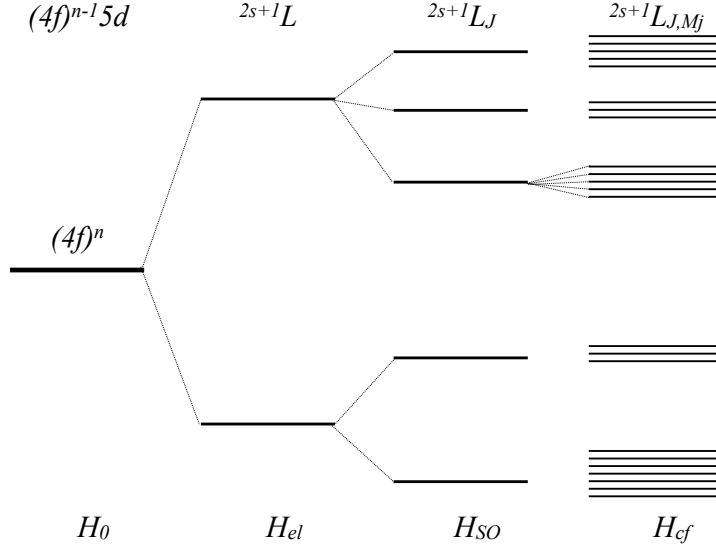


Figure 2.4: Effect of different terms of the Hamiltonian on the Energy Splitting

some ions like Pr^{3+} higher lying states $(4f)^{n-1}5d$ are low enough to produce strong absorption and emission spectra in ultraviolet [20].

The crystal field generates the admixing of the states of opposite parity and determines the strength of the radiative transitions. The strength and the symmetry of the crystal field causes host to host variations in the overall shape of the absorption and emission spectra between different manifolds, regarding not only the intensities of the transitions between individual Stark levels but also the position of the energy levels of different Stark components. Also, the energies of the Stark manifolds are affected by the covalent bonding between the host and the rare earth ion, which reduces the effective nuclear charge of the ion. All energy levels will be shifted toward lower values, and the more covalent the host, the larger the shift. This effect is known as *nephelauxetic effect*. As a result, the ions will absorb and emit at lower energies (longer wavelengths) in silicate glasses than in fluoride glasses, which present a more ionic bonding mech-

anism. This effect is combined with the *lanthanide contraction*³ property of the rare earth elements, resulting in a smaller shift as the atomic number increases in the series.

2.3.2 Intensities of optical transitions

The strength of a transition $S_{i \rightarrow j}$ between two states $\{L, S, J, M_J\}_{i \rightarrow j}$ is given by the square matrix elements of the oscillating dipole moment of the atom $|\mu_{ij}|^2$

$$S_{i \rightarrow j} = |\langle i | \hat{\mu} | j \rangle|^2 = |\langle i | \hat{\mu}_e | j \rangle|^2 + |\langle i | \hat{\mu}_m | j \rangle|^2 \quad (2.36)$$

where $\mu_e = \sum_y e \mathbf{r}_y$ and $\mu_m = e/2m(\mathbf{L} + \mathbf{2S})$ are the electric and the magnetic dipole moments due to all $4f$ electrons respectively.

The selection rules for the electric dipole moment forbid transitions between states of the same parity, like the ones between the different $\{L, S, J, M_J\}$ states, which correspond to the same $(4f)^n$ electronic configuration. In practice, these transitions are observed, however, due to the mixing of the empty higher lying states of opposite parity $(4f)^{n-1}5d$ into the $(4f)^n$ states by the crystal field, when this lacks inversion symmetry. This is usually true for glass media, and most of the observed absorption and emission spectra are determined by electric dipole transitions between the $4f$ and the $5d$ components of the different states. Magnetic dipole transitions are allowed, but they are about 5 orders of magnitude weaker than allowed electric dipole transitions.

The strength of the transition is therefore determined by the strength of the crystal field that generates the admixing of the states of opposite parity and also the by symmetry of the field in a particular host. The optical intensities of most $4f$ transitions vary within a factor of 2 or 3 between different hosts, except for the *hypersensitive transitions*, which are very sensitive to the environment, sometimes presenting variations of several orders of magnitude between different hosts [21].

³the decrease in the radius of the rare earth element as the atomic number increases in the series due to the imperfect screening by the $4f$ electrons

The intensities of the radiative transitions are usually expressed in terms of a dimensionless parameter f known as *oscillator strength*. A general definition⁴ of the oscillator strength of a transition between two individual Stark levels i and j is

$$f_{ij} = \frac{1}{3} \frac{2m\omega_{ij}}{\hbar^2} \frac{|\mu_{ij}|^2}{e^2} = f_{ij}^e + f_{ij}^m \quad (2.37)$$

where ω_{ij} is the angular frequency of the transition, m and e are the mass and the charge of the electron and f_{ij}^e and f_{ij}^m are the electric and magnetic dipole oscillator strengths of the $i \rightarrow j$ transition. The factor 1/3 is needed in describing randomly oriented systems, where the electric dipole oscillates in all three directions with equal probability. The oscillator strength obeys the sum rule, such that $\sum_i f_{ij} = 1$, where the summation is over all individual Stark components of the manifold from which the transitions originate. Allowed transitions have oscillator strengths close to 1, while forbidden transitions are characterized by very small oscillator strengths. For rare earth ions $f \sim 10^{-6}$ although variation of few orders of magnitude between different transitions are commonly observed.

We can refer to Eq.(2.20) to relate the absorption and stimulated emission processes to the oscillator strength. For transitions between two individual levels of a manifold, the oscillator strengths for absorption and stimulated emission are equal and we can write

$$f_{ij} = f_{ji} \quad (2.38)$$

For manifolds with a more complex level structure as is the case of rare earth ions in glass, the oscillator strength for absorption and for stimulated emission are different, depending on the absorption and emission rates, the frequency of each individual transition and population of the different levels within the manifold.

⁴This definition can be understood as the relative strength of the transition between two states i and j , relative to the strength of a harmonic oscillator of the same frequency, between the first lower states 0 and 1 [57].

The oscillator strength for stimulated emission f_{em} can be related to the spontaneous transition rate A_{21} from manifold 1 to manifold 2 using relation (2.22) and correcting for the presence of the medium of refractive index n by dividing Eq.(2.37) by n (assuming linear media where the speed of light $c_n = c/n$). For media with high local field symmetry, Dexter's correction for the local field has to be considered [58]. With this we write the radiative transition rate as

$$A_{21} = \frac{8\pi^2 e^2 n^2 \nu^2}{(4\pi\epsilon_0)mc^3} f_{em} \quad (2.39)$$

where ϵ_0 is the permitivity of the free space and ν is the frequency of the transition. Using Eqs. (2.21), (2.29) and Eq.(2.37) corrected for the local field, we can express the oscillator strength for emission as a function of the integrated emission cross section $\sigma_{21}(\nu)$ as

$$f_{em} = (4\pi\epsilon_0) \frac{mc}{\pi e^2} \int \sigma_{21}(\nu) d\nu \quad (2.40)$$

which basically shows that the intensity of a transition is proportional to the spectral integral of the cross section. In a similar fashion we can write the oscillator strength for absorption as

$$f_{abs} = (4\pi\epsilon_0) \frac{mc}{\pi e^2} \int \sigma_{12}(\nu) d\nu \quad (2.41)$$

where $\sigma_{12}(\nu)$ represents the absorption cross section of the transition from manifold 1 to manifold 2.

The intensities of the 4f-4f transitions can be determined by a set of three parameters Ω_2 , Ω_4 and Ω_6 that contain the complete description of the crystal field in a particular host. Once these parameters are determined for a particular ion-host combination, radiative transition rates between any pair of states can be obtained. This is done by using the Judd-Ofelt theory, and a brief treatment of this technique is presented in the next chapter.

2.3.3 Spectral shape of the 4f-4f transitions

The spectral shape of the optical transitions of rare earth ions in glasses is determined by three distinct processes. The crystal field of the lattice splits the energy levels of the free ion into $2J + 1$ individual Stark levels. The intensity and the energy position of the transitions between these levels vary from host to host, determining the major shape of the absorption and emission spectra, as has been discussed earlier in this section. The overall lineshape is the result of all transitions between the individual Stark levels. The total bandwidth caused by Stark splitting of a rare earth ion in glass is few hundred cm^{-1} and is in general larger in silicate (oxide) glass than in fluoride glass.

In addition to Stark splitting, the individual levels are homogeneously and inhomogeneously broaden, depending whether the transition width is the same or different for each ion. For rare earth ions in glass these two mechanisms contribute to the lineshape with comparable widths, on the order of tens to a hundred cm^{-1} at room temperature. The consequence of the spectral broadening is an overall spectral shape with unresolved Stark structure.

The two broadening mechanisms are very important not only in general, since they contribute to the lineshape of the transition, and therefore they determine the gain in an optical amplifier or laser, but in particular for my work, where the functions describing the homogeneous and inhomogeneous broadenings are critical for the proper prediction of the cross sections using the McCumber theory. In this section, discussion will be focused on the homogeneous and inhomogeneous broadening of the transition lineshape of rare earth ions in silicate and fluoride glasses.

Homogeneous broadening

In deriving the induced transition rate for a two level system interacting with an electromagnetic field, Eq.(2.17), it has been assumed that the interaction lasts an infinitely

long time. In this situation, the system absorbs or emits only at a single frequency equal to the frequency of the field, this interaction being described by a delta-function.

In real situations, the state of the system is perturbed by a number of factors that occur randomly in time, like spontaneous decay, interaction with the lattice phonons or with other similar ions, that shorten the lifetime of the excited state. The effect of the finite lifetime of the state of the system is homogeneous broadening, which is described by a Lorentzian function $g_L(\nu)$, given by

$$g_L(\nu) = \frac{1}{2\pi} \frac{\Delta\nu_H}{(\nu - \nu_0)^2 + (\Delta\nu_H/2)^2} \quad (2.42)$$

where ν_0 is the center frequency and $\Delta\nu_H$ is the *homogeneous width* of the transition, representing the full width measured at half maximum (FWHM).

Taking into account all the above factors, the lifetime τ of a given state 2 can be written as

$$\frac{1}{\tau} = \frac{1}{\tau_r} + \frac{1}{\tau_{nr}} + W_x \quad (2.43)$$

where $\tau_r = 1/A_{21}$ is the fluorescence lifetime, τ_{nr} is the nonradiative decay time due to the interaction of the ion with the phonons of the lattice and W_x is the nonradiative decay rate due to any other processes, like ion-ion interaction.

If only spontaneous decays were present, the ions in the state 2 would decay exponentially to a lower state 1 in a time of the order of hundred μs to milliseconds for most rare earth ion transitions. The measured lifetime is sometimes much shorter, however, due to the interaction with the lattice vibrations. If the energies of the different levels of the ion are close enough, they can be bridged by a few phonons of the lattice and this causes the ion to execute a transition between the two states by absorbing or emitting phonons of the lattice. The nonradiative rate decreases exponentially with the energy gap between the two levels. The larger the phonon energy of the host, the fewer phonons are required to bridge the gap, and the higher the probability

of decay through phonon interaction. Silicate glasses have high phonon energies ($\sim 1000 \text{ cm}^{-1}$) compared to the fluoride glasses ($\sim 400 \text{ cm}^{-1}$) [59], so the probability that an ion relaxes nonradiatively is higher in the silicate glasses. Therefore, for the same transition we expect in general that the homogeneous width is larger in silicate glass than in fluoride glass hosts. This is however not the limiting term that determines the spectral broadening; rather, it is the rapid phonon-induced relaxations within the same Stark multiplet, which at low temperature take place in times of picoseconds [60]. The amplitude of the lattice vibrations is greater at higher temperatures, so more phonons will interact with the ion. The homogeneous broadening increases quadratically with the temperature for both fluoride and oxide types of glasses [61]-[64], for temperatures above 10 K.

In low concentration samples, the rare earth ions interact very weakly with each other, due to the good shielding of the $4f$ electrons by the outer 5s and 5p layers. In high concentrations, the decay rate due to ion-ion interaction increases with the ion concentration, determining deviations from the exponential decay. The contribution to the spectral broadening is negligible compared to the phonon broadening.

Inhomogeneous broadening

Inhomogeneous broadening is determined by site-to-site variations in the local crystal field. As discussed earlier, the strength and the symmetry of the local field determines the energy and the strength of the optical transition. Site variations in the crystal field cause random variations in the frequency of the transition and in the oscillator strength. The overall lineshape is a superposition of all individual transitions characteristic to different ions. This process is described by a Gaussian function $g_G(\nu)$ given by

$$g_G(\nu) = \frac{1}{\Delta\nu_{IH}} \sqrt{\frac{4 \ln 2}{\pi}} \exp \left[-4 \ln 2 \left(\frac{\nu - \nu_0}{\Delta\nu_{IH}} \right)^2 \right] \quad (2.44)$$

where ν_0 is the average center frequency and $\Delta\nu_{IH}$ is the *inhomogeneous width* of the line, determined at half the maximum value (FWHM). The lineshape of the transition can be described by a Gaussian function only if the homogeneous profile is much narrower than the inhomogeneous one. The inhomogeneous linewidth is independent of the temperature and presents less variation with respect to host and dopant ion than the homogeneous one [20].

Fig.(2.5) shows the lineshape of a transition homogeneously and inhomogeneously broadened. For the same width of the line, the wings of the Lorentzian function are much

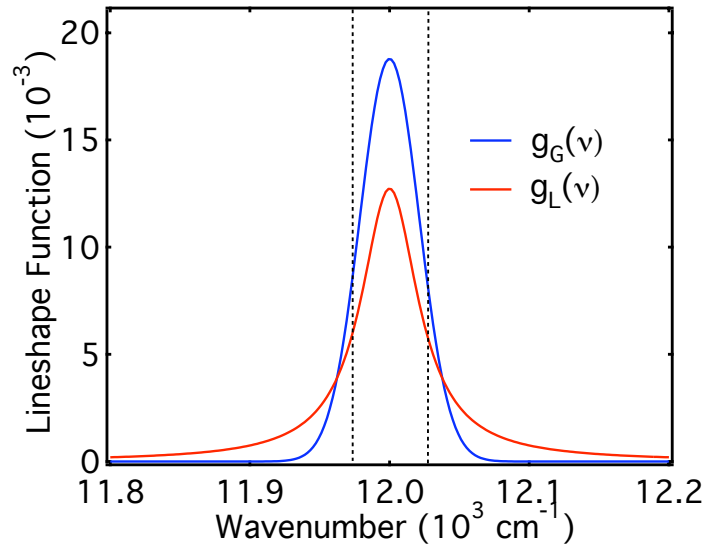


Figure 2.5: Normalized Gaussian and Lorentzian functions for the same FWHM

larger than the ones of the Gaussian function. The peak of the Gaussian is wider and rounder compared to the Lorentzian peak, which is sharper and lower in magnitude.

For most rare earth ions in glass, homogeneous and inhomogeneous widths have comparable values at room temperature. The lineshape in this case is described by a Voigt function $g_V(\nu)$ representing a convolution between the Gaussian and Lorentzian

functions:

$$g_V(\nu) = \int g_G(\nu') g_L(\nu - \nu') d\nu' \quad (2.45)$$

At low temperature, the homogeneous width is small and the line is predominantly inhomogeneously broaden, while at high temperature the homogeneous width dominates.

Chapter 3

Relationship between absorption and stimulated emission cross sections

The necessity of rigorous knowledge of the gain was underlined repeatedly in the first chapter. For those situations where the gain cannot be measured directly, it is very important to accurately determine the emission and absorption cross sections. There are also situations when either emission or absorption cross section are difficult to measure directly (absorption cross sections in fiber samples or between excited state levels, emission in high concentration samples where the spectral reabsorption of the fluorescence may affect the measured spectra). In those cases, one of the cross sections can be predicted if the other one is known from measurements. This is not an easy task however, for the complex structure of the rare earth doped systems (crystalline or glassy hosts) and for the general case, the detailed Stark structure and the oscillator strengths for individual Stark components are required, for each ion-host combination. For some particular situations, several theories are available that allow cross section prediction

from measured spectra. Three approximate situations are treated subsequently in this chapter: a) systems with large number of transitions for which absolute values of absorption cross sections can be measured directly (Judd-Ofelt theory), b) system with two degenerate levels (Fuchtbauer-Landenburg theory), and c) systems with two manifolds with narrow spectral width of individual Stark components (McCumber theory).

3.1 Judd-Ofelt theory

The Judd-Ofelt theory [11], [12] allows the determinations of the integrated cross section from absorption measurements of a number of ground state transitions. In this theory, the strength of any transition can be determined by a set of three parameters Ω_2 , Ω_4 and Ω_6 that contain the host dependence of the crystal field mixing of the states $4f^n$ and $4f^{n-1}5d$ of opposite parity. These two configurations are assumed to be $2J+1$ -fold degenerate and separated by an energy difference much larger than the energy spread due to the Russel-Saunders (L,S) coupling.

The first assumption of equal occupancy of the J levels is generally not satisfied at room temperature, especially for Stark splittings larger than 500 cm^{-1} . In media with low symmetry coordination, the approximation still remains valid, due to the fact that the crystal field components can be written as a linear combination of the different m_J levels, where m_J is the eigenvalue of the total angular momentum J . The theory however cannot be used at low temperatures.

The assumption that the SO splitting is small compared to the energy difference between the two electronic configurations is valid for most rare earth ions. Exceptions make ions like Pr^{3+} for which levels of the higher states $4f^{n-1}5d$ lie low inside the $4f^n$ state.

3.1.1 Determination of the Judd-Ofelt parameters using standard fitting procedure

In the Judd-Ofelt theory, the electric dipole oscillator strength for a transition between levels i and j of two different J manifolds can be written as [18]

$$f_{ij}^e = \frac{8\pi^2 m \nu \chi_e}{3h(2J+1)n^2} \sum_{t=2,4,6} \Omega_t |\langle i | \hat{U}^{(t)} | j \rangle|^2 \quad (3.1)$$

where $2J+1$ is the degeneracy of the originating level of the transition, $\chi_e = n(n^2+2)^2/9$ is the Dexter correction for the local field, and $\langle i | \hat{U}^{(t)} | j \rangle$ are the doubly reduced matrix elements of the *tensor transition operator*. They represent the radial contribution of the electric dipole operator matrix elements $\mu_{ij}^e \equiv \langle i | \hat{\mu}_e | j \rangle$ and they have been tabulated for lanthanide ions by Weber [15] and Carnal et al. [65]-[68].

The oscillator strengths can be determined directly from absorption data according to Eq.(2.41), by measuring the integrated absorption cross sections for a number of ground state transitions. The set of coefficients (Ω_2 , Ω_4 , Ω_6) are obtained by running a least-square fit procedure that minimizes the absolute difference $(f^{calc} - f^{meas})^2$ between the calculated and the measured oscillator strengths for all available transitions. Once calculated, they allow the determination of absorption or emission integrated cross sections for transitions between any levels.

Although very powerful in predicting quantitative information about transitions that are not accessible for direct measurements (e.g. absorption spectra from excited states), the Judd-Ofelt technique provides inaccurate results (unrealistic negative oscillator strengths) when not sufficient transitions are used in the fitting procedure, or when the hypersensitive transitions are included. To improve the accuracy of the technique, the branching ratios $a_l = A_l/A_{tot}$ determined from fluorescence measurements have been included in the fitting procedure in order to increase the effective number of measured transitions [18]. A_l represents the spontaneous emission rate for the transition l and A_{tot}

is the total spontaneous rate of the manifold from which the emission originates. Some other studies [22]-[24] minimize the relative differences between the calculated and the measured oscillator strengths. The Judd-Ofelt parameters are now tabulated for all rare earth ions in various host matrices. A good review of the Judd-Ofelt theory, together with a comprehensive list of the intensity parameters is presented by Gorller-Walrand and Binnemans in [21].

3.1.2 Analytical determination of Judd-Ofelt parameters including branching ratios

In this work a new method of analytically calculating the intensity parameters has been developed, that incorporates the branching ratios from fluorescence measurements. This method is a generalization of the one described by Quimby [18] for determination of the Judd-Ofelt coefficients from absorption data only. It allows the exact calculation of the (Ω_2 , Ω_4 , Ω_6) set by running a very simple, short computer program for any number of measured transitions. As was shown in ref. [18], including the branching ratios in the determination of the intensity parameters increases the accuracy of the Judd-Ofelt technique.

The absolute difference Δ between the calculated and the measured oscillator strengths for a number of N_a absorption and N_e emission transitions is

$$\Delta = \sum_l^{N_a+N_e} (f_l^{calc} - f_l^{meas})^2 \quad (3.2)$$

where $N_a + N_e$ is the total number of transitions measured. Eq.(3.1) can be written in a simplified notation, by introducing the following parameters:

$$U_{tl} = |\langle i | \hat{U}^{(t)} | j \rangle|^2 \quad (3.3)$$

$$K_l = \left[\frac{8\pi^2 m \nu \chi_e}{3h(2J+1)n^2} \right]_l$$

$$x_l = K_l U_{2l}, \quad y_l = K_l U_{4l} \quad \text{and} \quad z_l = K_l U_{6l}$$

with $t = 2, 4, 6$ and $l = 1$ to $N_a + N_e$. The calculated oscillator strength for a particular transition l becomes

$$f_l^{calc} = \Omega_2 x_l + \Omega_4 y_l + \Omega_6 z_l \quad (3.4)$$

Common fluorescence measurements do not provide absolute values of the oscillator strengths, mainly because the signal collected by the photodetectors is only proportional to the photon flux, and unless other calibration methods are used, only relative spectra are usually measured. Consider that all N_e emission transitions originate from the same

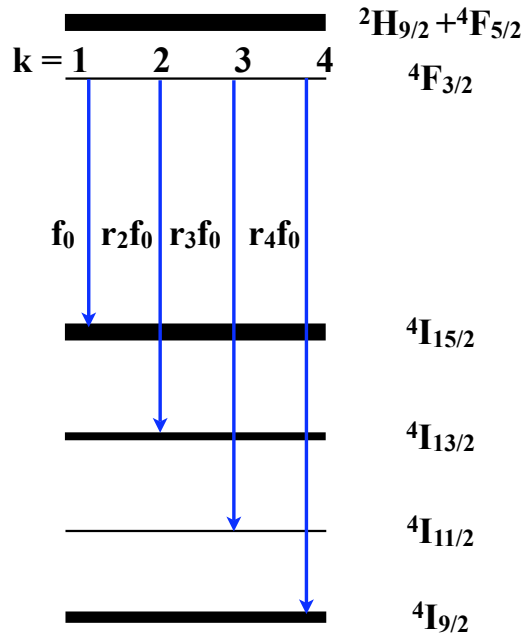


Figure 3.1: Representation of the branching ratios for Nd^{3+} fluorescence transitions

excited level¹. The branching ratio a_k for the k^{th} emission transition defined earlier can

¹The method can be generalized even more by taking into account a number of excited state levels, though increasing the number of transitions and also of the unknowns.

be expressed in terms of oscillator strengths by the use of Eq.(2.39). The ratio r_{kl} between the oscillator strengths of two emission transitions k and l can be written as

$$r_{kl} = \frac{f_k}{f_l} = \left[\frac{\lambda_k/n(\lambda_k)}{\lambda_l/n(\lambda_l)} \right]^2 \left(\frac{A_k}{A_l} \right) \quad (3.5)$$

where the refractive index $n(\lambda)$ at each particular wavelength has been considered. The emission oscillator strengths can all be related to the same reference value $f_l \equiv f_0$. For k varying from 1 to N_e , the oscillator strengths can be written as

$$f_k = r_k f_0 \quad (3.6)$$

With all these parameters implemented, the absolute difference Δ becomes

$$\Delta = \sum_{l=1}^{N_a} (\Omega_2 x_l + \Omega_4 y_l + \Omega_6 z_l - f_l^{meas})^2 + \sum_{k=N_a+1}^{N_e} (\Omega_2 x_k + \Omega_4 y_k + \Omega_6 z_k - r_k f_0)^2 \quad (3.7)$$

The goal is to determine the four parameters Ω_2 , Ω_4 , Ω_6 and f_0 for which the function Δ has minimum value. This is achieved by requiring

$$\frac{\partial \Delta}{\partial \Omega_2} = 0, \quad \frac{\partial \Delta}{\partial \Omega_4} = 0, \quad \frac{\partial \Delta}{\partial \Omega_6} = 0 \quad \text{and} \quad \frac{\partial \Delta}{\partial f_0} = 0 \quad (3.8)$$

which after derivation can be rearranged as

$$\begin{cases} \Omega_2(XX) + \Omega_4(XY) + \Omega_6(XZ) - f_0(XR) &= XF \\ \Omega_2(YX) + \Omega_4(YY) + \Omega_6(YZ) - f_0(YR) &= YF \\ \Omega_2(ZX) + \Omega_4(ZY) + \Omega_6(ZZ) - f_0(ZR) &= ZF \\ \Omega_2(RX) + \Omega_4(RY) + \Omega_6(RZ) - f_0(RR) &= 0 \end{cases}$$

where

$$\begin{aligned} XX &= \sum_{l=1}^{N_a+N_e} x_l x_l, & RX &= XR = \sum_{k=1}^{N_e} x_k r_k, & XF &= \sum_{l=1}^{N_a} x_l f_l^{meas} \\ XY &= YX = \sum_{l=1}^{N_a+N_e} x_l y_l, & RY &= YR = \sum_{k=1}^{N_e} y_k r_k, & YF &= \sum_{l=1}^{N_a} y_l f_l^{meas} \\ XZ &= ZX = \sum_{l=1}^{N_a+N_e} x_l z_l, & RZ &= ZR = \sum_{k=1}^{N_e} z_k r_k, & ZF &= \sum_{l=1}^{N_a} z_l f_l^{meas} \\ YY &= \sum_{l=1}^{N_a+N_e} y_l y_l & RR &= \sum_{k=1}^{N_e} r_k r_k \\ ZZ &= \sum_{l=1}^{N_a+N_e} z_l z_l \end{aligned}$$

The solution of the above linear system of linear equations is

$$\Omega_2 = \frac{1}{D} \begin{vmatrix} XF & XY & XZ & XR \\ YF & YY & YZ & YR \\ ZF & ZY & ZZ & ZR \\ 0 & RY & RZ & RR \end{vmatrix},$$

$$\Omega_4 = \frac{1}{D} \begin{vmatrix} XX & XF & XZ & XR \\ YX & YF & YZ & YR \\ ZX & ZF & ZZ & ZR \\ RX & 0 & RZ & RR \end{vmatrix},$$

$$\Omega_6 = \frac{1}{D} \begin{vmatrix} XX & XY & XF & XR \\ YX & YY & YF & YR \\ ZX & ZY & ZF & ZR \\ RX & RY & 0 & RR \end{vmatrix},$$

and

$$f_0 = \frac{1}{D} \begin{vmatrix} XX & XY & XZ & XF \\ YX & YY & YZ & YF \\ ZX & ZY & ZZ & ZF \\ RX & RY & RZ & 0 \end{vmatrix}$$

where D is the determinant of the homogeneous system of equations given by

$$D = \begin{vmatrix} XX & XY & XZ & XR \\ YX & YY & YZ & YR \\ ZX & ZY & ZZ & ZR \\ RX & RY & RZ & RR \end{vmatrix}$$

This new formalism allows the exact determination of the Judd-Ofelt parameters by running a very short program, in only seconds, for any number of absorption and emission transitions.

3.2 Fuchtbauer-Ladenburg (FL) theory

The original Fuchtbauer-Ladenburg (FL) formula relates the absorption coefficient to the Einstein A and B coefficients for a two degenerate level system, for situations when the refractive index does not vary rapidly across the lineshape of the transition ($c_n = c/n$). Several forms of the FL relation can be derived from these assumptions and they will be discussed in the next paragraphs.

3.2.1 Derivation of the FL relation

Consider a two level system 1, 2 with the degeneracies g_1 and g_2 , interacting with a nearly monochromatic beam. The induced transition rates are proportional to the total energy density of the incident beam according to Eq.(2.15) and Eq.(2.16).

The number of photons per unit volume per unit time that add up to the incident beam is given by the rate equation

$$\frac{dN}{dt} = B_{21}g_{em}(\nu_p)\rho N_2 - B_{12}g_{abs}(\nu_p)\rho N_1 \quad (3.9)$$

where ν_p is the pump frequency. The number of photons emitted spontaneously has again been neglected since they are emitted in all directions and do not contribute significantly to the amplification.

As the light propagates in the amplifying medium, it gets absorbed according to *Beer's Law*: $dI(z)/dz = -\alpha(\nu)I(z)$, where $I(z)$ is the intensity of light at the location z in the medium and $\alpha(\nu)$ is the absorption coefficient. Writing the change in the energy density per unit time time as in relation (2.26) and following a similar approach as in section (2.2), the absorption coefficient can then be written in terms of the populations of the two levels and the the Einstein B coefficients as

$$\alpha(\nu) = (B_{12}N_1g_{abs}(\nu_p) - B_{21}N_2g_{em}(\nu_p)) \frac{h\nu}{c/n} \quad (3.10)$$

Using the relationship between the Einstein B coefficients for degenerate levels $g_1 B_{12} = g_2 B_{21}$ given in (2.23), the absorption coefficient can then be written as

$$\alpha(\nu) = \left(\frac{g_2}{g_1} B_{21} N_1 g_{abs}(\nu_p) - B_{21} N_2 g_{em}(\nu_p) \right) \frac{h\nu}{c/n} \quad (3.11)$$

Integrating over the frequencies covered by the absorption line, the above equation becomes

$$\int \alpha(\nu) d\nu = \int \left(\frac{g_2}{g_1} N_1 g_{abs}(\nu_p) - N_2 g_{em}(\nu_p) \right) \frac{B_{21} h\nu}{c/n} d\nu \quad (3.12)$$

The quantity $g(\nu_p) d\nu$ give the relative probability that the atoms absorb or emit within the range $d\nu$ about the pump frequency ν_p . This is equivalent with

$$g_{abs}(\nu_p) d\nu = \frac{dN_{1\nu}}{N_1} \quad \text{and} \quad g_{em}(\nu_p) d\nu = \frac{dN_{2\nu}}{N_2} \quad (3.13)$$

where $dN_{2\nu}$ and $dN_{1\nu}$ are the number of atoms capable of emitting or absorbing within the range $d\nu$ about the frequency ν_p . Inserting these expressions into Eq.(3.12) and assuming narrow spectral line where the frequency can be replaced by the peak frequency ν_0 , the expression for the integrated absorption coefficient can be written as

$$\int \alpha(\nu) d\nu = \left(\frac{g_2}{g_1} N_1 - N_2 \right) \frac{B_{21} h\nu_0}{c/n} \quad (3.14)$$

This is the Fuchtbauer-Ladenburg formula. It relates the the integrated absorption coefficient to the Einstein coefficients and the populations of the levels involved in the absorption process.

3.2.2 Equivalent forms of the FL relation

The spectral distribution of the absorption coefficient can be determined according to Eq.(3.14) by using the lineshape functions for emission and absorption as

$$\alpha(\nu) = \left(\frac{g_2}{g_1} N_1 g_{abs}(\nu) - N_2 g_{em}(\nu) \right) \frac{B_{21} h\nu_0}{c/n} \quad (3.15)$$

When population inversion is achieved, this equation defines the optical gain at the frequency ν . It is useful to express the gain in terms of measurable quantities, like $A_{21} = 1/\text{radiative lifetime}$. For this, we can use the Einstein's relation Eq.(2.14), which is an exact relation for any two individual levels, 1 and 2. The above equation then becomes

$$\alpha(\nu) = \frac{A_{21}c^2}{8\pi n^2 \nu_0^2} \left(N_2 g_{em}(\nu) - \frac{g_2}{g_1} N_1 g_{abs}(\nu) \right) = \sigma_{21}(\nu) N_2 - \sigma_{12}(\nu) N_1 \quad (3.16)$$

where the stimulated emission and absorption cross sections have the following expressions

$$\sigma_{21}(\nu) = \frac{A_{21}c^2}{8\pi n^2 \nu_0^2} g_{em}(\nu) \quad (\text{FL Relation Emission 1}) \quad (3.17)$$

$$\sigma_{12}(\nu) = \frac{g_2}{g_1} \frac{A_{21}c^2}{8\pi n^2 \nu_0^2} g_{abs}(\nu) \quad (\text{FL Relation Absorption 1}) \quad (3.18)$$

Integrating the above two equations, we can write the relationship between the emission and absorption cross sections as

$$g_2 \int \sigma_{21}(\nu) d\nu = g_1 \int \sigma_{12}(\nu) d\nu \quad (\text{FL Reciprocity Relation 1}) \quad (3.19)$$

To understand the validity of the above relations, we need to review the conditions under which they were derived. The first approximation (*FL approximation*) was made when we used the relationship between the Einstein B coefficients Eq(2.23). This relation is valid either when the individual levels of the two manifolds 1 and 2 are equally populated, or when the they have the same induced transition rate. Also, the last equations, (3.14)-(3.19) have been obtained under the assumption of narrow atomic transition, where the frequency does not vary significantly across the spectral line, and was replaced by the peak frequency. A very important remark should be made here. The equation relating the emission cross section to the spontaneous transition rate (3.17) is not affected by the FL assumption relating the Einstein B coefficients, so this equation is valid to study optical transitions of rare earths in crystalline hosts.

The above equations can be written in terms of a dimensionless parameter f representing the *oscillator strength* of the transition. The oscillator strength is defined as

$$f = 4\pi\epsilon_0 \frac{mc}{\pi e^2} \int \sigma(\nu) d\nu \quad (3.20)$$

where m and e are the mass and the charge of an electron and ϵ_0 is the electrical permittivity of the free space. The FL reciprocity relation can be written as

$$g_1 f_{abs} = g_2 f_{em} \quad (3.21)$$

which represents another expression of the FL reciprocity relation.

A more general form of the above equations can be obtained directly from the expression of the absorption coefficient as given by Eq(3.11). Replacing B_{21} from Einstein's relation and writing the absorption coefficient as $\alpha(\nu) = \sigma_{12}(\nu)N_1 - \sigma_{21}(\nu)N_2$, and following the same procedure as above, we obtained the integrated FL relations:

$$\int \nu^2 \sigma_{21}(\nu) d\nu = \frac{A_{21}c^2}{8\pi n^2} \quad (FL \text{ Relation Emission 2}) \quad (3.22)$$

$$\int \nu^2 \sigma_{12}(\nu) d\nu = \frac{g_2}{g_1} \frac{A_{21}c^2}{8\pi n^2} \quad (FL \text{ Relation Absorption 2}) \quad (3.23)$$

The two cross sections can then be related as

$$g_2 \int \nu^2 \sigma_{21}(\nu) d\nu = g_1 \int \nu^2 \sigma_{12}(\nu) d\nu \quad (FL \text{ Reciprocity Relation 2}) \quad (3.24)$$

We should again underline the fact that, while the FL reciprocity relation Eq.(3.24) and the equation (3.23) relating the integrated absorption cross section to the radiative transition rate A_{21} are approximate relations, Eq.(3.22) connecting the integrated emission cross section to the fluorescence rate is an exact relation.

Starting with Eq.(3.17) for individual Stark levels and assuming steady-state low level excitation, Aull and Jenssen [33] derived an expression that allows the emission

cross section be calculated by measuring the spectral fluorescence intensity and the fluorescence lifetime t_r . The stimulated emission cross section is given by

$$\sigma_{em}(\lambda) = \frac{\eta\lambda^5}{t_r(\int \lambda I(\lambda)d\lambda)f_i8\pi n^2c}I(\lambda) \quad (FL\ Relation\ Emission\ 3) \quad (3.25)$$

where η is the radiative quantum efficiency of the upper states, $I(\lambda)$ is the total fluorescence signal, and f_i is the fraction of the pumped population in the particular state i, given by Bolzmann distribution. This equation has been obtained in conditions of narrow linewidths, to describe optical transitions of rare earth ions in crystals, but its validity can be extended to more broad transitions, as we shall see in the next chapter. It is extremely useful and provides reliable cross section spectra from routine fluorescence measurements.

3.3 McCumber theory

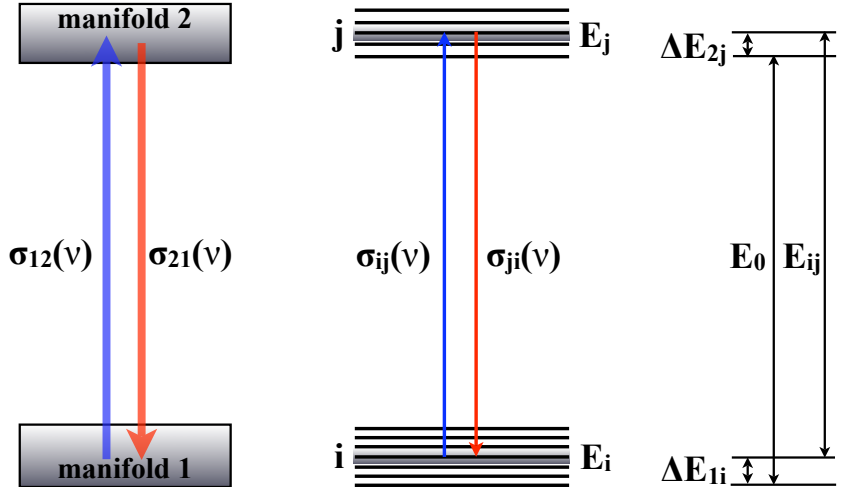
The theory of McCumber [46] generalizes the Einstein relations for broadband transitions, which are typical for rare earth ions in glassy environments. The theory shows that at any frequency, the absorption, spontaneous emission and stimulated emission spectra are uniquely related by very simple relations. These relations are obtained in the context of narrow energy widths of the individual Stark levels and of thermal equilibrium between the impurity ions and the host. In this section, the derivations of the generalized Einstein relations, as presented by McCumber, will be emphasized in some detail, together with potential difficulties and situations when the theory breaks down.

3.3.1 Generalization of Einstein relations for broadband spectra

Consider a system of ion impurities uniformly distributed in a homogeneous dielectric medium of volume V . Assume that the populations per unit volume within different Stark manifolds can be independently specified, and the total population among all levels is fixed (and equal to the ion concentration). Within each manifold, the individual energy levels are in thermal equilibrium, which requires that the time taken to establish thermal equilibrium within the manifold is short compared to the lifetime of that manifold.

Consider two Stark manifolds 1 and 2, within which the individual levels are labeled by i and j , with $i = 1$ to $2J_1 + 1$ for the lower manifold and $j = 1$ to $2J_2 + 1$ for the upper one², where J_1 and J_2 are the quantum numbers of the two states. This situation is illustrated in fig.(3.2). We can write the absorption and emission cross sections for

²This is true only for ions with even number of electrons. For ions with odd number of electrons, the energy levels are Krammers degenerated resulting in a total of $(2J + 1)/2$ distinct levels, assuming low symmetry environment



$$\sigma_{21}(v) = \sigma_{12}(v)\exp[\epsilon - h v/k_B T] \quad \sigma_{ij}(v) = \sigma_{ji}(v) \quad \Delta E_{2j} = \Delta E_{1i} + E_{ij} - E_0$$

Figure 3.2: Representation of optical transitions between two Stark manifolds in a rare earth doped system

the manifolds 1 and 2 by taking into account all individual contributions of each level as follows

$$N_1\sigma_{12}(\nu) = \sum_{i,j} N_{1i}\sigma_{ij}(\nu) \quad (3.26)$$

$$N_2\sigma_{21}(\nu) = \sum_{i,j} N_{2j}\sigma_{ji}(\nu) \quad (3.27)$$

where N_1 and N_2 are the total populations of the two manifolds and N_{1i} and N_{2j} are the populations of the individual levels i and j .

In thermal equilibrium, the population distribution among different levels is described by Boltzmann statistics. The ion concentration N_{Mk} on any k level within a manifold M can be written as

$$N_{Mk} = N_M \frac{e^{-\Delta E_{Mk}/k_B T}}{\sum_k e^{-\Delta E_{Mk}/k_B T}} \quad (3.28)$$

where N_M is the total population of the manifold and ΔE_{Mk} is the energy separation

between k and the lowest level of the manifold. With this, the two cross sections can be written as

$$\sigma_{12}(\nu) = \frac{1}{Z_1} \sum_{i,j} e^{-\Delta E_{1i}/k_B T} \sigma_{ij}(\nu) \quad (3.29)$$

$$\sigma_{21}(\nu) = \frac{1}{Z_2} \sum_{i,j} e^{-\Delta E_{2j}/k_B T} \sigma_{ji}(\nu) \quad (3.30)$$

where $Z_1 = \sum_i e^{-\Delta E_{1i}/k_B T}$ and $Z_2 = \sum_j e^{-\Delta E_{2j}/k_B T}$ are the partition functions of the two manifolds. These two equations are exact and valid for any systems of ions in thermal equilibrium with the host.

The absorption and stimulated emission cross sections for transitions between the individual Stark components i and j can be written according to Eq.(2.32) as

$$\sigma_{ij}(\nu) = \frac{h\nu}{I} W_{ij}(\nu) \quad (3.31)$$

and

$$\sigma_{ji}(\nu) = \frac{h\nu}{I} W_{ji}(\nu) \quad (3.32)$$

where I is the intensity of the light beam of frequency ν at a certain location inside the medium and W_{ij} and W_{ji} are the induced absorption and emission transition rates between the levels i and j .

Assuming infinitely sharp energy levels interacting with a plane wave of angular frequency $\omega = 2\pi\nu$, the induced transition rates can be expressed from Eq.(A.23) and the absorption and emission cross sections become

$$\sigma_{ij}(\nu) = \frac{\pi^2}{h^2} \frac{h\nu}{I} |V_{ij}^0|^2 \delta(\nu - \nu_{ij}) \quad (3.33)$$

$$\sigma_{ji}(\nu) = \frac{\pi^2}{h^2} \frac{h\nu}{I} |V_{ji}^0|^2 \delta(\nu - \nu_{ij}) \quad (3.34)$$

where $|V_{ij}^0|^2$ and $|V_{ji}^0|^2$ are the square matrix elements of the time independent part of the interaction potential connecting the states i and j , and $\nu_{ij} = (E_{2j} - E_{1i})/k_B T$ is the frequency of the atomic transition $i \leftrightarrow j$.

Using the above equations into Eq.(3.29) and Eq.(3.30) we can relate the emission and absorption cross sections by calculating the ratio

$$\frac{Z_2\sigma_{21}(\nu)}{Z_1\sigma_{12}(\nu)} = \frac{\sum_{i,j} e^{-\Delta E_{2j}/k_B T} |V_{ij}^0|^2 \delta(\nu - \nu_{ij})}{\sum_{i,j} e^{-\Delta E_{1i}/k_B T} |V_{ji}^0|^2 \delta(\nu - \nu_{ij})} \quad (3.35)$$

Writing the energy of the level j as $\Delta E_{2j} = \Delta E_{1i} + h\nu_{ij} - E_0$, where E_0 is the separation between the two manifolds, and summing over all the states, the only nonzero terms are those for which ν_{ij} matches the frequency of the field ν . Equation (3.35) becomes

$$\frac{Z_2\sigma_{21}(\nu)}{Z_1\sigma_{12}(\nu)} = \frac{|V_{ij}^0|^2 e^{-\Delta E_{1i}/k_B T} e^{(E_0-h\nu)/k_B T}}{|V_{ji}^0|^2 e^{-\Delta E_{1i}/k_B T}} \quad (3.36)$$

The square matrix elements $|V_{ji}^0|^2$ and $|V_{ij}^0|^2$ are equal because the Hamiltonian describing the interaction between the electromagnetic field and the system is real. The relationship between the absorption and the stimulated emission cross section can then be simplified to

$$\sigma_{21}(\nu) = \frac{Z_1}{Z_2} \sigma_{12}(\nu) e^{(E_0-h\nu)/k_B T} \quad (3.37)$$

Defining an effective energy ϵ such that

$$e^{\epsilon/k_B T} = \frac{Z_1}{Z_2} e^{E_0/k_B T} \quad (3.38)$$

the above relation becomes

$$\sigma_{21}(\nu) = \sigma_{12}(\nu) e^{(\epsilon-h\nu)/k_B T} \quad (\text{McCumber Relation}) \quad (3.39)$$

which represents the **McCumber** or **reciprocity relation** for the absorption and stimulated emission cross sections. This is the generalization of the relationship between Einstein B coefficients, Eq.(2.13). Unlike the FL reciprocity relation which is an integral expression, the McCumber formula relates the absorption and stimulated emission spectra at the same frequency. This allows cross section predictions, absolute values, as well as spectral distributions.

In order to relate the stimulated and spontaneous emission spectra, we need to define a function $f_\lambda(\nu)$ as the spontaneous transition rate of the λ -polarized radiation of frequency ν emitted per unit frequency interval $d\nu$ per unit solid angle $d\Omega$. The total spontaneous transition rate A_{21} can be determined by integrating $f_\lambda(\nu)$ over all frequencies and the solid angle, and summing over all polarization as follows

$$A_{21} = \sum_\lambda \int d\Omega \int d\nu f_\lambda(\nu) \quad (3.40)$$

The stimulated transition rate $W_{21/12}^f(\nu)$ of the same λ -polarized radiation of frequency ν per unit frequency interval in the solid angle $d\Omega$, can be written as a function of the cross section from Eq.(2.32) as

$$W_{21}^f(\nu) = \sigma_{21}(\nu) c_n \frac{\aleph_{em}}{V} \quad (3.41)$$

$$W_{12}^f(\nu) = \sigma_{12}(\nu) c_n \frac{\aleph_{abs}}{V} \quad (3.42)$$

where the index f marks the fact that this transition rate is a fractional quantity, within the specified range, \aleph_{em} and \aleph_{abs} are the number of photons emitted and absorbed in this range, respectively, and V is the radiated volume of the dielectric.

We can write \aleph_{em} explicitly as the number of modes $p(\nu)$ times the average number of photons in each mode $n(\nu)$. In thermal equilibrium, the average occupation number is given by the Bose-Einstein distribution function

$$n(\nu) = \frac{1}{e^{h\nu/k_B T} - 1} \quad (3.43)$$

The number of λ -polarized modes in the solid angle $d\Omega$ of a rectangular cavity of volume V , for which the wave vector k lies between 0 and $2\pi\nu/c_n$ can be found by dividing the volume of the sphere determined by the vector \mathbf{k} to the volume of the unit cell determining the standing waves in the cavity. Since the wave vector has positive magnitude, only the contribution of the first octant will be considered. This can be written as

$$p(\nu) = \frac{1}{8} \frac{\frac{4}{3}\pi(2\pi\nu/c_n)^3}{4\pi(\pi/l_x)(\pi/l_y)(\pi/l_z)} = \frac{\nu^3}{3c_n^3} V \quad (3.44)$$

Using the above considerations, equations (3.42) and (3.41) become

$$W_{21}^f(\nu) = \sigma_{21}(\nu) \frac{\nu^2}{c_n^2} n(\nu) \quad (3.45)$$

$$W_{12}^f(\nu) = \sigma_{12}(\nu) \frac{\nu^2}{c_n^2} n(\nu) \quad (3.46)$$

The detailed balance argument for the manifolds 1 and 2 can be written as

$$N_1 \sigma_{12}(\nu) \frac{\nu^2}{c_n^2} n(\nu) = N_2 f_\lambda(\nu) + N_2 \sigma_{21}(\nu) \frac{\nu^2}{c_n^2} n(\nu) \quad (3.47)$$

Using Eqs.(3.28), (3.39) and (3.43) into the above, we obtain

$$f_\lambda(\nu) = \sigma_{21}(\nu) \frac{\nu^2}{c_n^2} \quad (3.48)$$

which is the McCumber formula relating the fluorescence and the stimulated emission spectra. This is a generalization of the Einstein relation for A and B coefficients. To calculate the total spontaneous transition rate we use Eq.(3.40) and find

$$A_{21} = \sum_\lambda \int d\Omega \int d\nu f_\lambda(\nu) = \frac{2 \cdot 4\pi}{c_n^2} \int \nu^2 \sigma_{21}(\nu) d\nu \quad (3.49)$$

which is equivalent with

$$\int \nu^2 \sigma_{21}(\nu) d\nu = \frac{c_n^2}{8\pi} A_{21} \quad (3.50)$$

This relation is the same as the exact FL expression relating the integrated emission cross section to the fluorescence lifetime.

Using the same strategy as for the spontaneous transition rate, the Einstein B_{21} coefficient can be obtained writing the total stimulated transition rate for narrow atomic transitions (2.8) as

$$B_{21} = \frac{1}{\rho_\nu(\nu_0)} \sum_\lambda \int d\Omega \int d\nu W_{21}^f(\nu) = \frac{1}{\rho_\nu(\nu_0)} \sum_\lambda \int d\Omega \int d\nu \sigma_{21}(\nu) \frac{\nu^2}{c_n^2} n(\nu) \quad (3.51)$$

where $\rho_\nu(\nu_0)$ is the spectral distribution of the blackbody spectrum at the center frequency of the atomic transition. For very sharp spectral lines $n(\nu)$ can be evaluated at

ν_0 and taken outside the integral. Expressing $\rho_\nu(\nu_0)$ from Plank's formula (2.6) and using equations (3.43) and (3.48), the above equation can be reduced to Einstein's relation (2.14).

3.3.2 Range of validity of the McCumber theory

In order to understand the applicability of the McCumber relation in predicting absorption and emission cross section spectra from each other when one is known from direct measurements, we will write the expressions of the two cross sections for a general case. For this, we consider transitions between two manifolds 1 and 2 as represented in fig.(3.2), consisting in individual levels that are not infinitely narrow, but rather have a finite spectral width determined by the broadening mechanism specific to a particular ion in a certain local environment. For purely homogeneously or inhomogeneously broadened transitions, the individual cross sections $\sigma_{ij}^H(\nu)$ and $\sigma_{ij}^{IH}(\nu)$ are respectively described by the corresponding lineshape functions $g_L(\nu - \nu_{ij})$ and $g_G(\nu - \nu_{ij})$ using Eq.(2.29) and (2.30), as

$$\sigma_{ij}^H(\nu) = \sigma_{0ij}(\nu_{ij})g_{0L}(\nu - \nu_{ij}) \quad (3.52)$$

$$\sigma_{ij}^{IH}(\nu) = \sigma_{0ij}(\nu_{ij})g_{0G}(\nu - \nu_{ij}) \quad (3.53)$$

where ν_{ij} is the peak frequency, $\sigma_{0ij}(\nu_{ij})$ is the peak cross section and $g_0(\nu - \nu_{ij})$ is the lineshape function normalized to unity at the transition peak (defined such that $g_{ij}(\nu - \nu_{ij}) = g(\nu_{ij})g_0(\nu - \nu_{ij})$). Note that rel.(3.53) is valid for homogeneous widths much smaller than site to site variations in the center frequency, and also for negligible variations in oscillator strengths from site to site.

The effective emission and absorption cross sections for the transition between the two manifolds can be written according to Eqs. (3.29) and (3.30) as a function of the

individual cross sections of the different $i \leftrightarrow j$ transitions as

$$\sigma_{21}(\nu) = \frac{1}{Z_2} \sum_{i,j} e^{-\Delta E_{2j}/k_B T} \sigma_{0ji}(\nu_{ij}) g_0(\nu - \nu_{ij}) \quad (3.54)$$

$$\sigma_{12}(\nu) = \frac{1}{Z_1} \sum_{i,j} e^{-\Delta E_{1i}/k_B T} \sigma_{0ij}(\nu_{ij}) g_0(\nu - \nu_{ij}) \quad (3.55)$$

Again, the relationship between the energy levels is written as $\Delta E_{2j} = \Delta E_{1i} + h\nu_{ij} - E_0$ and adding and subtracting $h\nu$ at the right hand side of this, the two cross sections can be connected as sections of the different $i \leftrightarrow j$ transitions as

$$\sigma_{21}(\nu) = \frac{Z_1}{Z_2} \sigma_{12}(\nu) e^{(E_0 - h\nu)/k_B T} \left[\frac{\sum_{i,j} e^{-\Delta E_{1i}/k_B T} \sigma_{0ji}(\nu_{ij}) g_0(\nu - \nu_{ij}) e^{-(E_{ij} - h\nu)/k_B T}}{\sum_{i,j} e^{-\Delta E_{1i}/k_B T} \sigma_{0ij}(\nu_{ij}) g_0(\nu - \nu_{ij})} \right] \quad (3.56)$$

For spectral widths $|E_{ij} - h\nu| \ll k_B T$, the above equation leads to the McCumber relation (3.39). Typical transition widths [20], [61]-[64] for rare earth ions in glassy hosts at room temperature are in the range of $20-80 \text{ cm}^{-1}$, small compared to the value of $k_B T \sim 200 \text{ cm}^{-1}$. This approximation is though reasonable, making this theory very valuable for describing rare earth transitions at room temperature.

Effectiveness in predicting correct cross section spectra

The McCumber relation is extremely useful in connecting the absorption and emission cross sections, especially in predicting spectral shapes of transitions that are experimentally inaccessible. It is the only of the three discussed theories that allows determination of the spectral shape of a cross section from direct measurements of the reciprocal one. To analyze the absorption and emission cross sections we examine the McCumber relation $\sigma_{21}(\nu) = \sigma_{12}(\nu) e^{(\epsilon - h\nu)/k_B T}$ (3.39) and rewrite it as

$$\sigma_{21}(\nu) = \frac{Z_1}{Z_2} e^{E_0/k_B T} \sigma_{12}(\nu) e^{-h\nu/k_B T} \quad (3.57)$$

The spectral difference between emission and absorption cross sections observed experimentally as in fig.(3.3) can be understood by examining the above relations. The Stark

splitting for a rare earth ion in crystal or glass is several hundred cm^{-1} , larger than the value of $k_B T$, which implies that according to the McCumber relation, the two cross sections are shifted in frequency with respect to each other. They are equal for a unique value of the frequency equal to ϵ/h , at higher frequency (shorter wavelength) the absorption exceeding the emission cross section, while at lower frequency (longer wavelength) the emission cross section being greater. The factor $(Z_1/Z_2)\exp(E_0/k_B T)$ can be deter-

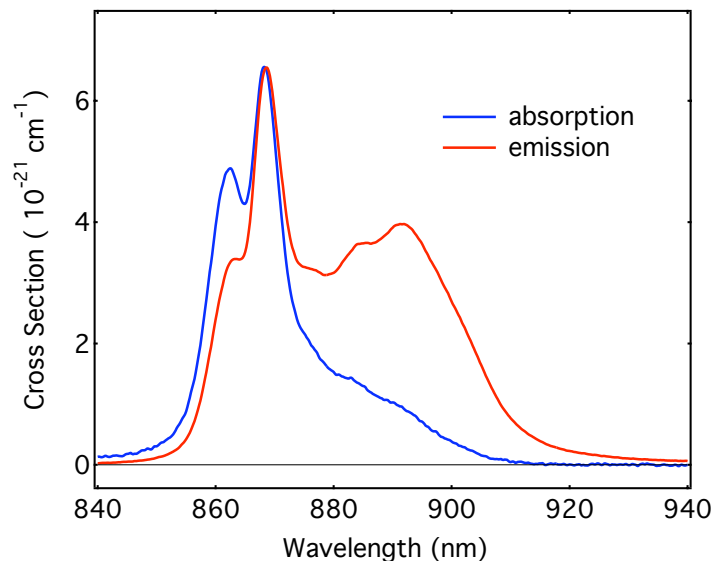


Figure 3.3: Spectral shape of measured absorption and emission cross sections for Nd in fluoride glass. The emission cross section has been rescaled to the same peak value as the absorption cross section.

mined only if the detailed Stark structure of a particular ion-host combination is known. This factor, however, is frequency independent and does not affect the spectral shape of the cross section. This is of a greatest importance, since it implies that the McCumber formula has the ability to predict spectral shapes of emission or absorption cross sections from each other, even when only relative spectra are available from measurements.

In order to determine absolute values of the cross sections, knowledge of the electronic parameters of the system is required. Since the detailed Stark structure of a

particular ion varies from host to host, low temperature measurements are needed for each ion-host combination. In glassy hosts, the individual peaks cannot be resolved, since they are masked by the inhomogeneous linewidth, which is temperature independent, making low temperature measurements impractical.

To overcome this difficulty, Miniscalco and Quimby [31] introduced a simplified model that also allows determination of absolute cross sections, with better accuracy than using the FL relation (3.24). This model assumes that the energy levels due to Stark splitting are equidistant. By writing the energies as a function of the constant spacing between individual levels E_{22} for the upper states and E_{12} for the lower ones, the number of the unknown is reduced to 3, which can be evaluated from measured absorption spectra. For ions like Nd^{3+} with an odd number of electrons, the number of levels entering the summation in the partition functions Z_1 and Z_2 is $(2J_1 + 1)/2 = 5$ respectively $(2J_2 + 1)/2 = 2$ for the first lower states $^4I_{9/2}$ and $^4F_{3/2}$. The spacing between two neighboring Stark levels are then determined by measuring the spectral width of the manifolds 1 and 2. The *zero phonon energy* E_0 , between the lowest individual levels of the two manifolds, is the energy calculated at the average wavelength of the absorption and emission peaks. The spectral width of the upper manifold is twice the width measured from the peak to the high energy side point of the spectrum, where the intensity of the absorption spectrum drops to 5% from its maximum. In a similar manner the low energy side of the absorption spectrum, determines the spectral width of the lower Stark manifold. This model has been tested on a number of transitions [31] and the results were overall more accurate than when the Einstein's relation (FL) has been used.

Limitations and potential difficulties

In order to discuss those situations for which the spectral width $|E_{ij} - h\nu|$ is not negligible with respect to $k_B T$, it is convenient to rewrite the relation connecting the actual absorption and emission cross sections (3.56) as

$$\sigma_{21}(\nu) = \sigma_{21}^{McC}(\nu)F(\delta E_{ij}) \quad (3.58)$$

where $\sigma_{21}(\nu)$ represents the actual emission cross section, $\sigma_{21}^{McC}(\nu)$ is the emission cross section determined by the McCumber relation as

$$\sigma_{21}^{McC}(\nu) = \frac{Z_1}{Z_2}\sigma_{12}(\nu)e^{(E_0 - h\nu)/k_B T} \quad (3.59)$$

and $F(\delta E_{ij})$ is a factor depending on the spectral width $\delta E_{ij} = E_{ij} - h\nu$ of the individual Stark level given by

$$F(\delta E_{ij}) = \left[\frac{\sum_{i,j} e^{-\Delta E_{1i}/k_B T} \sigma_{0ji}(\nu_{ij}) g_0(\nu - \nu_{ij}) e^{-(E_{ij} - h\nu)/k_B T}}{\sum_{i,j} e^{-\Delta E_{1i}/k_B T} \sigma_{0ij}(\nu_{ij}) g_0(\nu - \nu_{ij})} \right] \quad (3.60)$$

For $\delta E_{ij} > 0$ and comparable with $k_B T$, the factor $F(\delta E_{ij}) < 1$, implying that for the real emission cross section is smaller than the one calculated using the McCumber formula $\sigma_{21}^{McC}(\nu)$. If $\delta E_{ij} < 0$ the factor $F(\delta E_{ij}) > 1$, which produces a real emission cross section that is larger than the McCumber calculated one. This means that for large spectral widths $|E_{ij} - h\nu|$ of the individual Stark levels, compared to $k_B T$, the McCumber formula overestimates the low energy side of the emission lineshape and underestimates the high energy side, with respect to the peak E_{ij} .

Moreover, different types of broadening will affect differently the calculated spectral shape [47], [48], due to the way the lineshape functions $g_{0L}(\nu - \nu_{ij})$ and $g_{0G}(\nu - \nu_{ij})$ decay to zero from the peak. The Lorentzian function has longer and larger wings compared to the Gaussian function, and when they are multiplied by a growing or decaying exponential, the Lorentzian lineshape produces a larger distortion in the calculated lineshape than the Gaussian. This can be visualized by calculating the McCumber cross

section for a single transition between two nondegenerate individual levels i and j . In this case, the emission and absorption cross sections are equal (2.33). The McCumber theory, however, predicts an emission cross section given by

$$\sigma_{ji}^{McC}(v) = \sigma_{ji}(v)e^{\delta E_{ij}/k_B T} = \sigma_{0ji}(v)g_0(v - v_{ij})e^{\delta E_{ij}/k_B T} \quad (3.61)$$

Fig.(3.4) illustrates the distortion generated by pure homogeneous (a) and pure inhomogeneous broadening (b) on the spectral shape of a single Stark transition. The

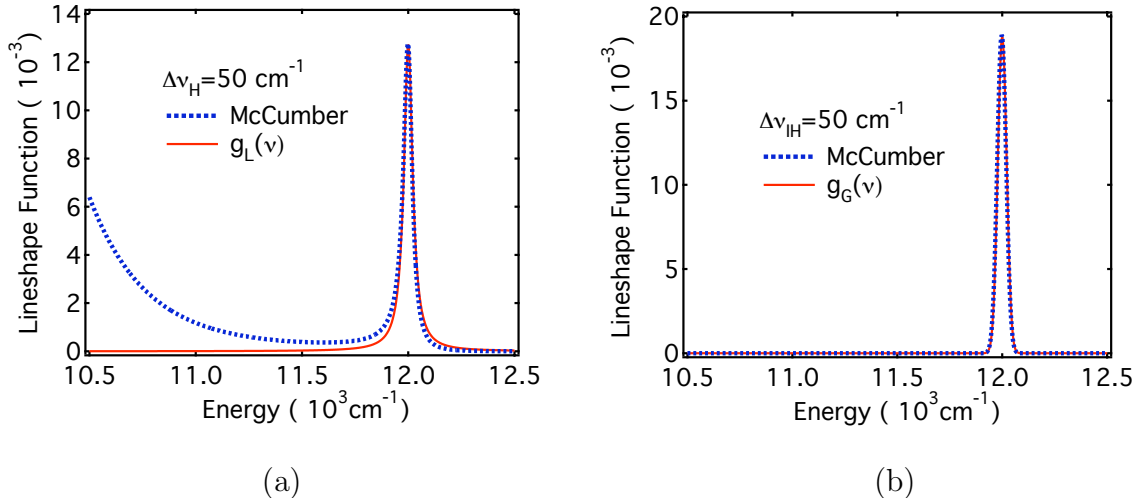


Figure 3.4: Distortion introduced by the McCumber relation on a Lorentzian (a) and a Gaussian (b) lineshape function with a spectral width of 50 cm^{-1} at room temperature.

disagreement between the McCumber lineshape and the real one worsens with increasing the total linewidth. Numerical simulations for multiline spectra have also shown that the degree of distortion increases with the number of transitions between the two multiplets [47].

The relative amount of distortion is expected to be small at room temperature for typical values of the homogeneous and inhomogeneous linewidth of the rare earth transitions in glassy environments. It can, however, become significant at low or high temperature [47]. Inhomogeneous linewidth is temperature independent, and as the

temperature decreases, the factor $k_B T$ becomes smaller, so at some value of T , the linewidth becomes comparable with, or even larger than $k_B T$, and the McCumber theory will eventually break down. Homogeneous linewidth, on the other hand, varies almost quadratically with the temperature, and as the temperature increases, the ratio $h\Delta\nu_H/k_B T$ increases linearly with T . At high enough temperature, the homogeneous width exceeds $k_B T$ and again the McCumber theory will break down.

Real situations involving transitions of rare earth ions especially in glassy hosts are more complex and more general than the cases discussed above. The linewidth of these transitions is determined almost equally by homogeneous and inhomogeneous processes. The lineshape cannot be described by Lorentzian or Gaussian linefunctions, but rather by their convolution, which determines a Voigt profile. For narrow linewidths (homogeneous and inhomogeneous much smaller than $k_B T$), the McCumber relation is still valid [47], and for large widths, distortions following patterns similar to those discussed above are expected. At room temperature, these distortions are expected to be small, while at low or high temperature they can be very significant.

Chapter 4

Experimental method used for room temperature measurements

In this thesis, the validity of the McCumber theory has been tested experimentally in a number of systems, by comparing measured and calculated cross section spectra. Room temperature absorption and fluorescence measurements were performed on oxide and fluoride bulk glass samples doped with Nd, Tm and Er. To maximize the signal to noise ratio, moderately high concentrations (~ 1 wt%) have been used. The McCumber theory has been applied to calculate emission cross section from measured absorption spectra as well as absorption cross section from measured emission spectra. In order to separate eventual discrepancies caused by limitations of the McCumber theory, careful measurements have been performed so that both absorption and fluorescence data have been taken in the same experimental conditions (same equipment, same instrumental setting, same geometry for light detection, etc.). Special attention was given to certain aspects of the experimental procedure that give systematic errors in the analysis (baseline subtraction for absorption, fluorescence reabsorption in high concentration samples, etc.).

4.1 Emission cross section measurements

The emission cross section can be determined from fluorescence measurements by using the exact FL relation (3.22), which was also recovered by McCumber as Eq.(3.48) and can be written as

$$\sigma_{em}(\lambda) = \frac{\lambda^4}{cn^2} R(\lambda) \quad (4.1)$$

where $R(\lambda)d\Omega$ represents the average fluorescence intensity in photons per unit wavelength interval per unit time emitted into the solid angle $d\Omega$.

Optical instruments (spectrometers and photodetectors) measure optical power per unit wavelength interval. The measured signal $S^{meas}(\lambda)$ represents the number of photons $R^{meas}(\lambda)$ measured by the instrument multiplied by the photon energy hc/λ such that

$$S^{meas}(\lambda) = R^{meas}(\lambda) \frac{hc}{\lambda} \quad (4.2)$$

The spectrometer and the photodetector introduce their own response $A(\lambda)$ to a measured signal, depending on the sensitivity of the photodetector and the spectral efficiency of the spectrometer. Therefore, the measured signal must be calibrated by comparing the measured fluorescence signal with a blackbody spectrum $S_{BB}(\lambda)$ taken in identical conditions. We can write

$$S^{meas}(\lambda) = A(\lambda) I^{cal}(\lambda) \quad (4.3)$$

$$S_{BB}^{meas}(\lambda) = A(\lambda) I_{BB}^{cal}(\lambda) \quad (4.4)$$

where $I^{cal}(\lambda)$ and $I_{BB}^{cal}(\lambda)$ represent the calibrated (true) intensities (power per unit area) of the fluorescence and blackbody radiation respectively detected by the instrument. The calibrated fluorescence intensity can be written as

$$I^{cal}(\lambda) = c\rho_\lambda^{BB}(\lambda) \frac{S^{meas}(\lambda)}{S_{BB}^{meas}(\lambda)} \quad (4.5)$$

where $\rho_{\lambda}^{BB}(\lambda) = I_{BB}^{cal}(\lambda)/c$ is the spectral density of the blackbody radiation, given by the Plank's formula (2.6). As a function of wavelength, the spectral density is given by

$$\rho_{\lambda}^{BB}(\lambda) = \frac{8\pi hc}{\lambda^5} \frac{1}{e^{(hc/\lambda)/k_B T_c} - 1} \quad (4.6)$$

where T_c is the color temperature of the blackbody source. From Eqs.(4.2) and (4.5) the fluorescence intensity collected by the instrument is

$$R^{meas}(\lambda) = \frac{\lambda}{hc} c \rho_{\lambda}^{BB}(\lambda) \frac{S^{meas}(\lambda)}{S_{BB}^{meas}(\lambda)} A_{PD} \quad (4.7)$$

where A_{PD} is the area of the beam on the photodetector. Absolute values of the emission cross section cannot be determined from basic fluorescence measurements, since only a fraction of the spontaneously emitted photons is collected in the direction of the spectrometer-photodetector system, also the signal measured by the photodetectors is only proportional to the photon flux. The spectral shape of the emission cross section $\sigma_{em}^{ss}(\lambda)$ is determined by the following parameters that depend on wavelength

$$\sigma_{em}^{ss}(\lambda) = \frac{\lambda^5}{n^2(\lambda)} \rho_{\lambda}^{BB}(\lambda) \frac{S^{meas}(\lambda)}{S_{BB}^{meas}(\lambda)} \quad (4.8)$$

which is the same as the FL relation derived by Aull [33], except for the factors that are constant with the wavelength.

To determine the spectral shape of the emission cross section we need to measure the fluorescence and the blackbody spectra under identical conditions, to estimate the color temperature of the blackbody source, and to account for the spectral change in the refractive index across the spectral width of the emission transition.

4.2 Absorption cross section measurements

The absorption cross section can be determined from absorption measurements by comparing the transmission spectra with sample in and out the beam path. The light

traversing an optical medium of length L is absorbed according to Beer's Law as

$$I(\lambda) = I_0(\lambda)\eta(\lambda)e^{-\alpha(\lambda)L} \quad (4.9)$$

where $I(\lambda)$ and $I_0(\lambda)$ is the light intensity with the sample in and out the beam, $\alpha(\lambda)$ is the absorption coefficient, and $\eta(\lambda)$ represents the fraction of light lost by processes like reflection on the two faces of the sample, scattering inside the sample, coupling loses on the slit of the spectrometer, etc. The absorption coefficient can be written as

$$\alpha(\lambda) = \frac{1}{L} \ln \left[\frac{I_0(\lambda)}{I(\lambda)} \right] + \frac{1}{L} \ln [\eta(\lambda)] \quad (4.10)$$

The absorption cross section has been defined in section (2.2) by Eq.(2.31) as

$$\sigma_{abs}(\lambda) = \alpha(\lambda)/N \quad (4.11)$$

where the population of the lower energy level N_1 has been taken equal to the total ion concentration N of the sample¹. We can then write the absorption cross section as

$$\sigma_{abs}(\lambda) = \sigma_{abs}^{meas}(\lambda) - f(\lambda) \quad (4.12)$$

where $\sigma_{abs}^{meas}(\lambda) = (1/NL) \ln [I_0(\lambda)/I(\lambda)]$ is the value of the absorption cross section determined experimentally by measuring $I_0(\lambda)$ and $I(\lambda)$ for known ion concentrations and sample length, and $f(\lambda) = -(1/NL) \ln [\eta(\lambda)]$ is a slowly varying function of wavelength. This represents the baseline of the measured cross section and needs to be estimated by performing a curve fit of the base points, in order to obtain the real value of the absorption cross section.

4.3 Experimental setup

Since the consistency and reproducibility of the measurements are very important in the proper study of the validity of the McCumber theory relating the emission and the

¹This is true for low power excitations, which is the case of sample radiation with custom halogen or laser diode sources.

absorption spectra, the fluorescence and absorption measurements were performed using the same equipment, same geometry and same instrumental settings. However, different optical transitions require instrumentation, settings and setup arrangements specific to a particular wavelength range (detectors sensitive to the emission wavelength, appropriate amplification of weak transitions, space limitation in situations when light needed to be refocused on small size detectors by inserting additional lenses, etc.). To account for all the different requirements, the experimental setup was slightly modified between the investigations of the different optical transitions, but all measurements needed in relating absorption and emission spectra have been taken in exactly same conditions (or careful analysis has been done to check the effect of parameters that were not needed to be kept the same, like the chopping frequency, for example).

4.3.1 Experimental setup for fluorescence measurements

The basic experimental setup used in fluorescence measurements is shown in Fig.(4.1). The samples were pumped at either 784 nm with a 70 mW Sanyo diode laser DL7140-201S operated at 100 mA, or at 808 nm with a Thorlabs 200 mW diode laser L808P200 operated at 250 mA by a diode laser controller LDC220, which can control the bias range from 0 to ± 2 A. The operational range has been selected close to the typical values provided in the company specification sheets. Diode lasers generate strongly divergent, asymmetrical light beam, and lenses are required to collimate the beam in order to transport it across large distances. The beam divergence is described by θ_{\parallel} and θ_{\perp} , which represent the angles in a plane parallel to the pn junction of the diode, or in a plane perpendicular to the junction. Typical divergence angle for the two lasers are $\theta_{\parallel} = 7^{\circ}$ and $\theta_{\perp} = 17^{\circ}$ for the 794 nm laser and $\theta_{\parallel} = 10^{\circ}$ and $\theta_{\perp} = 30^{\circ}$ for the 808 nm laser. Placing the lasers at the focal point of a lens (lens 3) with a 2.5 cm focal length and ~ 2.4 cm diameter ensures that most fraction of the beam is collected by the lens. It

is also important that the beam is not too much expanded, so it can farther be focused to a tight spot on the sample. A second lens (Lens 4) with a 5.5 cm focal length² focuses the beam on the sample and a mirror changes the direction of propagation to a vertical propagation. This is a very convenient geometry, since the focused beam on the sample

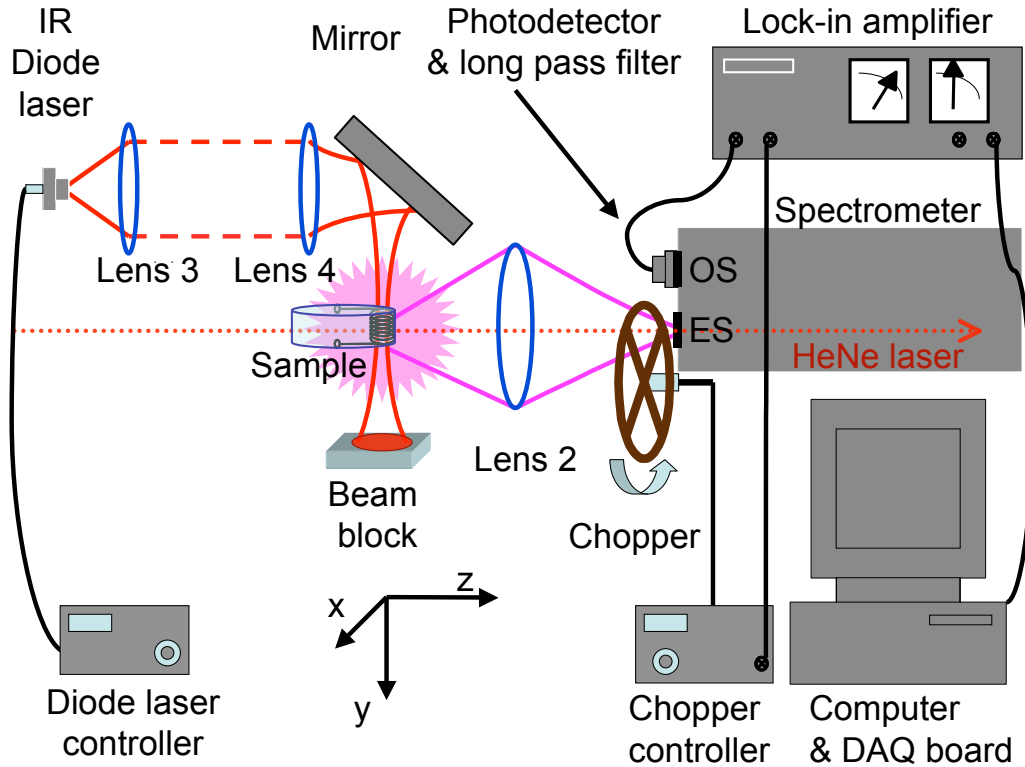


Figure 4.1: Experimental setup for emission measurements

determines a fluorescence object (of a height equal to the width of the sample and width equal to the diameter d_x of the beam in the x direction) that has the same orientation as the entrance slit ES of the monochromator, which improves the coupling efficiency of the fluorescence onto the entrance slit.

²These are examples of settings that were used at some instance for a particular setup. The lenses have been changed as the experiment has been fine-tuned.

The fluorescence is collected in a direction perpendicular to the direction of the laser beam with another lens (Lens 2) and focused on the ES of the monochrometer. The focal length-diameter combination is determined by the acceptance angle of the monochrometer ($f/D = 8.6$), also chosen to provide best collection of the fluorescence, which is emitted in all directions. Lens 2 is placed on a translation stage that allows adjustment of the focus point onto the ES in both z and x directions. The y position is optimized by modifying the height of the post supporting the lens. As reference for aligning the optical axis of the collection system with the optical axis of the monochrometer, a HeNe laser has been used.

The fluorescence is then passed through a 0.5 m Jarrell-Ash 82-020 spectrometer, with a 590 *grooves/mm* diffraction grating, blazed at $1.6\mu\text{m}$. The linear dispersion of the spectrometer at the output slit OS is 3.2 nm/mm . The two slits of the monochrometer were set to a spectral resolution of 1.5 nm, corresponding to slit widths $\text{ES} = \text{OS} = 0.45 \text{ mm}$. Several slit width combinations were tested in order to determine the entrance-output slit widths that permit us to resolve the individual Stark structure of the transition, yet give the best signal to noise ratio³. As shown in Fig.(4.2), narrowing the slits beyond 0.5 mm does not improve the spectral resolution, due to the inhomogeneous broadening of the spectral line. At 0.6 mm width, the peak starts only slightly to become shorter, while at 2mm width (ES or OS), this becomes noticeably shorter and broader. If the following set of slit widths (0.45 mm, 0.60 mm and 2.00 mm) is translated in spectral resolutions, it corresponds to (1.44 nm, 1.92 nm and 4.80 nm), which in terms of energy widths about the 880 nm fluorescence transition becomes (19 cm^{-1} , 25 cm^{-1} and 62 cm^{-1}). Typical inhomogeneous widths of rare earth transitions in silicate and fluoride glass are in the range $30\text{-}80 \text{ cm}^{-1}$ [20], suggesting that the slit combination $\text{ES} = \text{OS} = 0.45 \text{ mm}$ is a good choice for measuring most spectral transitions studied

³By closing the slits too much the signal is reduced accordingly.

further in this work⁴. This combination has been used to acquire all spectra needed in the McCumber analysis, for all spectral transitions. If large OS and ES are used, the

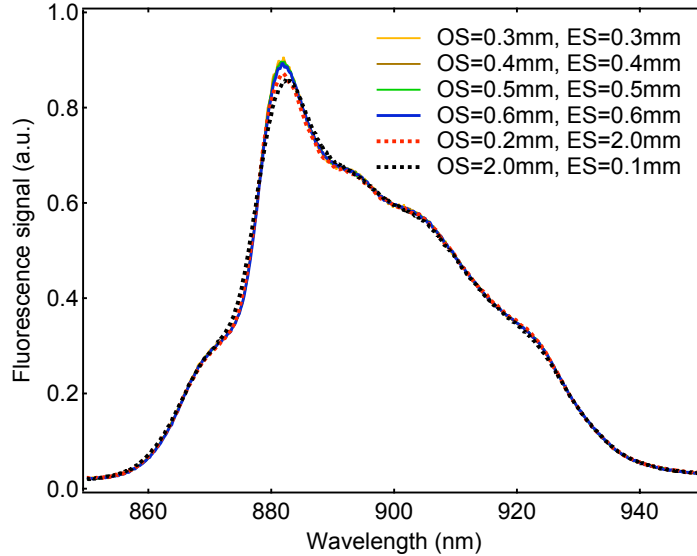


Figure 4.2: Effect of different combinations of the entrance and output slit widths of the monochromator on the measured lineshape

spectral broadening becomes comparable with the slit width and the measured signal is a convolution between the shape of the slit and the shape of the line. This results in shorter and broader peaks, with a trapezoidal or even triangular shape (depending on the ratio of the two widths). Unequal slit widths create slight asymmetrical deformation of the spectra, due to any inclination of the optical axis of the experimental setup with respect to the optical axis of the monochrometer.

The light that exits the monochrometer is measured with either a silicon photodetector (for $\lambda < 1100$ nm) or a germanium photodetector cooled at -79°C (for $1100 < \lambda < 1800$ nm). Long pass filters with cutoff wavelength at 550 nm for $\lambda < 1100$ nm and at 950 nm for $1100 < \lambda < 1800$ nm have been used to reject the second order spectra. A lock-in amplifier is used to improve the signal to noise ratio, and then the

⁴This combination should allow us to resolve peaks of spectral width $\sim 20 \text{ cm}^{-1}$.

spectra are recorded by a data acquisition board DAQ and save to computer files for processing. The reference signal used by the lock-in was produced by cutting the beam with a chopping wheel, rotating at a fixed frequency. The frequency can be adjusted from a chopper controller, and has been selected to be as low possible to reconstruct a large fraction of the signal within the chopping time. Still the frequency cannot be set too low, to avoid instabilities determined by non perfect rectangular pulses (produced by the finite slicing time t_{ch} of a large diameter beam) or other irregularities in the flatness of the wheel. Typical chopping frequencies used in these experiments were in the range of 15-75 Hz.

For the measurements below 1100 nm, the silicon photodetector SiPD can be directly attached to the OS, with the long pass filter placed in front of it. This way the exposure of the photodetector to the stray room lights is drastically limited. The active area of the photodetector is 1 cm^2 , and this ensures a better collection of light from larger image sizes. However, this introduces a larger time constant $\tau_c = R_L C$, where R_L is the load resistance across which the voltage produced by the photoelectron current is collected, and C is the capacitance of the detector. A larger area photodetector will give a slower response of the detector. This, combined with the time constant of the lock-in, will determine the response time t_c of the acquisition system. In this situation the scan speed v_s and the chopping frequency f_{ch} have to be adjusted accordingly. A number of combinations (t_c, v_s) have been tried, and for a particular experiment we selected those ones that give the fastest scan for which spectra are not distorted by recording the data at a rate much higher than the response time. If the acquisition time is too short (scan speed too high), the spectra will be shifted in wavelength with respect to each other, due to the fact that the data are not recorded in real time, but before the measured signal has reached the actual value. If the scan speed is too low, the acquisition time required to take a spectrum becomes very large, increasing the chance of unwanted events

like fluctuations in electrical power, temperature fluctuations or decay in the luminous output of the incandescent lamps, etc., to perturb the data.

The germanium photodetector GePD used for measurements in the spectral range $1100 < \lambda < 1800$ nm has been cooled at $-79^\circ C$ with dry ice (condensed CO_2). The active area of this photodetector is $1\ mm^2$, much smaller (100 times) than the one of SiPD. This implies some changes in the experimental set-up, settings and alignment compared to the measurements with the silicon photodetector. The effect of the time response introduced by this detector is not as critical as for SiPD, but rather the time constant lock-in becomes more important. Due to the very small active area and the large physical dimensions of the GePD, the light that exits the OS needed to be focused on the detector with a short focal length (2.5 cm) lens (Lens 5), placed on a 3-d translation stage. Also, another mirror was used in the path of the collimated beam at 45° with the horizontal axis of it, to redirect the beam in horizontal plane so more space can be created for the detector. The long pass filter was placed right in front of the detector, very close to its surface. The increased sensitivity of this photodetector (when cooled), requires extreme grounding care also critical isolation from the room lights. The entire detection system (OS, Lens 5, filter, GePD) has been surrounded by a dark chamber made by thick velvet cloth. Also, an iris diaphragm has been placed in front of the chopping wheel, to limit the stray light that reaches the monochromator through the wheel (the only light that gets amplified by the lock-in).

The position and the geometry of the IR laser beam with respect to the sample and the entrance slit of the monochromator are very important, as well as a small diameter of this at the focus. To maximize the collection efficiency and reduce reflection losses on the faces of the sample, the beam should be positioned perpendicular to the surface of the sample, and parallel to the ES. The position of the beam on the sample can be modified in the x,z plane by twisting the two screws of the plane mirror. It is also important to

illuminate the sample at the very edge, in order to reduce fluorescence reabsorption inside the sample. For this, the sample has been placed on a translation stage which allows changing the location of the focus point on the sample without changing the geometry of the collecting system (Lens 2, monochromator, photodetector). Also, focusing the laser beam very tightly to a small diameter, assures a higher intensity though a more

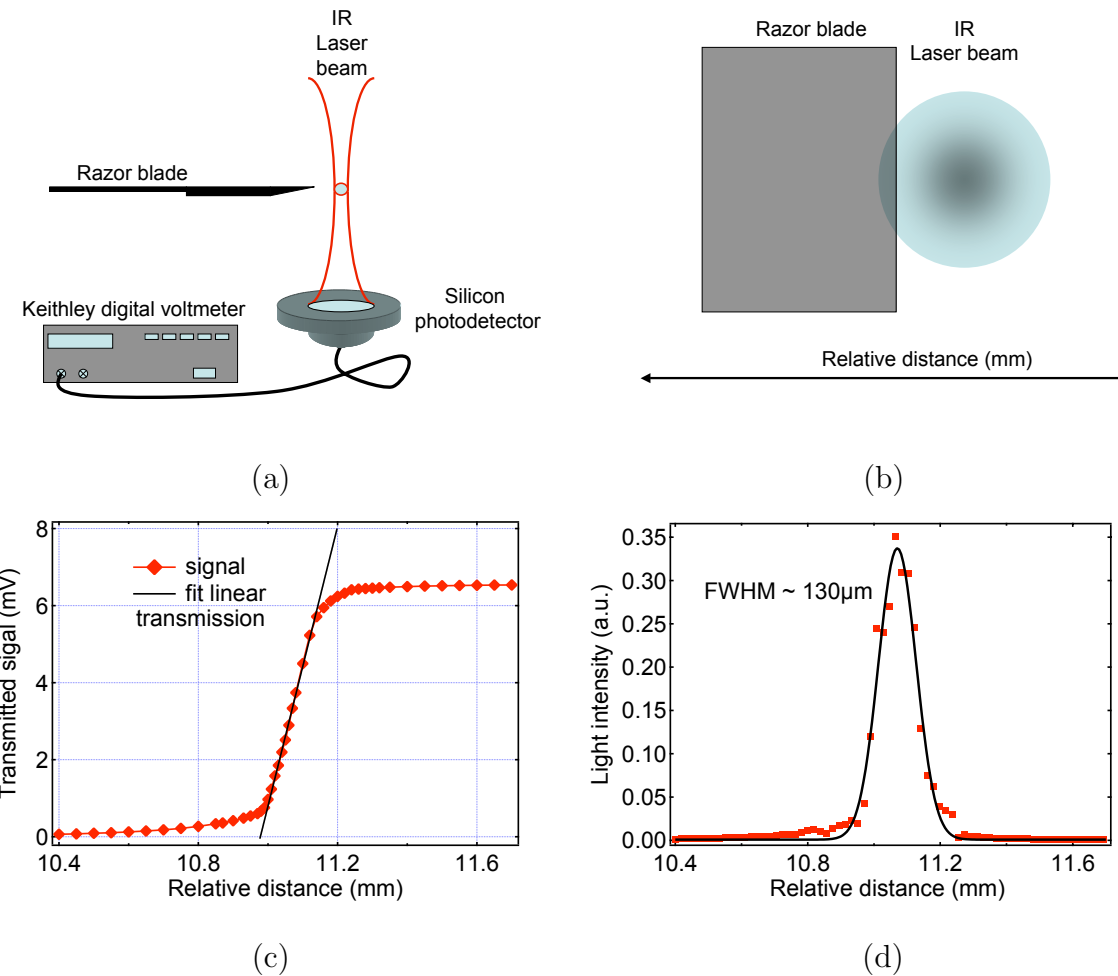


Figure 4.3: Determination of the beam diameter by cutting the beam with a razor blade: a) front view; b) cross section view; c) transmitted signal function of distance; d) the first derivative of the transmitted signal fitted with a gaussian function

efficient excitation of the sample ions, generating a larger fluorescence signal. However, if the beam is too tight, the diameter of it will vary significantly along the width of

the sample, creating problems of the type discussed above. Choosing the right focal length lens to focus the beam on the sample is a compromise between high and uniform intensity across sample. A wide beam diameter in the z direction will create problems regarding fluorescence reabsorption, whereas a nonuniform beam in the same direction will generate strong scattered light that will reduce the intensity of the beam inside the sample, also when collected by Lens 2 will affect the measured spectra if the scattered light is in the same wavelength range as the fluorescence. The diameter of the laser beam from the 784 nm laser has been measured by cutting the beam with a razor blade and measuring the transmitted light as a function of the distance (along z) with a Keithley digital voltmeter as shown in Fig(4.3). A measure of the beam diameter is the FWHM of the gaussian fit of the first derivative of the transmitted signal with the distance (d). The FWHM was $\sim 130\mu m$ for the 794 nm laser in the z direction (the direction of the fluorescence collection).

As explained in section (4.1) the measured fluorescence signal must be calibrated for the detection system response, which in general varies across the spectra. This is done by comparing the fluorescence spectra with the spectrum of blackbody source taken in identical conditions. The lamp used to calibrate the spectra was a 20W Gilway L7394 tungsten-halogen lamp with a nominal color temperature of 3000 K, and a 2.9 mm length and 1 mm diameter filament. The filament was placed exactly at the location of the focused beam on the sample, and the intersection of the reference HeNe laser beam with the IR beam. A third HeNe laser has been used in the (x,z) plane as a backup, for situations when the bulb was distorting the direction of propagation of the reference laser. The position of the filament with respect to ES turned out to be very critical in measuring the correct fluorescence signal and good care has been taken to reconstruct the exactly same conditions as used in measuring the fluorescence. The experimental setup has been kept exactly the same, and no adjustments have been done regarding

the optical alignment of the collecting system. The blackbody spectrum depends on

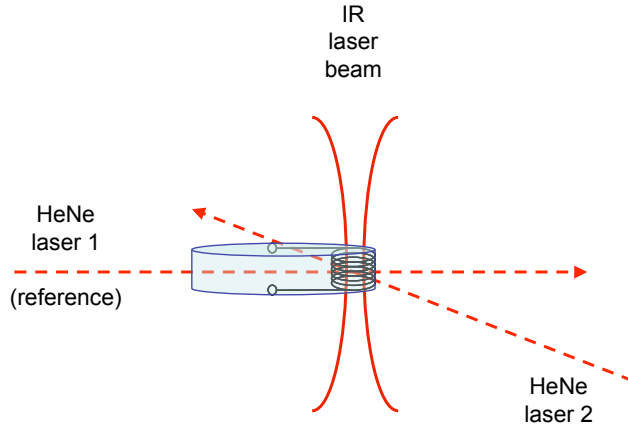


Figure 4.4: Alignment of the filament at the intersection of the three laser beams

the color temperature T_c , which varies with the operation voltage. To select the correct color temperature, the theoretical blackbody curves of the spectral density have been compared with the data sheet values determined from the company specification sheets, to get a feeling about the correct calibration of the lamps. As shown in Fig.(4.5) the data sheet values lineup very well on the theoretical curves, which implies that a good calibration of the lamps has been performed by the company. The voltage applied on the lamp was within the 85% – 95% of the operating voltage prescribed in the spec-sheets. This determines a range for the color temperature of 95% – 98% (fig.1 p.3 spec.sheet) of the nominal value (or 2850 - 2940 K). The temperature used for the blackbody has been taken as 2900 K in all experiments. The color temperature is more critical for the wavelength from ~ 800 nm to ~ 1200 nm, where the curve changes concavity. For $\lambda < 800$ nm and $1200 < \lambda < 1800$ nm the curves differ only by a constant scale factor, resulting in the same overall contribution to the spectra.

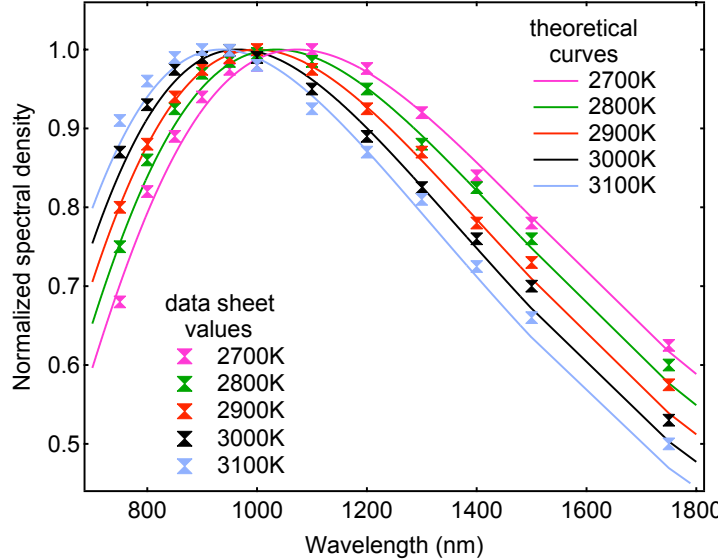


Figure 4.5: Calibration of the color temperature of the filament

Another factor that can introduce a spectral distortion of the measured emission spectra is the dispersion of the light inside the sample, if this is not properly accounted for. The variation of the refractive index with the wavelength can be modeled by the Cauchy relation

$$n(\lambda) = A + \frac{B}{\lambda^2} \quad (4.13)$$

where A and B are constants and λ is expressed in nm. The two constants A and B are usually determined from known values of the refractive index corresponding to two different wavelengths. For silicate glass samples, the refractive index at the wavelength 1062 nm is 1.62338 and at the sodium D line $\lambda_D = 589$ nm is $n_D = 1.6363$ as found in the spec-sheets for the Nd:silicate sample LL1041. This will give a spectral variation for the refractive index in silicate samples according to

$$n_{silicate}(\lambda) = 1.61768 + \frac{6423.32}{\lambda^2} \quad (4.14)$$

In fluoride glasses, the A and B constants have been determined from Abbe's number $\nu_D = (n_D - 1)/(n_F - n_C)$, where n_F and n_C are the refractive indices for the hydrogen

F and C lines at $\lambda_F = 486.13$ nm and $\lambda_C = 656.27$ nm. The Abbe's number for fluorozirconate glass is $\nu_D = 64$ (from ref. [71]), which should be a representative value for most fluoride glasses. The refractive index for fluoride glasses is then given by

$$n_{\text{fluoride}}(\lambda) = 1.469 + \frac{3927.41}{\lambda^2} \quad (4.15)$$

These expressions (4.14 and 4.15) have been used in the present study for determining the measured emission cross section from fluorescence spectra. However, across the wavelength interval spanned by the transitions studied, the refractive index only affects the measured emission cross section by $\sim 0.3\%$ in fluoride glasses for the 780 – 950 nm span range (which is the largest used in our measurements) and by $\sim 0.4\%$ for the same range for silicate samples, and can be simply omitted from the analysis by assuming constant refractive index across the spectral rage of study.

4.3.2 Experimental setup for absorption measurements

For absorption measurements the same tungsten-halogen lamp has been used as in fluorescence measurements, with the filament of the lamp imaged onto the sample as shown in Fig(4.6). The same way as for the blackbody correction, the image of the filament was very carefully aligned to coincide with the location of the focused pump beam that was used in fluorescence measurements. The same two HeNe lasers and the IR pump beam have been used in determining the exact location of the filament image on the sample. This ensures that the geometry for light collection and measurement is identical in both fluorescence and absorption measurements. The transmission spectra have been measured with the sample in and out of the beam. The same equipment, same instrumental setting (same width of the entrance and exit slits of the monochromator), same settings for collection system (collective lenses and position of the detectors) as for fluorescence measurements have been used.

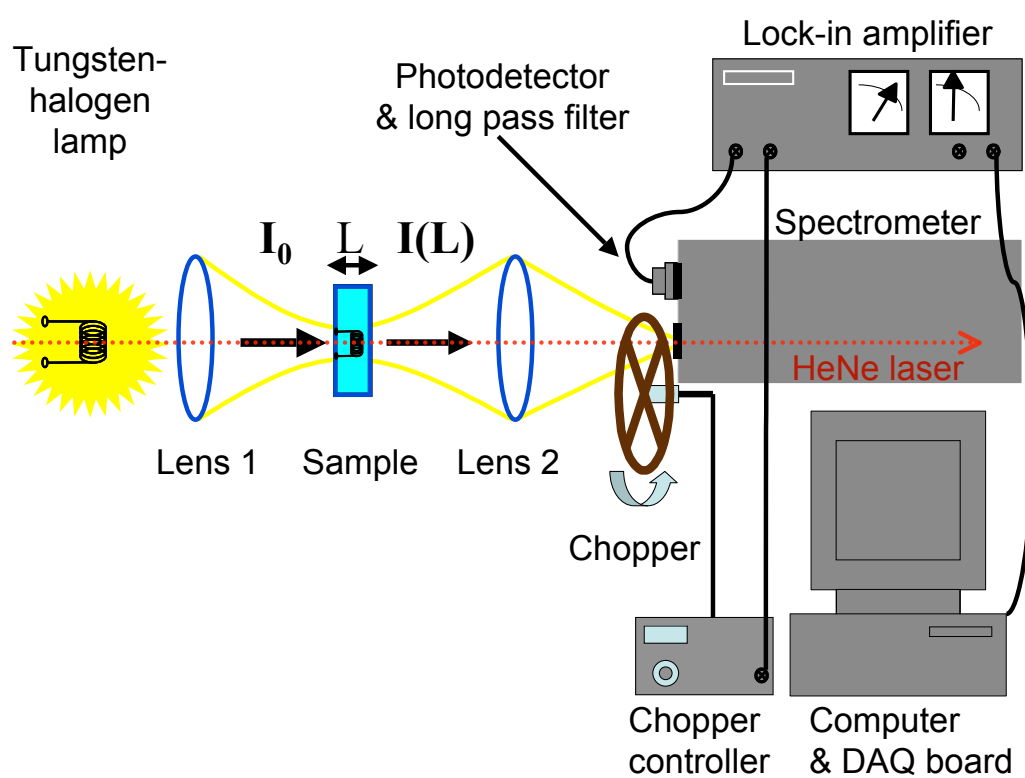


Figure 4.6: Experimental setup for absorption measurements

Chapter 5

Experimental investigations of the validity of the McCumber theory at room temperature

Absorption and fluorescence measurements have been performed at room temperature on seven rare earth doped glass samples: Nd:silicate, Nd:fluorozirconate, Tm:fluorozirconate, Tm:silicate, Tm:fluorophosphate, Er:silicate and Er:fluorozirconate. The transitions studied are the ground state absorption and emisission indicated by double arrows in Fig.(5.1) for Nd^{3+} , Fig.(5.12) for Tm^{3+} , and Fig.(5.25) for Er^{3+} . Pump transitions for fluorescence measurements are indicated by the dashed arrows in the same figures. The spectra calculated using the McCumber relation Eq.(3.39) were then compared to the measured spectra. Since the fluorescence measurements give only the relative shape of the cross section spectra and not absolute values, an appropriate scale factor has been chosen in each case which gave the best overall agreement between the measured and calculated spectra.

Different factors that affect the absorption and emission shape were expanded in

detail and the effect of each to the calculated cross spectra were carefully investigated. The effect of baseline subtraction for absorption spectra, spectral reabsorption of the fluorescence and filament alignment for the blackbody correction was studied for each sample. Factors like refractive index or color temperature that were constant during the different experiments, but could in principle introduce spectral variations across the transition were also investigated. The study explained in section (4.3.1) shows that the color temperature of the filament used to correct the fluorescence spectra presents very slight variations ($\pm 50\text{K}$) around the value of 2900K used in all experiments, for the range of operating voltage applied. This affects the calculated absorption cross section by $\sim \pm 0.8\%$ at the 808 nm absorption peak, for spectra normalized to the same value at 880 nm emission peak. The variation of the refractive index with the wavelength has been taken into account by using the Cauchy's expressions (4.14 and 4.15) in determining the measured emission cross section from fluorescence spectra. However, across the wavelength interval spanned by the transitions studied, the refractive index only affects the measured emission cross section by less than 0.5% and can be therefore omitted from the analysis.

5.1 Nd^{3+} doped samples

The Nd:silicate and Nd:fluorozirconate samples were pumped at 784 nm to excite the combined level ($^2H_{9/2}, ^4F_{3/2}$) as shown by the dashed arrows in Fig.(5.1)). Since the energy gap between the ($^2H_{9/2}, ^4F_{5/2}$) and $^4F_{3/2}$ manifolds is only about 1000 cm^{-1} , there is a small but measurable thermal population of the ($^2H_{9/2}, ^4F_{5/2}$) levels at room temp ($\approx 200\text{ cm}^{-1}$), according to the Boltzmann factor $\exp(-1000/200) = 0.0067$. Therefore, fluorescence can be observed from both the ($^2H_{9/2}, ^4F_{5/2}$) and $^4F_{3/2}$ levels, even though the nonradiative decay rate out of the ($^2H_{9/2}, ^4F_{5/2}$) level is much greater than the radia-

tive rate. There are upward-going as well as downward-going nonradiative transitions,

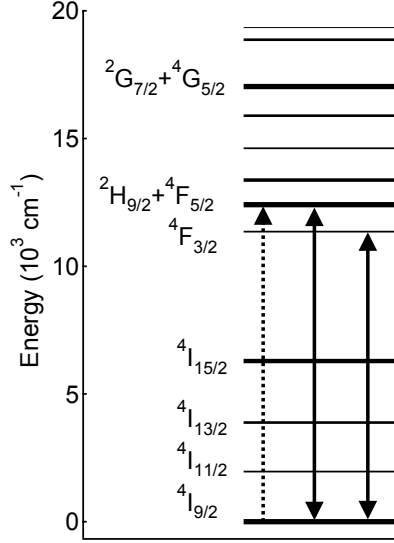


Figure 5.1: Energy level diagram for the lower-lying levels of Nd^{3+} .

so the levels achieve a thermal distribution.

Since the combined ($^2H_{9/2}, ^4F_{5/2}$) and $^4F_{3/2}$ levels act in effect as a single multiplet with widely spaced energy levels, we applied Eq.(3.39) separately to the measured absorption and emission spectra over the entire range 750-1000 nm, which includes both the ($^2H_{9/2}, ^4F_{5/2}$) and $^4F_{3/2}$ levels.

5.1.1 Nd:silicate glass

The Nd:silicate sample investigated is a LG06 glass, doped with 0.9 % moles of Nd^{3+} ions. The ion concentration is $N = 2.65 \times 10^{20} \text{ ions/cm}^3$ and the thickness of the sample is 0.5 cm. Absorption and fluorescence measurements have been performed and specific difficulties of each type of measurements will be treated separately as follows.

A. Absorption Measurements

To determine the absorption cross section according to Eq.(4.12), we recorded transmission spectra from a halogen-filament source, with the sample in and out of the beam. To ensure that the geometry for light collection and measurement is the same in both absorption and fluorescence measurements, the image of the filament has been carefully aligned to coincide with the location of the focussed beam used in fluorescence measurements.

Three different situations have been considered regarding the sample position with respect to the light beam: Q - sample at the exact focus point and perpendicular to the direction of the beam, M - sample slightly tilted with respect to the beam, and P- sample tilted and out of focus. These situations are illustrated in Fig.(5.2 (a)) and the results are shown in the (b)-(d) graphs. As we see from these graphs, the position and orientation of the sample affects the baseline of the uncorrected absorption spectra, but not the corrected cross section, within the limiting errors of a good baseline subtraction.

The subtraction of the baseline, however, turns out to be very important when the measured absorption cross section is used in the McCumber analysis to calculate emission cross section spectra. The baseline is determined by a combination between the geometry of the sample and its orientation with respect to the beam, the path of the light inside the monochromator and the spectral response of the photodetector. It varies from spectrum to spectrum, and must be individually subtracted for each situation. Choosing the proper fit for the baseline represents by far the factor that most influences the calculated emission spectra. Very small variations in the fitting line can create large deviations at the long wavelength side of the calculated emission spectra, due to exponential amplification of the McCumber equation (3.39). Fig.(5.3 (a)) shows an uncorrected absorption spectrum and three different curves that fit the baseline. At

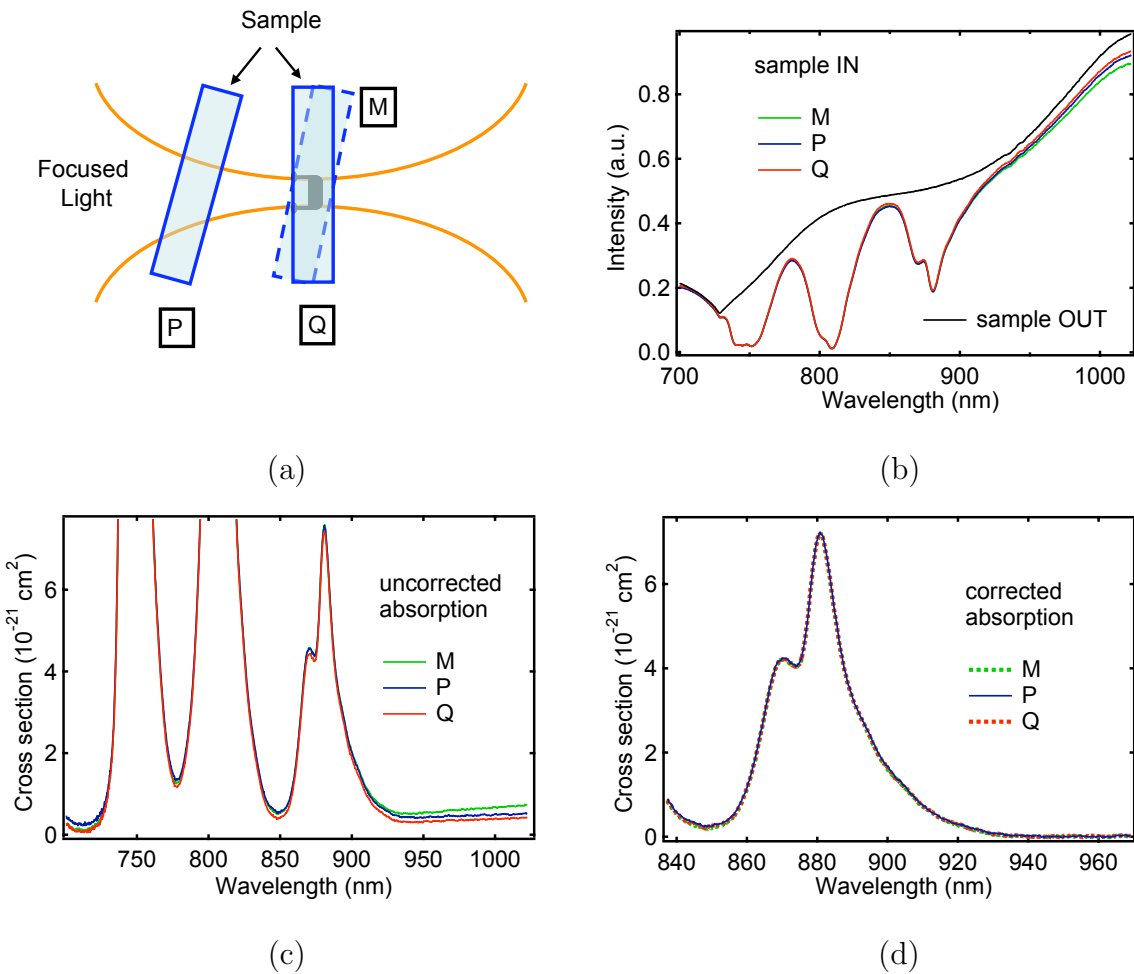


Figure 5.2: Determination of the absorption cross section for three different locations of the sample along the path of the light (a), spectra with sample IN and OUT of the beam (b), uncorrected absorption cross section for the situation M, P and Q (c), and absorption cross section after the baseline subtraction (d).

the scale of the spectral line, they all seem reasonably good fits. When the scale is expanded, however, (as seen in the inset), the three curves give slightly different values of the cross section around 850 nm. Fig.(5.3 (b)) shows how the choice of fit affects the final calculated emission spectrum. The greatest effect is seen on the long-wavelength

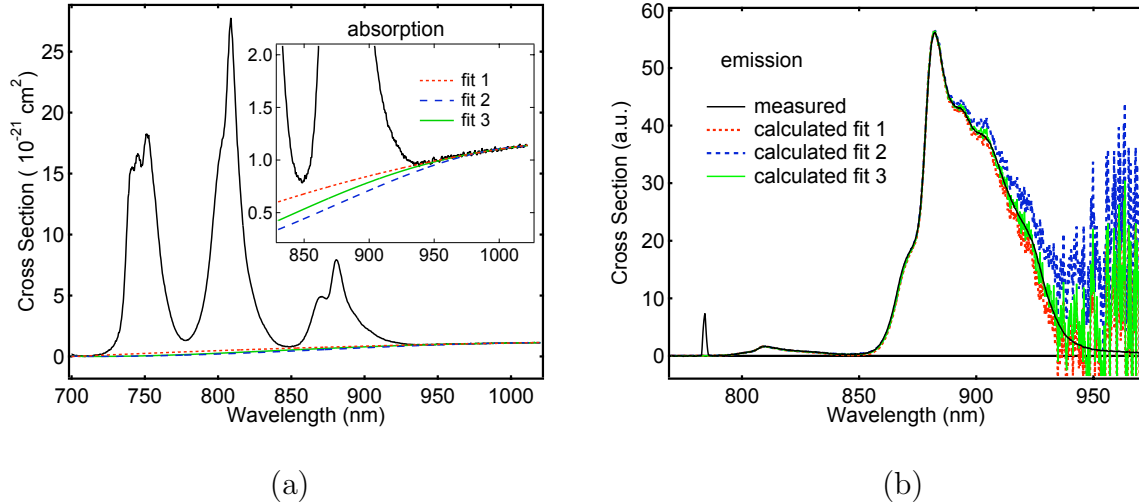


Figure 5.3: Effect of baseline subtraction on the calculated emission spectrum

side, where the shape of the absorption wing is strongly influenced by the choice of baseline fit. In situations where there are overlapping spectral lines, it is even harder to do a perfect fit across a wide spectral interval, because there are more fitting possibilities. Choosing a proper baseline is also difficult when there are not enough data points to do a proper fit, for example at the limits of sensitivity of the photodetector or close to the limits of the spectrometer. If the baseline is obtained by fitting points too far from the spectral line, as in fit #2 in Fig.(5.3 (a) and (b)), the calculated emission has too large a tail. On the other hand, if fitting points are chosen too close to the spectral line, so that part of the spectral wing is being fit to the baseline, then the calculated emission curve cuts off too sharply to zero.

These errors due to the choice of baseline only occur on the long-wavelength side of the emission spectrum. On the short-wavelength side, the absorption is large, and

small uncertainties in the baseline do not have any practical effect.

To overcome this problem, "careful" baseline subtraction has been performed for a decent number of absorption spectra. The baseline for each spectra has been fit with several reasonably good fit curves (low order polynomials), and the best fit has been selected to correspond to their average. The final absorption spectrum used in the McCumber analysis is the average of all the absorption cross sections obtained with the best fit. Also averaging over a number of different spectra increases the signal to noise ratio, and also builds the confidence of managing reproducible and consistent data.

B. Fluorescence measurements

The emission cross section spectra have been determined from fluorescence measurements according to relation (4.8). The fluorescence signal and the blackbody have been taken in identical conditions as described in section (4.3.1). The measured fluorescence signal can be distorted by fluorescence reabsorption in samples with high ion concentrations. Also, improper positioning of the filament for the blackbody correction can determine incorrect emission cross section spectra, though becoming a source of error in relating the measured and calculated cross sections based on the McCumber theory. These two aspects will be treated next in this section.

Fluorescence reabsorption

If the pump laser beam is focused on the sample to a spot that is far from the sample edge, the fluorescence emitted is reabsorbed by other ions in the path toward the collection system. This situation is illustrated in Fig.(5.4 (a)). To minimize the reabsorption, the beam is brought closer to the edge of the sample, in order to reduced the traveling path of the emitted light inside the sample. However, when the wings of beam hit the sample right on its edge as in Fig.(5.4 (b)), if not perfectly smooth edges, the

laser light is scattered outside the sample and also inside it, becoming trapped and producing fluorescence within a much greater volume than the focused beam. The

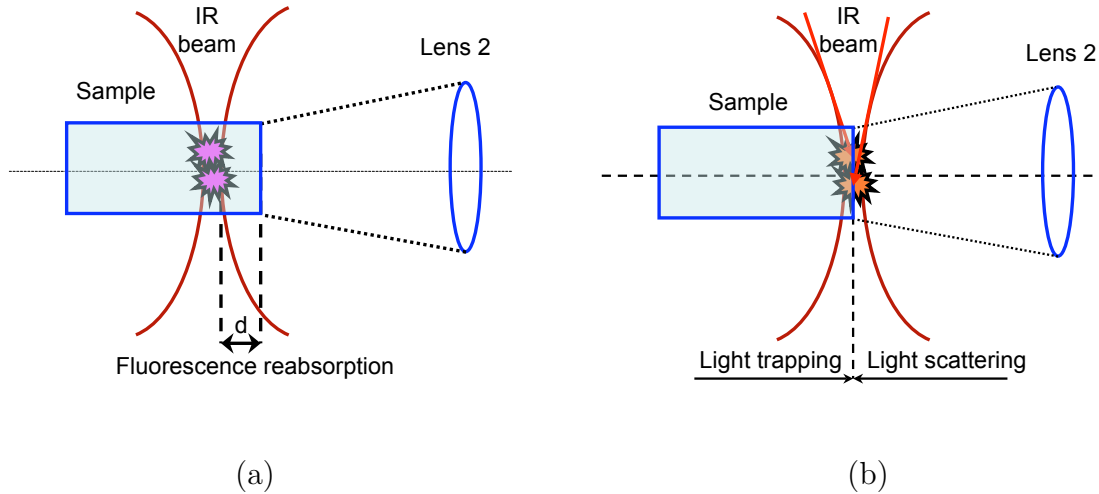


Figure 5.4: Reabsorption of light when the laser beam is focused far from the sample edge (a). Scattering of light inside (trapping) and outside the sample (b).

fraction propagating toward the collection system again becomes reabsorbed along the distance to the edge of the sample. To investigate the reabsorption effect on the measured fluorescence signal, the location of the beam spot on the sample has been varied in very small increments with respect to the edge and the results are shown in Fig.(5.5). If the sample is shined right at its edge, the spectral shape of the fluorescence signal is strongly distorted due to light trapping that causes reabsorption within a large volume inside the sample. While advancing less than $100 \mu m$ inside the sample, the spectral shape starts recovering, and at about $350 \mu m$ has the best restoration. Here, the wings of the beam are completely inside the sample (the measured FWHM of the gaussian fit of the beam intensity is $\sim 130 \mu m$), yet very close to the edge to have minimum reabsorption. Going even farther, in less than $100 \mu m$, the peak starts becoming shorter, and within 1 mm, the shape becomes visibly distorted. The fluorescence reabsorption phenomenon will be described in more detail in section (5.1.2) together with the effect on the calculated

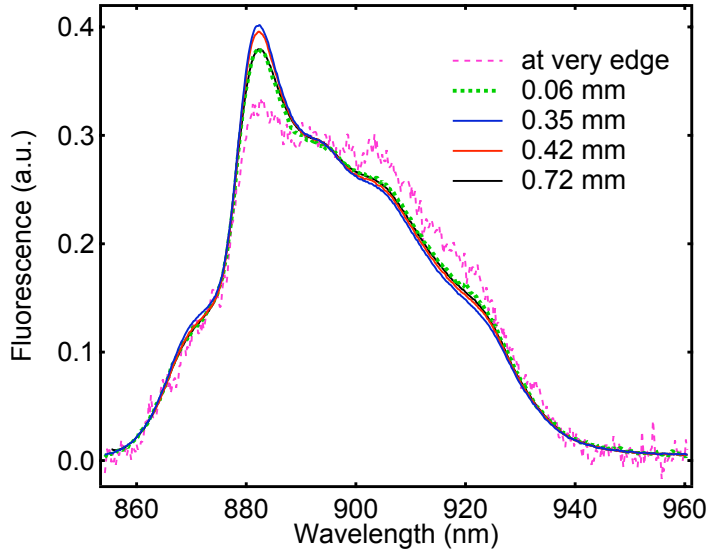


Figure 5.5: Effect of light reabsorption and scattering on the measured fluorescence spectrum.

absorption cross section spectra.

Blackbody correction

The effect of the improper blackbody correction has been investigated by comparing the emission and corresponding calculated absorption spectra obtained using a misaligned filament (which was slightly offset with respect to the optical axis of investigation as shown in Fig (5.6 (a))), with the emission and calculated absorption using the same spectra and the correct positioning of the filament. The two BB correction spectra have been normalized to the same value at the emission peak wavelength, to allow a better comparison between the results obtained in each case. The emission cross section determined using the correction from the offset filament presents a greater amplification at the long wavelength side and less at the short wavelength side of the peak, because the fluorescence signal is divided by a value of the BB signal smaller than the real one at longer wavelengths, and larger at shorter wavelengths. As seen in Fig (5.6 (b)), the two

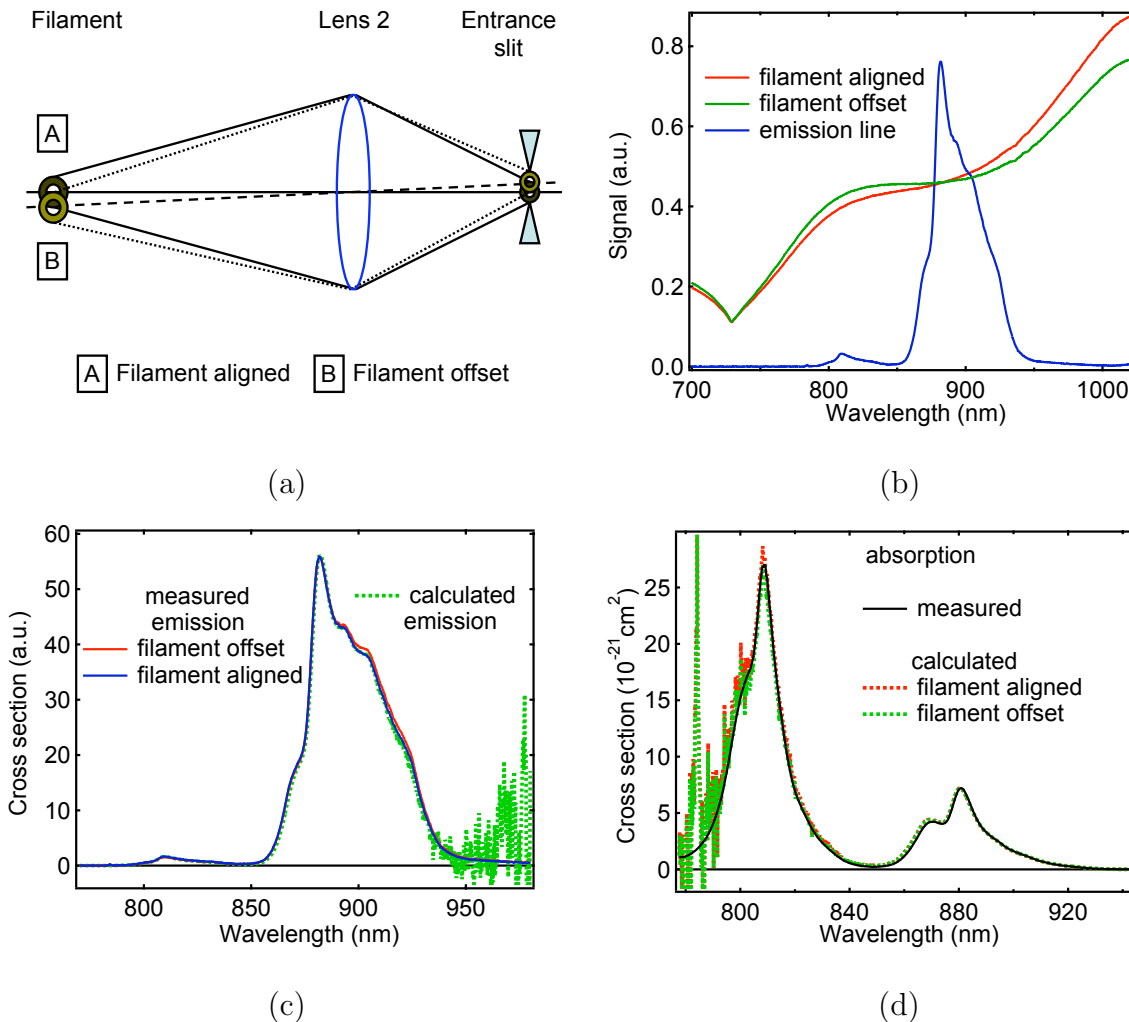


Figure 5.6: Effect on the BB correction on measured fluorescence spectrum and consequently on calculated absorption spectrum

emission spectra recorded by the detection system show significant differences across the spectral range scanned (700-1020 nm), and distort the spectral shape of the emission and calculated absorption as in Fig (5.6 (c) and (d)).

C. Comparison between measured and calculated cross sections

The calculated and the measured cross sections for Nd:silicate sample are shown in Fig.(5.7 (a) and (b)). The calculated emission cross section in Fig.(5.7 (a)) is the

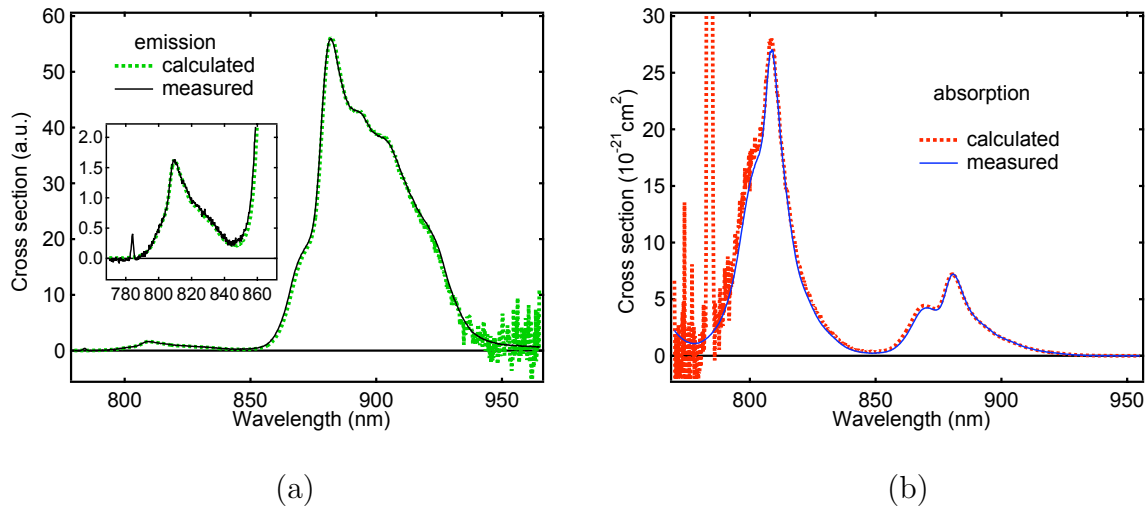


Figure 5.7: Comparison between calculated and measured spectra for: a) emission and b) absorption

result of the McCumber transform on the average of 7 absorption spectra taken in the same conditions on 3 consecutive days. Also, the calculated absorption cross section is determined from the average of 4 fluorescence data sets. The averaging process improved the signal-to-noise ratio for the measured data and therefore the calculated spectra have a more reduced amplified noise. The agreement between the calculated and measured cross section spectra is excellent for both absorption and emission spectra, along a spectral range of $\sim 2000 \text{ cm}^{-1}$. This covers the ${}^4F_{3/2} \leftrightarrow {}^4I_{9/2}$ transition, as well as the transition between the thermally excited levels (${}^4F_{5/2}, {}^2H_{9/2}$) and the ground level ${}^4I_{9/2}$.

In the inset the transition for these thermally excited levels is shown in more detail, and the agreement is also remarkable. The root-mean-square (rms) difference between the measured and calculated absorption spectra normalized to the value of the 880 nm peak is < 5%, where the average was taken over the interval where the noise is not significant (805-950 nm). For the emission spectra, the normalized rms value is less than 2% for the wavelength range of 785-950 nm, since the 882 nm emission peak that would produce eventual distortions has a much higher value.

These results are not only important because they test the validity of the McCumber theory when applied to very broad transitions, but also they represent, to our knowledge, the first application of this theory to a combined upper state consisting of two thermalized Stark manifolds. The very good agreement found in this case confirms the fact that there is a quasi-thermal equilibrium achieved between the populations of the two upper levels.

5.1.2 Nd:fluorozirconate glass

The Nd:Fluorozirconate sample studied is a FG108 glass, doped with 1% Nd^{3+} ions. The concentration of this sample is $N = 1.83 \times 10^{20} ions/cm^3$ and the thickness of the sample is 0.45 cm.

A. Absorption Measurements

The steps followed in determining the emission cross section from absorption measurements are shown in Fig.(5.8 (a)-(d)). The transmission spectra with the sample in and out of the beam light have been measured (a) and the resulting absorption cross section uncorrected for the losses has been computed (b). The corrected spectra for two different background subtractions are displayed in (c), and the corresponding calculated emission cross sections are shown in (d). We see again that two different baseline curves

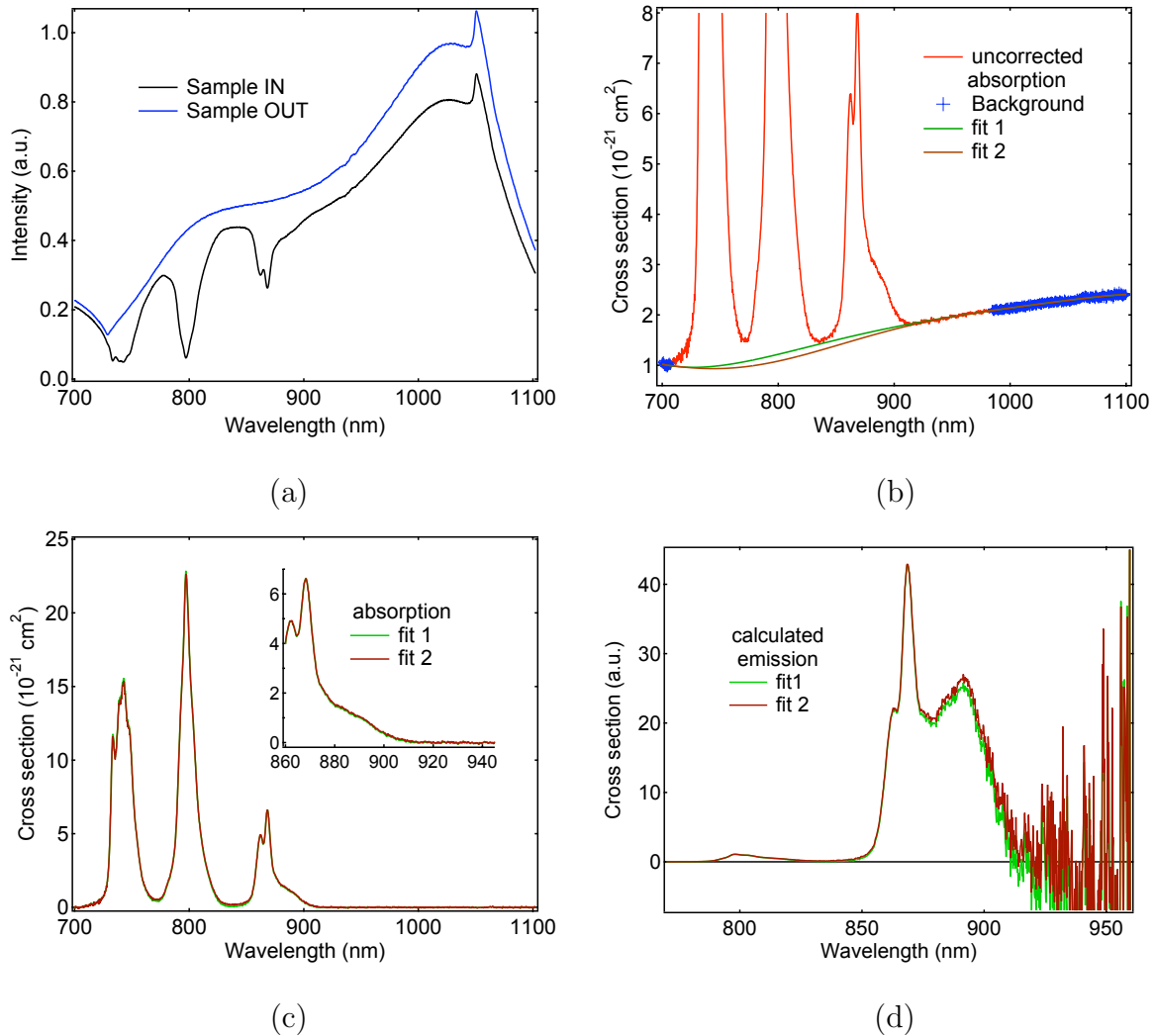


Figure 5.8: a) Transmission spectra for Nd:fluorozirconate with the sample in and out of the beam; b) Uncorrected absorption spectra and two different fit curves of the baseline; c)Absorption cross section after the baseline subtraction with expansion of the long wavelength side tail in the inset, and d) Calculated emission cross section corresponding to the two baseline fits.

that determine almost identical absorption cross sections (c), produce different tails at the long wavelength side of the calculated emission cross section.

B. Emission Measurements

Careful fluorescence measurements were performed on Nd:ZBLAN sample, and the high optical quality of this sample (smooth edges and less inhomogeneities in the sample provided reduced scattering within the sample) allowed a detailed study of the reabsorption process for a long range of distances of the laser beam to the edge of the sample.

The process of fluorescence reabsorption affects the intensity of the light corresponding to a particular transition between two Stark manifolds, as well as the spectral shape of the transition. A photon emitted at a wavelength λ_{51} by an ion performing a transition from level 5 to level 1, as shown in Fig(5.9), is reabsorbed by an ion in the ground state 1, which is promoted to level 5. In this process, the photon is not

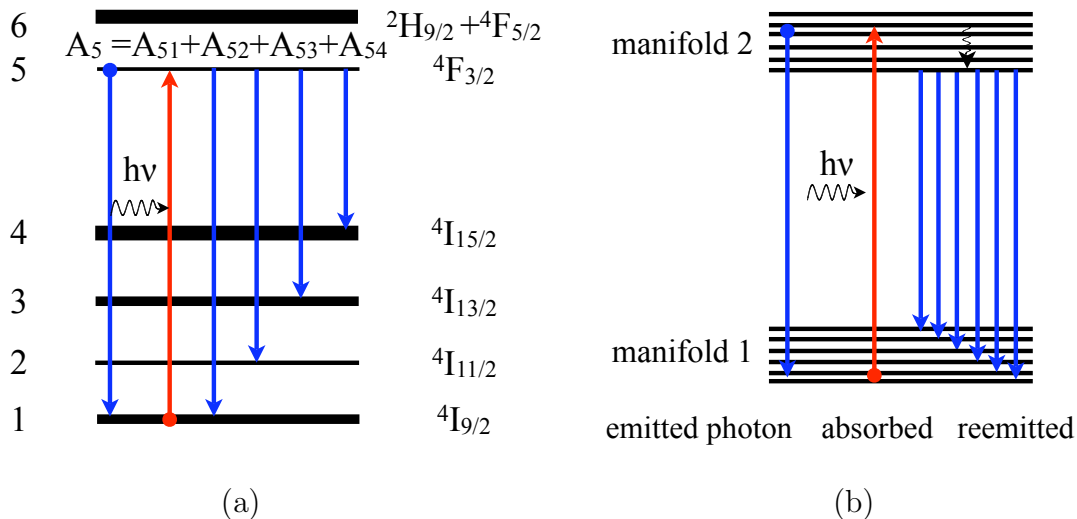


Figure 5.9: Description of the fluorescence reabsorption for Nd^{3+} transitions: a) affecting the intensity of the signal for a particular transition $5 \rightarrow 1$ by absorption and weighted reemission to any of the lower-lying Stark manifolds, and b) affecting the spectral shape of the transition between the two Stark manifolds

collected by the detector, being lost by the interaction with the atoms in the ground

state. However, the new ion now in the state 5 will emit another photon, by decaying spontaneously to any lower level 1 - 4, with probabilities A_{51} - A_{54} , this way reducing the probability of collecting the photon at λ_{51} , and increasing the chance of being collected on the longer wavelengths, corresponding to transitions to the levels 2 - 4. The intensity of the transition between the manifolds 5 and 1 will be reduced by a fraction $1 - \exp(-\alpha(\lambda_{51})l_z)$, where $\alpha(\lambda_{51})$ is the absorption coefficient at the wavelength λ_{51} of the transition and l_z is the distance along which reabsorption occurs, while the intensity of the transitions $5 \rightarrow 2$, $5 \rightarrow 3$, and $5 \rightarrow 4$ will become higher. This process is experimentally observed while the laser beam is moved away from the sample, as in Fig.(5.10 (a)). The area under the 880 nm transition becomes smaller, while the area under the

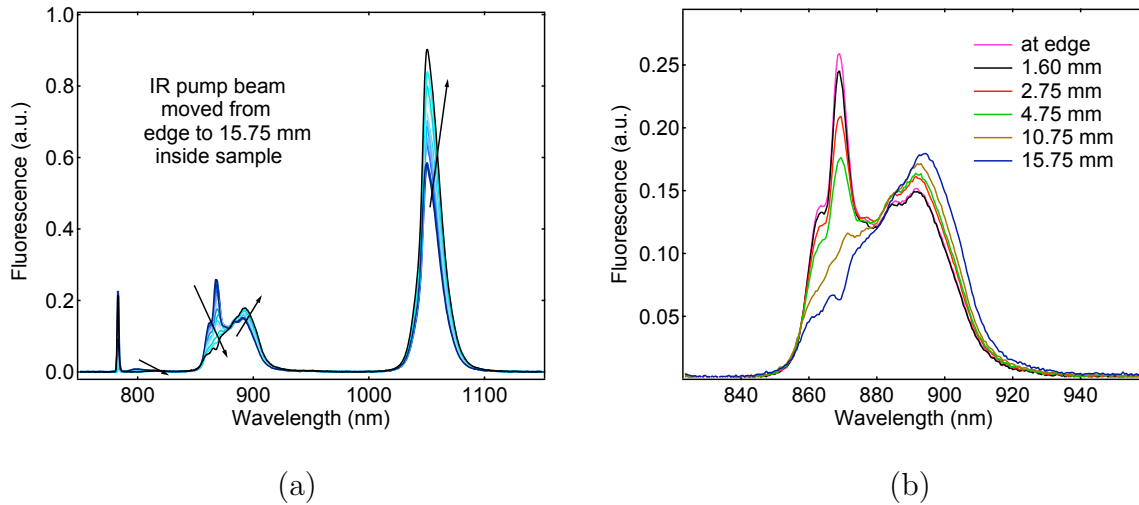


Figure 5.10: Illustration of the effect of reabsorption on the fluorescence spectrum of Nd in ZBLAN glass. As the position of the beam on the sample is moved further away from the edge, the intensity of the 880 nm transition decreases while the 1050 nm transition becomes stronger (a). Also the shape of the 880 nm transition becomes strongly distorted (b).

1050 nm transition gets larger.

The effect of the fluorescence reabsorption on the spectral shape of the transition can be similarly explained by considering two Stark manifolds as in Fig.(5.9 (b)). Pho-

tons that are emitted at the shorter wavelength side of the spectrum are absorbed by ions in the ground state (highly populated at low excitations), which are excited back to a high energy state. Due to very rapid nonradiative relaxations to lower Stark levels within the same manifold, most of the atoms will decay from the lowest Stark level, again to any of the individual Stark levels of manifold 1 with the corresponding spontaneous probability. This way, photons that otherwise would be collected at the shorter wavelength side of the transition, are now contributing to the longer wavelength side. The farther the beam from the edge and the larger the absorption coefficient at a particular wavelength, the stronger the effect of reabsorption. Fig.(5.10 (b)) shows select fluorescence curves normalized to a value at mid-range wavelength that corresponds to lower absorption coefficient and is less affected by reabsorption.

C. Comparison between measured and calculated cross sections

A similarly good agreement between the calculated and the measured spectra, as for the Nd:silicate sample, is found for Nd in fluorozirconate glass. This is illustrated in Fig.(5.11) for emission (a) and for absorption (b). The rms difference between calculated and measured absorption spectra for the 787-950 nm range, normalized to the value of the 864 nm absorption peak, is $\sim 4.4\%$. Comparing the emission spectra, the rms value normalized to the 868 nm emission peak is $\sim 1.1\%$ for the 787-915 nm interval, where the noise is not dominant.

5.2 Tm^{3+} doped samples

The three Tm-doped samples have been pumped at either 784 nm and 808 nm to excite the 3H_4 level (transition represented by dashed line in Fig.(5.12))¹ and resonant

¹Energy values used in constructing this diagram as found in ref.[20] p.107.

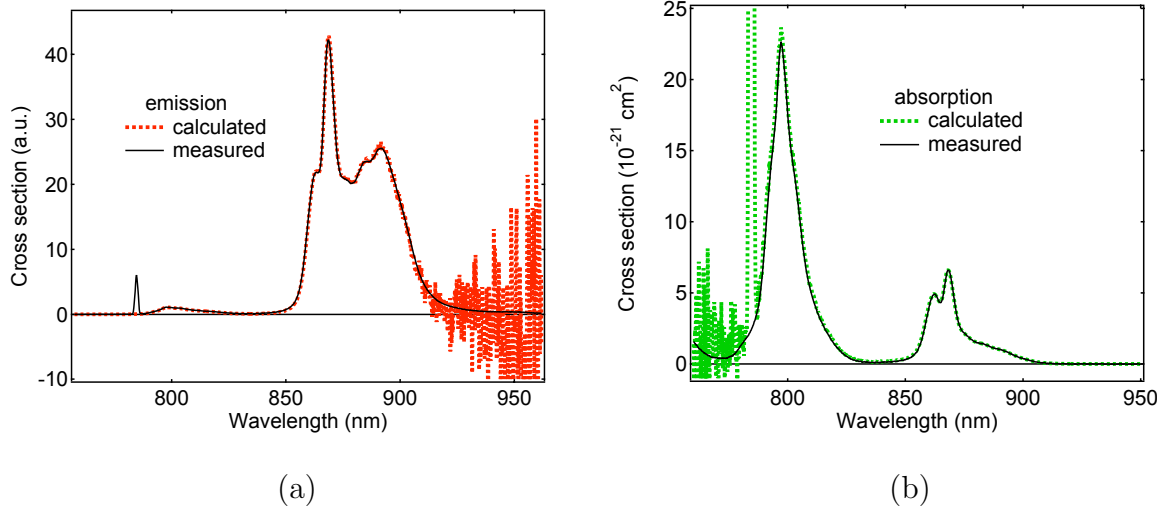


Figure 5.11: Comparison between calculated and measured spectra for emission (a) and absorption (b) cross sections in Nd:fluorozirconate sample.

fluorescence has been observed from the pumped level to the ground level 3H_6 . The McCumber theory has been applied to the transition between the same states, marked by a double arrow in the same figure.

In these samples, the strong scattered light became an issue for Tm:silicate and Tm:fluorozirconate samples, as the fluorescence signal was very weak ($\leq 50 \mu\text{V}$) and the scattered light sometimes overloaded the scale of the lock-in. Also, strong scattered light entering the monochromator can produce artifacts on the scale of measured fluorescence, by scattering on dust particles on the mirrors and diffraction grating of the monochromator.

5.2.1 Tm:fluorozirconate glass

The Tm:fluorozirconate sample used in this study was an FG122 glass, doped with 1% Tm^{3+} ions. The ion concentration was $1.76 \times 10^{20} \text{ ions/cm}^3$ and the thickness of the sample was 0.7 cm.

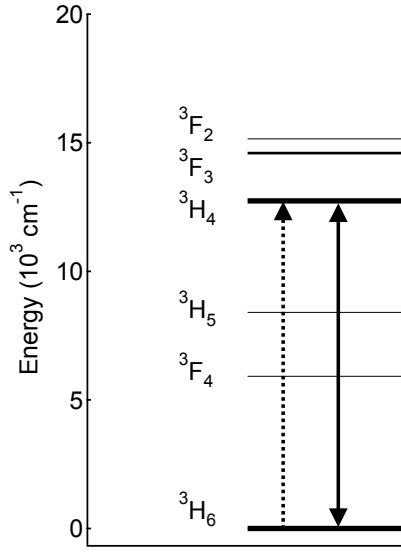


Figure 5.12: Energy level diagram for the low-lying levels of Tm^{3+}

A. Absorption Measurements

The light beam from the broadband tungsten-halogen lamp was focused on the sample and absorption spectra have been recorded with the sample in and out the path of the beam. The spectra obtained for the entire scan range from 500-1020 nm are presented in Fig.(5.13 (a)). Below 550 nm, the signal is cut off the by the long pass filter used. For wide samples, the baseline is more sloped than for thin ones, since the path of the beam is more strongly affected, parallel with its initial direction. This, however, only affects the slope of the baseline (as shown in section (5.1.1)), if the effective image of the filament on the sample is properly aligned as for fluorescence measurements. Also, this is a situation where the baseline reaches negative values (Fig.(5.13 (b))), meaning that the signal with sample in is larger than for sample out (which can also be seen in (a)). This is possible, due to the fact that the baseline is determined by a combination between the reflection losses (dependent of the incident angle of the beam on sample, which becomes

larger for larger samples), the geometry of the sample and the response of the detection system at different wavelengths. We also observe the overlapping absorption transition

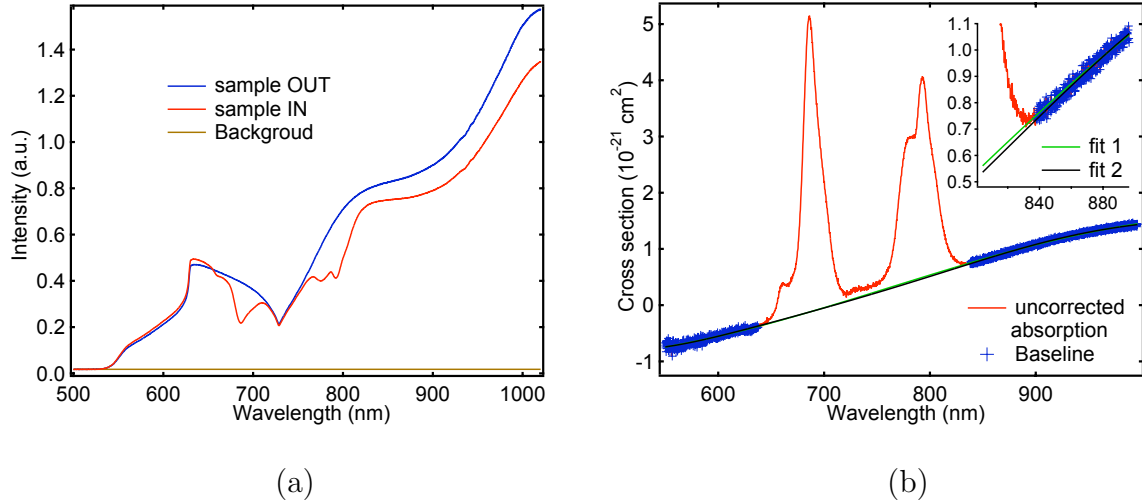


Figure 5.13: (a) Transmission spectra for Tm^{3+} in fluorozirconate glass, with the sample In and Out the beam. (b) Uncorrected absorption spectrum and two different curves that fit the baseline.

at 660 nm and 685 nm from the ground level 3H_6 to the combined levels (${}^3F_2, {}^3F_3$).

The absorption spectrum uncorrected for the experimental losses (which determines the baseline) is shown in Fig.(5.13 (b)), together with the expansion of the long wavelength tail of the 790 nm absorption line. Although very sloped, the background can be fitted with a low order polynomial, and two very similar fit curves are shown on this graph. The corrected absorption cross section for the 780 nm transition (of interest), is shown in Fig.(5.14), where we can see that although the two fit curves give almost undistinguishable differences in the measured absorption, they produce rather different long wavelength tails of the calculated emission cross section spectra. The graph also shows the measured emission cross section which runs through the points of the calculated curves, agreeing well within the noise level with both fits. The spike observed at 784 nm represents the scattered laser light. The fit #2 gives a slightly better agreement between the calculated and the measured emission cross sections.

The large noise amplification above 840 nm in the calculated curve is a consequence of the McCumber transform, which produces exponential amplification with the wavelength. This means, that the signal and the noise are equally amplified in this region of the spectra. Also, the value of the absorption cross section that creates the

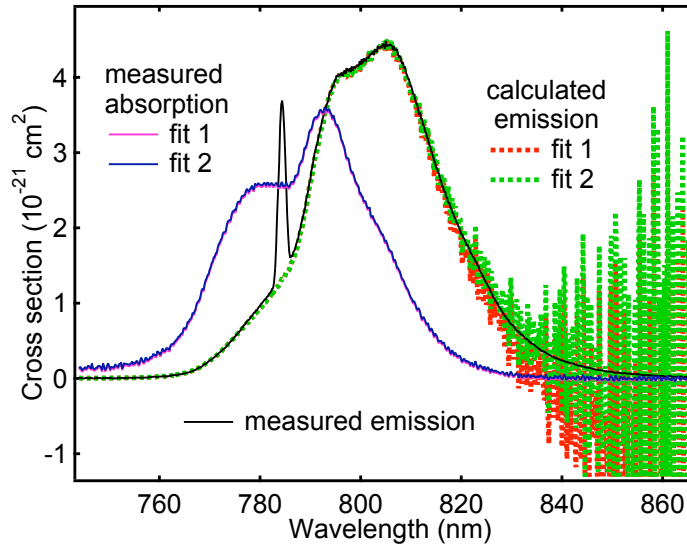


Figure 5.14: Effect of the different baseline fit curves on the calculated emission cross section spectra in Tm:fluorozirconate sample. While the two measured absorption spectra are almost indistinguishable, they determine different tails of the calculated emission at the long wavelength side.

calculated emission is small for wavelength larger than 830 nm, so the signal-to-noise ratio is reduced compared to the regions determined by large values of the absorption spectra.

B. Fluorescence Measurements

The major issue regarding the fluorescence measurements stays the reabsorption of the fluorescence inside the sample, complicated somehow by the scattered light which perturbs the measured fluorescence spectra if this is shined too close to the edge of the sample.

A number of fluorescence spectra were recorded as the position of the focused laser beam was varied in steps of 0.5 mm with respect to the edge of the sample. The results are shown in Fig(5.19 (a) and (b)), where (b) shows the change in shape and intensity of the fluorescence for only 4 different positions of the beam. We can see that

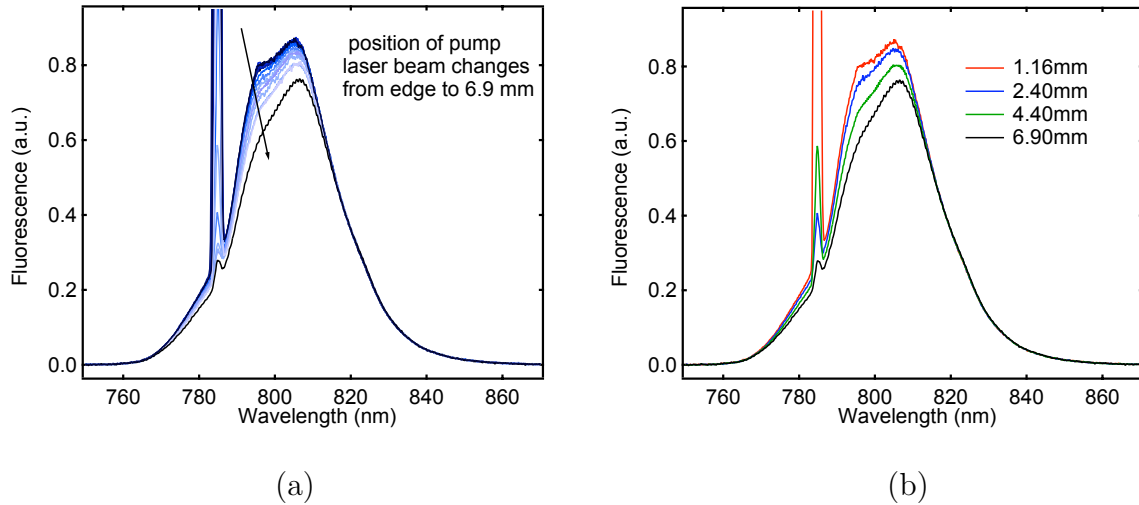


Figure 5.15: Fluorescence reabsorption in Tm:fluorozirconate glass

collection of strong scattered light affects the measured emission spectra around 784 nm when the sample is shined close to the edge. There were smoother parts on the surface and the edge of the sample that allowed discrete measurements close to edge with less scattered light, however, for the systematic study of reabsorption, scattered light could not be avoided. The amount of distortion introduced by the light reabsorption at 796 nm, along $l_z = 2 \text{ mm}$ distance (from 2.40 mm to 4.40 mm, for example) is $1 - \exp(\alpha l_z) \approx 10\%$ which is consistent with the measured emission curves for the two values mentioned.

C. Comparison between measured and calculated cross sections

Although for the study of reabsorption the sample could not be brought too close to the edge without being affected by scattered light, for the study of the McCumber theory,

smooth spots on the surface and edge of the sample where explored, and spectra with reduced scattered light have been recorded for distances as close as 0.5mm to the edge of the sample. The fraction of fluorescence reabsorbed in this case is less than 3%, as can also be seen in Fig.(5.16) from the excellent agreement with the calculated curve. Several spectra were recorded at those locations, in order to improve the signal-to-noise

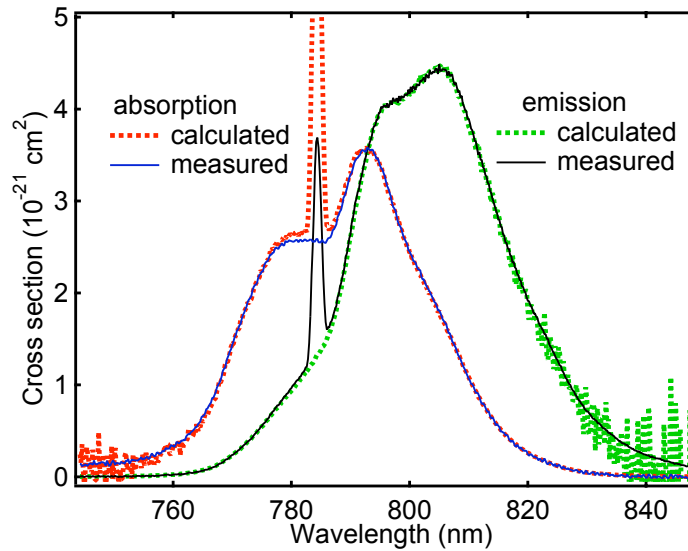


Figure 5.16: Comparison between the calculated and measured cross section spectra for Tm:fluorozirconate sample pumped at 784 nm. The spike at 784 nm represents the scattered laser light.

ratio. From Fig.(5.16) we see that the agreement is excellent not only for the emission, but also when comparing the absorption cross sections, for a 1250 cm^{-1} spectral range of the transition and away from the laser light.

The feature at 784 nm in the calculated absorption spectrum represents the scattered light measured in fluorescence. To test that this is really what we see, we pumped this sample at 808 nm, and this spike in the measured fluorescence moves now at 808 nm. Fig.(5.17) shows the calculated and measured emission and absorption spectra for this situation. The agreement between the calculated and measured cross section spectra is very good, across the entire spectral line, away from the scattered line.

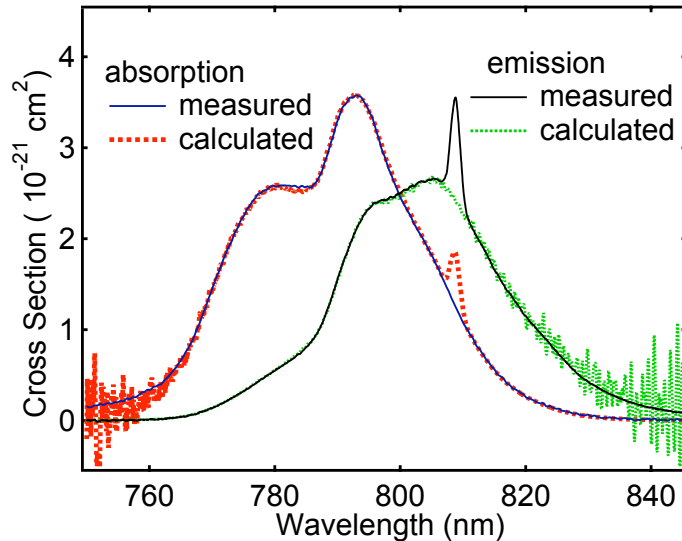


Figure 5.17: Comparison between the calculated and measured cross section spectra for Tm:fluorozirconate sample pumped at 808 nm. The feature representing the scattered laser light is now to 808 nm.

5.2.2 Tm:fluorophosphate glass

The Tm:fluorophosphate sample studied was a high fluorine to oxygen ratio LG137 glass, doped with 1% Tm^{3+} ions. The ion concentration was $2.35 \times 10^{20} \text{ ions/cm}^3$ and the thickness of the sample was 0.7 cm.

A. Absorption Measurements

Absorption spectra in Tm:fluorophosphate sample have been obtained following the same procedure as for all the other samples, and three different corrected spectra, corresponding to different baseline fittings are shown in Fig(5.18). At the scale of the transition, the overall shapes of the three absorption spectra do not differ much from each other, but they show discrepancies in the way the absorption wings decay to zero above 830 nm, as can be seen from the expansion in the inset. These wings determine the shape of the emission cross section calculated with the McCumber relation. It is very clear

that the cross section calculated from fit #1 is not realistic, since is determined from a negative cross section. As for the other two situations, the measured emission cross section fits right between the calculated curves determined by fit #2 and fit #3. We can

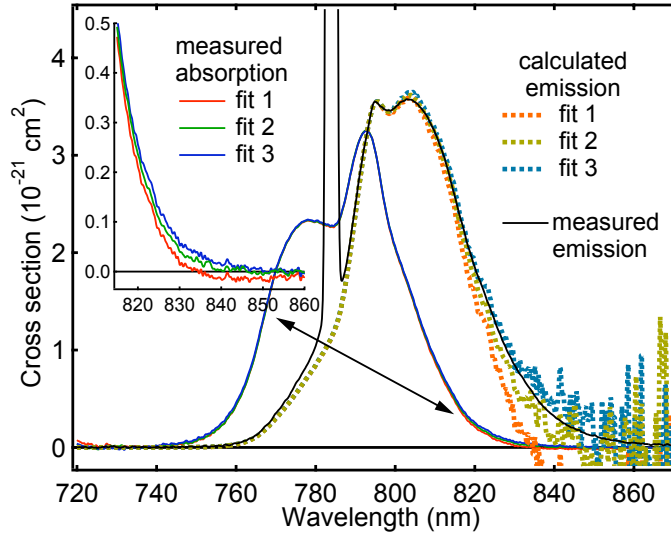


Figure 5.18: Effect of the different long wavelength tails of the absorption cross section on the calculated spectra for Tm:fluorophosphate sample.

therefore conclude that there is a good agreement between the measured and calculated emission cross section, within the noise limits and uncertainties regarding the baseline subtraction.

B. Fluorescence Measurements

The weak emission signal collected from this sample compared to Nd:fluorozirconate, is determined by the contribution of three factors: a) higher phonon energy of the fluorophosphate glasses means that fewer phonons are required to bridge the gap between the 3H_4 and 3H_5 levels, this increasing the nonradiative transition rate to the 3H_5 , therefore reducing the radiative rate from level 3H_4 , b) slightly less efficient excitation (about 10%) at the same pump wavelength, and c) less high quality of the glass determines

more pump light to be scattered on the surface of the sample instead of penetrating the sample to produce excitations.

A study of the reabsorption regarding the strength of the transition and the spectral shape has been performed for positions of the laser on the sample varying from the edge to 6.93 mm inside the sample. The results are plotted in Fig.(5.19 (a) and (b)). As expected, the distortion in the spectral shape caused by the reabsorption increases

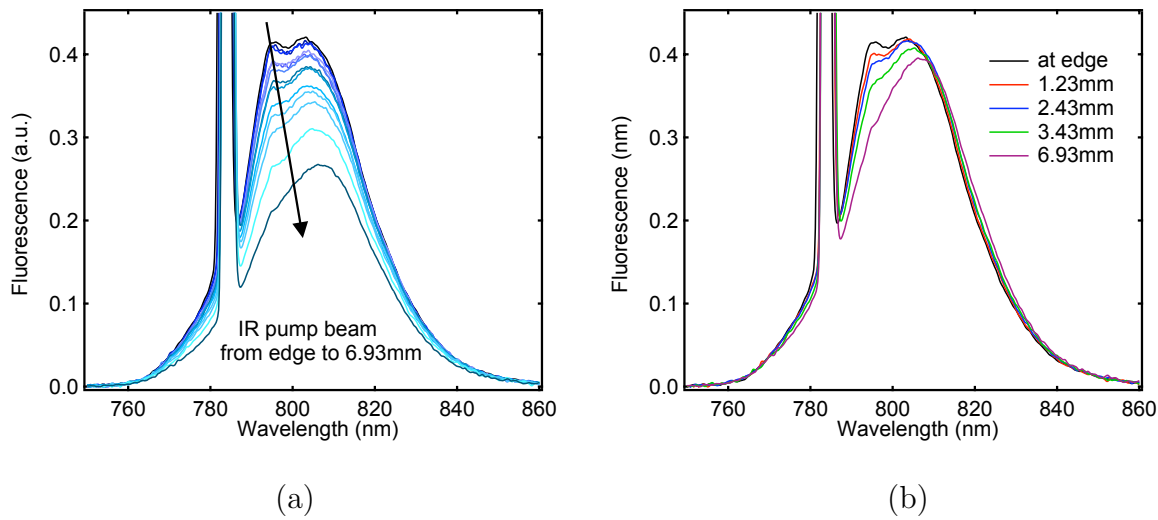


Figure 5.19: Illustration of the effect of reabsorption on the fluorescence spectrum of Tm in fluorophosphate glass. As the position of the beam on the sample is moved further away from the edge, the intensity of the transition decreases (a). Also the shape of the transition becomes strongly distorted (b) (The curves have been rescaled by a constant factor to give the best spectral match).

with the distance from the edge. Also, as the beam is moved farther into the sample, the scattered light becomes weaker. The effect of fluorescence reabsorption on the calculated absorption cross section is shown in Fig.(5.20) for three different emission curves: at the edge of the sample, at 2.43 mm, and 3.43 mm from edge. The part of the transition that is most affected corresponds to the highest absorption peak, at 793 nm. (by a fraction of $\sim 7\%$ per mm length). Also, from the graph we can see that this is not the only disagreement between the measured and the calculated absorption cross section. There

is another feature at the wavelength of the laser, produced by the scattered light, whose short wavelength side wings become exponentially amplified with the wavelength. This

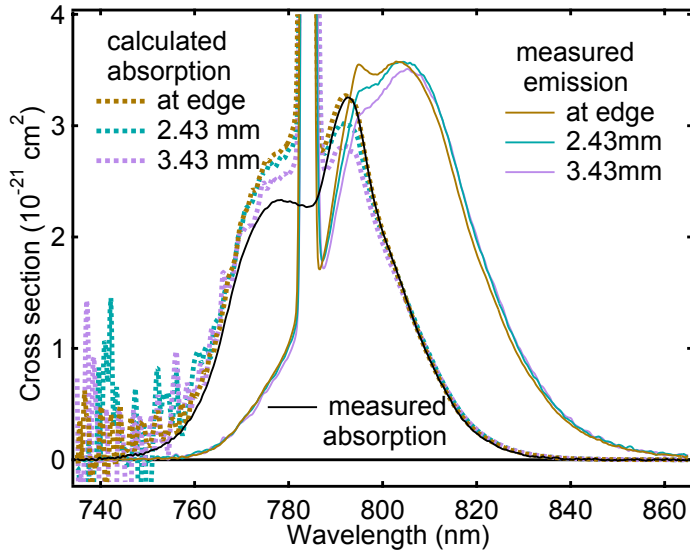


Figure 5.20: Effect of the fluorescence reabsorption on the calculated emission cross section spectrum of Tm in fluorophosphate glass for three different positions of the focused laser beam on the sample.

feature becomes less strong for the 2.43 mm, and 3.43 mm spectra, as the scattered light weakens up inside the sample. So, a better agreement between the measured and the calculated cross sections is found at wavelengths < 770 nm for less scattered light.

C. Comparison between measured and calculated cross sections

Comparing the calculated and measured cross sections we find a very good agreement both for absorption and for emission cross section spectra as seen in Fig.(5.21), at wavelengths away from the laser line. To further study the agreement around 784 nm, we pumped the Tm samples at 808 nm and the feature moves with the laser transition at 808 nm. The signal-to-noise ratio for fluorescence measurements in this case is very low, resulting in large amplification of the noise for the calculated absorption cross section

spectra. However, the measured cross sections fit well the calculated one, for the range of wavelengths away from the 808 nm laser line. Although the measurements at 808 nm

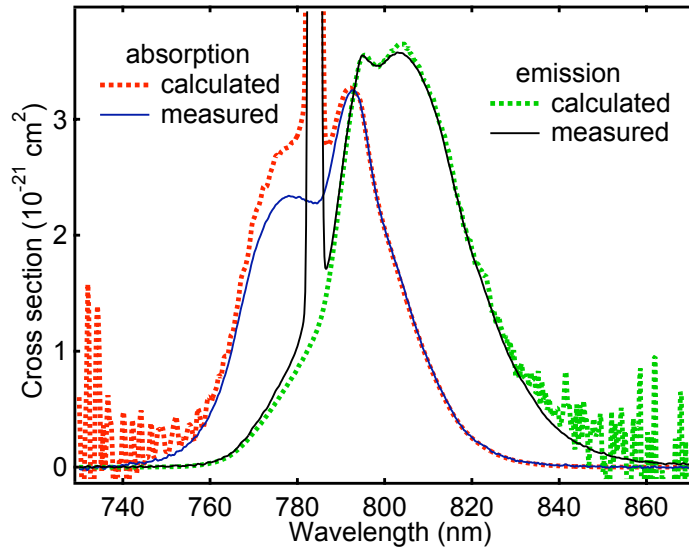


Figure 5.21: Comparison between calculated and measured spectra for emission and absorption cross sections in Tm:fluorophosphate sample.

pump wavelength are not very revealing for the McCumber theory because of the large noise, the are very relevant in explaining the existence of the feature found at the laser wavelength.

5.2.3 Tm:silicate glass

We used a LG163 glass doped with 1% Tm ions, with a concentration of $2.83 \times 10^{20} \text{ ions/cm}^3$ and thickness 0.55 cm. The phonon energies in oxide glass are much larger than in fluoride glass, which facilitates nonradiative relaxation by multiphonon emission to the lower levels. The consequence of this in Tm:silicate glass, is much lower fluorescence signal from the 3H_4 , since the ions excited to this level decay rapidly to the 3H_5 and 3F_4 levels.

Measured transmission spectra with the sample in and out the beam are shown in

Fig.(5.22 (a)), together with two similar baseline curves and the expansion of the long wavelength side of the corrected absorption spectra in the inset. The corresponding

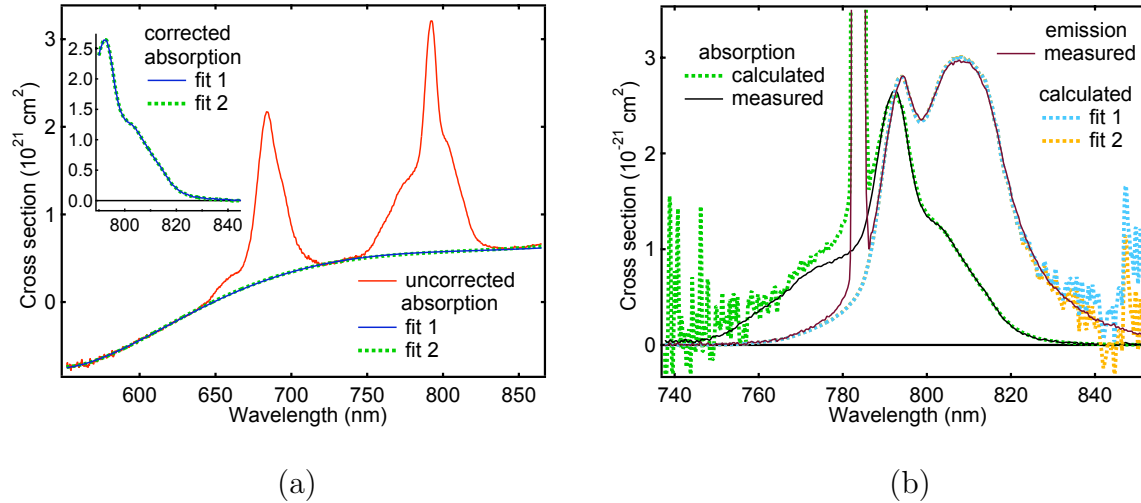


Figure 5.22: (a) Uncorrected absorption cross section and two very similar baseline fits, together with the long wavelength side of the corrected absorption determined using the two fit curves. (b) Comparison between calculated and measured spectra for emission and absorption cross sections in Tm:silicate sample.

calculated emission cross section spectra are shown in Fig.(5.22 (b)). In the same figure we displayed the measured absorption and emission cross sections (averaged over a number of spectra taken in identical conditions to reduce the noise), and also the calculated absorption cross section.

Comparing the emission spectra, we find that the measured curve fits well the calculated one, except for a portion around the laser line, at 784 nm. In absorption, the agreement between the measured and the calculated curves is also good, but the wings of the laser transition introduce a larger discrepancy at shorter wavelength side of the line, caused by the exponential amplification of the McCumber equation.

The reabsorption process in the Tm:silicate sample was again investigated, in order to determine the optimum distance from the edge that minimizes reabsorption, also does not bring an excessive amount of scattered light in the measured spectra. The recorded

fluorescence as the position of the focused laser beam on the sample was varied from the edge to 4.07 mm inside the sample, is shown in Fig.(5.23 (a) and (b)). The shape of

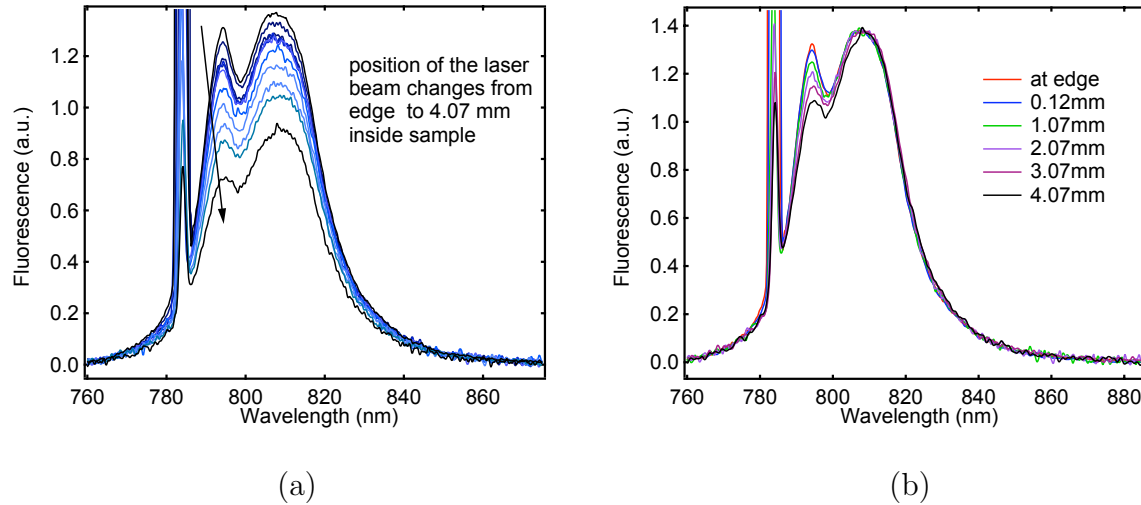


Figure 5.23: Fluorescence reabsorption in Tm:silicate: (a) the intensity of the spectral line attenuated as the position of the beam moves away from the edge of the sample; (b) the shape of the transition is more distorted with the distance

the emission is distorted particularly within the 785-800 nm spectral range, where the absorption coefficient is almost double than for the rest of the transition.

The effect of the reabsorption on the calculated absorption cross section within ~ 1 mm distance from the edge is shown in Fig.(5.24). The calculated spectrum does not reconstruct well the absorption peak at 792 nm, it does, however, come closer to the measured spectrum at wavelengths shorter than the laser wavelength, due to the fact that inside the sample there is less scattered light. The agreement at the long wavelength side of the spectra is excellent, for both curves (at edge and at 1.07 mm).

5.3 Er^{3+} doped samples

The McCumber theory has also been tested on Er-doped silicate and fluorozirconate samples. Er was pumped at 808 nm to excite the $^4I_{9/2}$ level, and fluorescence was col-

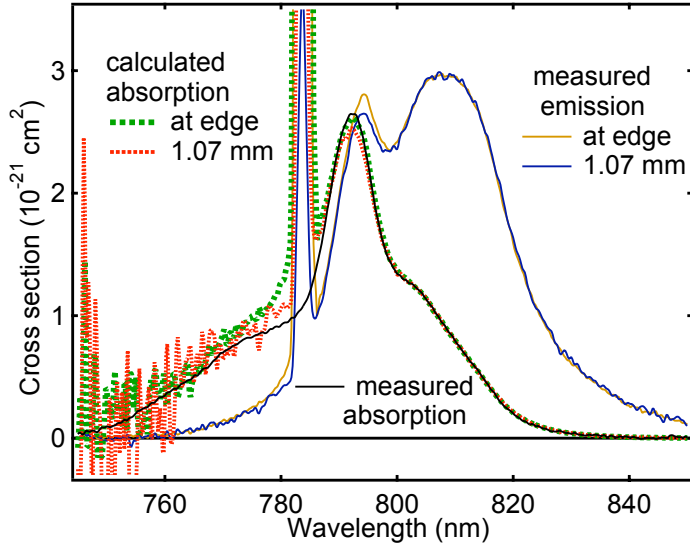


Figure 5.24: Effect of the reabsorption on the calculated absorption cross section in Tm:silicate sample.

lected from the levels ${}^4I_{13/2}$ to the ground level ${}^4I_{15/2}$ in silicate glass, and from both ${}^4I_{11/2}$ and ${}^4I_{13/2}$ to ${}^4I_{15/2}$ in fluorozirconate. These transitions are shown in Fig.(5.25), where the dashed arrow represents the pump transition, and the solid arrows represent the absorption emission pairs on which we tested the McCumber theory. From the level ${}^4I_{9/2}$ the atoms decay rapidly to the next lower level ${}^4I_{11/2}$. In silicate glass, the nonradiative decay rate from the level ${}^4I_{11/2}$ to ${}^4I_{13/2}$ is very high, due to the larger phonon energy of oxide glasses compared to fluoride glasses². This causes rapid relaxation of the ions from this level to the lower ${}^4I_{13/2}$ level, and as a result, no fluorescence is measured from ${}^4I_{11/2}$ level in silicate glass.

²The phonon energy in fluorozirconate glass is $\sim 500 \text{ cm}^{-1}$, while in silicate glass is $\sim 1100 \text{ cm}^{-1}$ (from ref.[20] p.37).

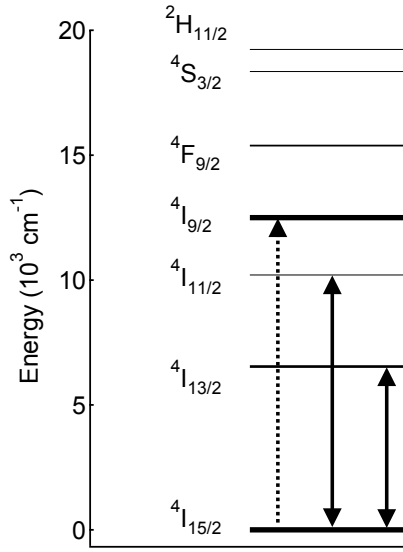


Figure 5.25: Energy level diagram for the lower-lying levels of Er^{3+} .

5.3.1 Er:silicate glass

The Er:silicate sample studied was a LG22 glass, with an ion concentration of $2.46 \times 10^{20} \text{ ions/cm}^3$ and thickness 0.5 cm. Absorption and fluorescence measurements for the 1550 nm transition were performed using the cooled germanium detector as explained in section (4.3.1).

A. Absorption Measurements

The measured absorption cross section has been determined again comparing the sample IN and OUT transmission spectra as shown in Fig.(5.26 (a)). The set of features around 1400 nm in this graph represent the absorption spectrum of the OH radical from atmosphere. It is very important that the two spectra are taken consecutively, during the same day, so that the amplitude of the OH absorption spectrum does not vary much between the two measurements. This way the measured absorption spectra for the Er

transition at 1550 nm is not affected much. This is what we see in Fig.(5.26 (b)) for the absorption cross section spectrum, uncorrected yet for the background. The baseline is then subtracted by fitting it with three different curves, and the resulting measured spectra are shown in Fig.(5.26 (c)). The corresponding calculated emission spectra are shown in Fig.(5.26 (d)). The importance of the proper baseline subtraction has been

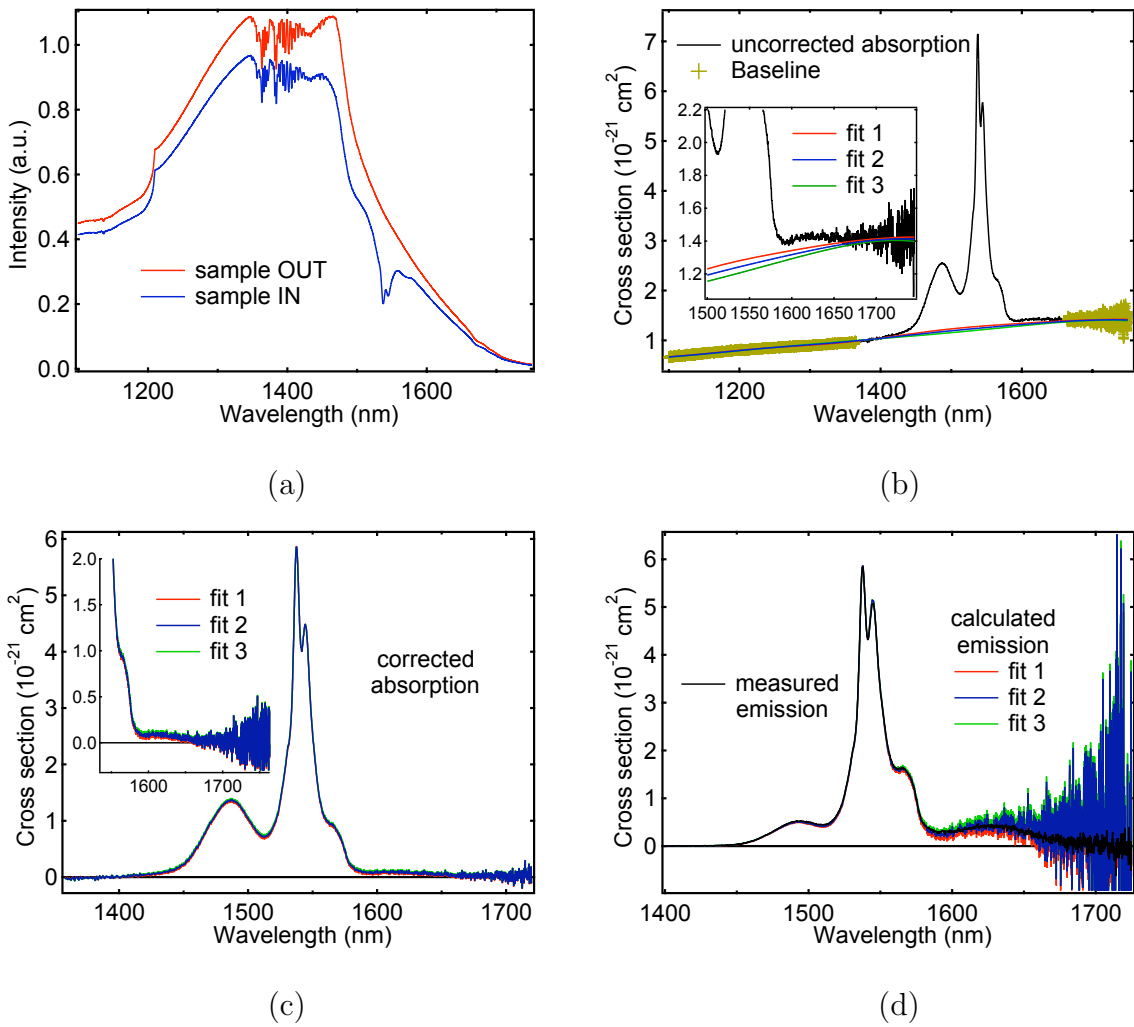


Figure 5.26: Determination of the absorption cross section for three different bkg. fit

stressed many times along the way, and here it also emphasized by showing the effect of the three fitting curves on the calculated emission cross section spectra. Also displayed

on this graph, the measured emission spectrum fits well within the three calculated spectra.

For wavelengths larger than 1650 nm, the sensitivity of the germanium detector drops down (Fig.(5.26 (d))), resulting in a very low signal-to-noise ratio for the signal measured in this spectral region. This noise is amplified when the two transmission spectra are divided by each-other to calculate the absorption cross section, end again exponentially by the McCumber formula, when calculating the emission cross section. This explains the very large noise at wavelengths greater than 1650 nm. The instrumental resolution of 1.44 nm used, allows us to resolve the narrow individual Stark peaks of this transition, yet the slits are wide enough for a good signal-to-noise ratio.

B. Fluorescence Measurements

Fluorescence measurements have been performed for various positions of the focused laser beam on the sample with respect to the edge of the sample. The purpose was again to find the optimum distance from the edge that minimizes the reabsorption of the fluorescence inside the sample. For this, the distance was varied in steps of 0.10 mm, from edge to 0.70 mm, and then in steps of 0.50 mm up to the final distance of 2.20 mm from edge. Three of these spectra are presented in Fig.(5.27 (a)), for beam at the very edge, at 1.20 mm and 2.20 mm from edge. The region 1530-1550 nm of the emission spectrum is the most affected by reabsorption, since it corresponds to very high absorption peaks compared to the rest of the absorption transition. The calculated absorption cross sections corresponding to these three curves are shown in Fig.(5.27 (b)), together with the measured absorption spectrum. Very good agreement between the calculated and the measured curves is obtained when the sample is properly illuminated at the edge. The attenuation in the intensity of the 1538 nm peak along a 1.20 mm distance can be determined using the measured absorption cross section and

the ion concentration. This is about $\sim 16\%$ for the 1538 nm peak, and is very close to

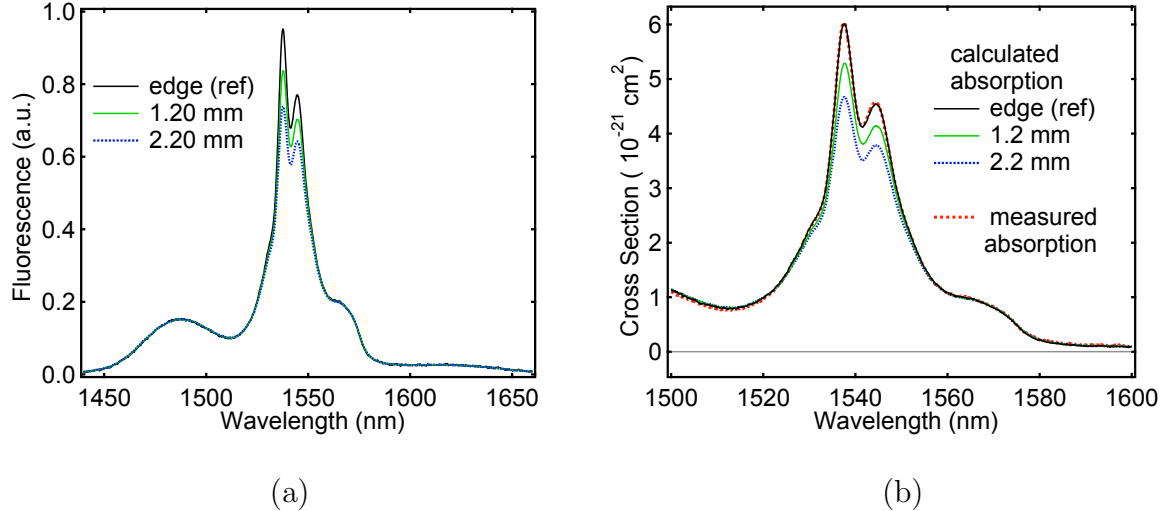


Figure 5.27: Reabsorption in Er:silicate

the attenuation observed experimentally in Fig.(5.27).

C. Comparison between measured and calculated cross sections

The calculated and measured absorption and emission spectra are compared in Fig.(5.28). The agreement between measured and calculated cross section spectra is excellent, across the entire $\sim 1000 \text{ cm}^{-1}$ spectral width of the transition. This agreement can be quantified by calculating the rms deviation between the two curves, normalized to the value of the measured peak. This was less than 1% for this transition, where the average was taken for the interval where the noise was not dominant (1400-1650 nm for example). This is in very good agreement with the theoretical predictions [47] that modeled this type of system for typical widths of rare earth ions in glass.

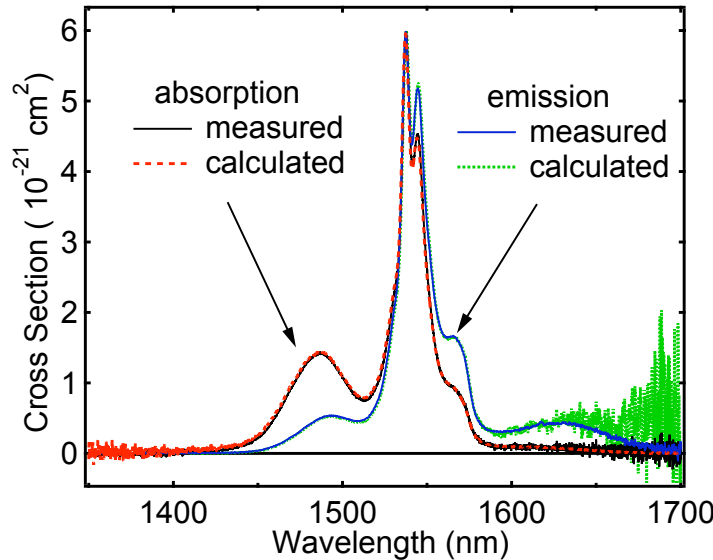


Figure 5.28: Comparison of calculated and measured absorption spectra for the 1550 nm transition in Er:silicate

5.3.2 Er:fluorozirconate glass

The Er:fluorozirconate sample investigated is a Er₂ZBLANI glass, doped with 1% ErF₃, with an ion concentration of $1.76 \times 10^{20} \text{ ions/cm}^3$ and thickness 0.275 cm. In this glass we investigated the 1550 nm and the 980 nm transitions.

1550 nm transition

For the 1550 nm transition we investigated the effect of the background fit choice on the measured absorption and the calculated emission spectra. The results for three different absorption cross sections obtained with different data sets and different baselines are shown in Fig.(5.29 (a) and (b)). The increasingly larger noise at the long wavelength side of the spectral line is determined by the low sensitivity of the germanium detector above 1650 nm. This is exponentially amplified by the McCumber relation when the emission cross section spectra are calculated. The measured emission cross section is

displayed for comparison on the same graph (b), and within the noise limits, it agrees well with the calculated spectra, especially with fit #3. The small spike at 1616 nm is

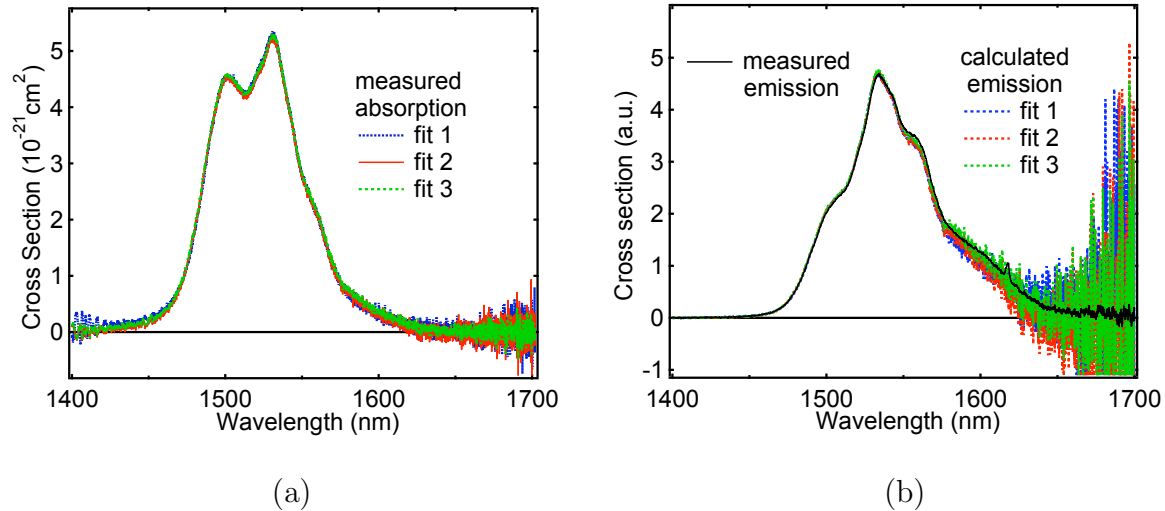


Figure 5.29: Effect of the background choice on the measured absorption (a) and calculated emission (b) for the 1550 nm transition in Er:fluorozirconate glass

caused by the scattered light in second order.

The rough edges of this sample makes difficult the optimization of the distance from edge for minimum reabsorption. Within only 0.40 nm from edge (as shown in Fig.(5.30), the shape is distorted by reabsorption within the volume of the sample, while closer to the edge is distorted due to light trapping. The attenuation for this sample is about 4% within 0.4 mm distance, more significant at the 1500 nm and 1530 nm emission peaks.

The comparison between the calculated and the measured cross section spectra is shown in Fig.(5.32) for both emission and absorption. In emission, the agreement is very good, within the noise limits, and seems even better in absorption, where the noise from measured fluorescence is much lower at the short wavelength side at the spectral line. The very slight disagreement at the two absorption peaks can be explained by reabsorption within 0.4 mm distance from the edge of the sample, or by light trapping

as discussed earlier for Fig.(5.30).

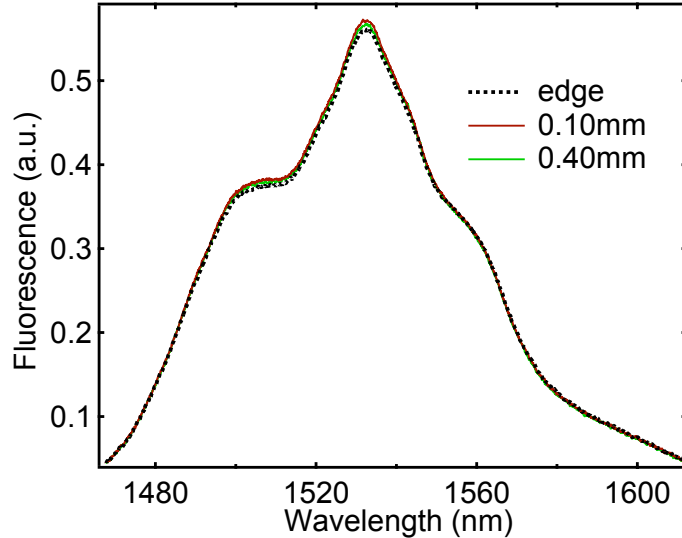


Figure 5.30: Reabsorption at 1550 nm in Er:fluorozirconate glass

980 nm transition

The transition at 980 nm in Er:fluorozirconate was investigated, and the spectra were measured using the silicon photodetector. The absorption transition in Er at this wavelength is very weak, resulting in a low signal to noise ratio for the measured absorption cross sections, and even lower for the calculated emission cross section spectra. The same steps have been followed in determining the calculated emission spectra, and the results are shown in Fig.(5.31 (a)-(d)). From the measured transmission with the sample in and out (a), we determined the uncorrected absorption cross section (b), this has then been corrected by subtracting different baselines (c), and the emission cross section is calculated using the McCumber relation (d). The three background fits give different behaviors for the long wavelength tail of the transition, and the one that gives best agreement seems fit #1 (also see (b)), which looks indeed the most appropriate to fit

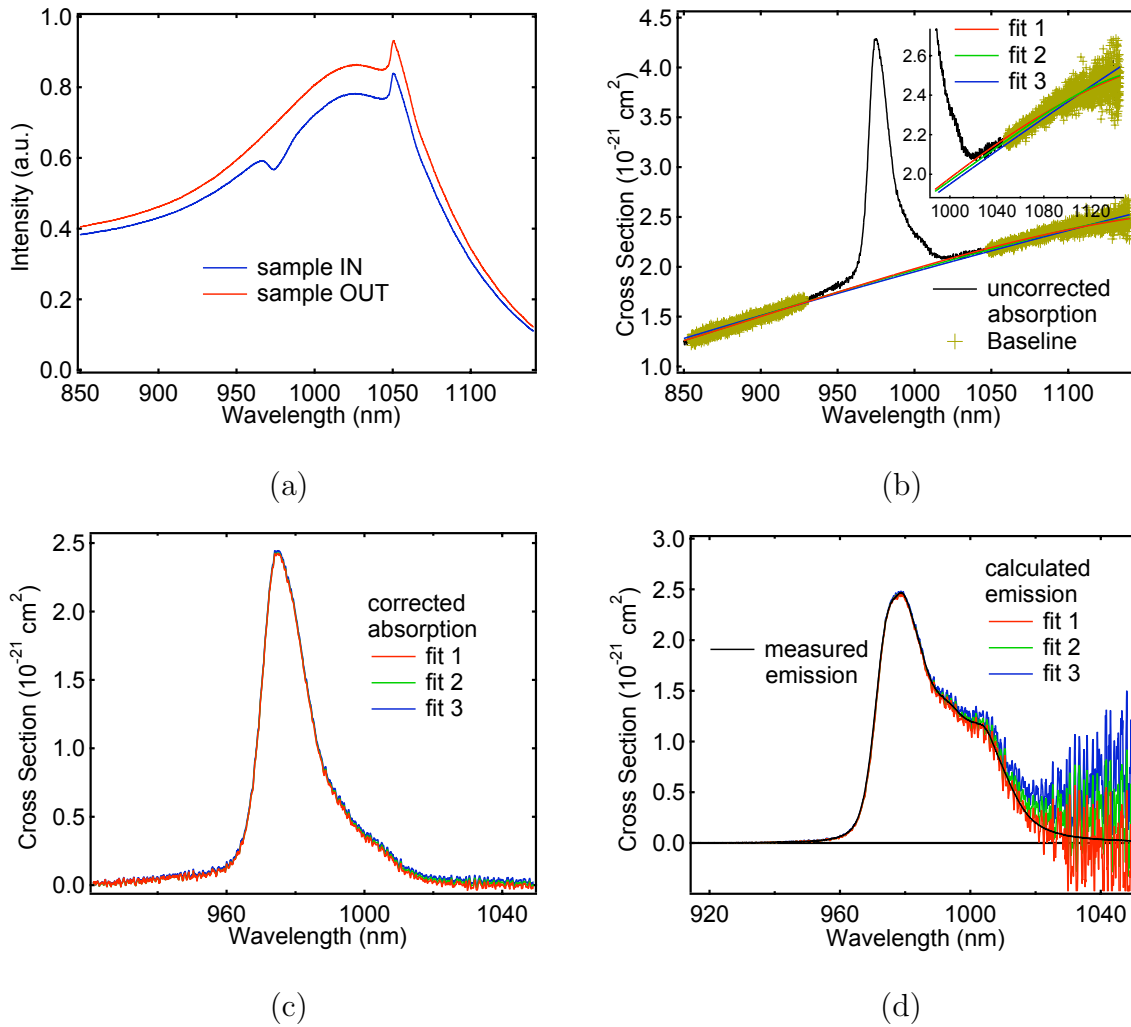


Figure 5.31: Determination of the absorption cross section for the 980 nm transition in Er:fluorozirconate for three different background fit curves. (a) Transmission spectra with sample In and Out the beam; (b) Uncorrected absorption spectra with three different baseline fit curves; (c) corrected absorption cross section spectra for each fit; (d) The corresponding calculated emission cross section spectra

most points of the baseline.

Since the absorption transition at 980 nm in Er:fluorozirconate glass is very weak, no complications due to reabsorption are encountered. The fluorescence signal from

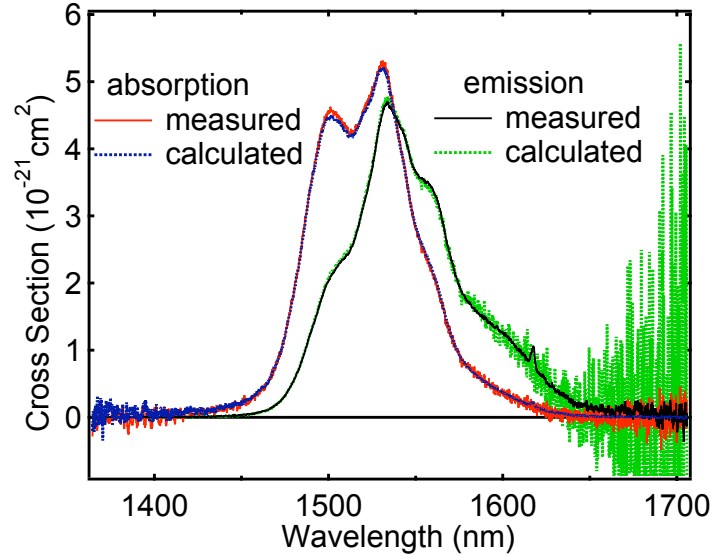


Figure 5.32: Comparison between measured and calculated cross sections for the 1550 nm transition in fluorozirconate glass

$^4I_{11/2}$ to $^4I_{15/2}$ is strong, and a good signal-to-noise ratio is obtained for the measured emission cross section spectra.

The calculated and measured cross sections are presented in Fig.(5.33). While in comparing emission spectra, the noise is a large uncertainty factor, the agreement in absorption between the same two sets of data is excellent. This is determined by the very good signal-to-noise ratio for fluorescence measurements in the region that is amplified by the McCumber transform, compared to the absorption data that are much noisier on the amplified side, and are also the subject of uncertainties in the baseline selection. There are no baseline subtraction uncertainties when the absorption cross section is determined from fluorescence measurements, since any background can be precisely determined by blocking the laser beam. The absorption cross section spec-

tra determined from fluorescence measurements may actually be more accurate than

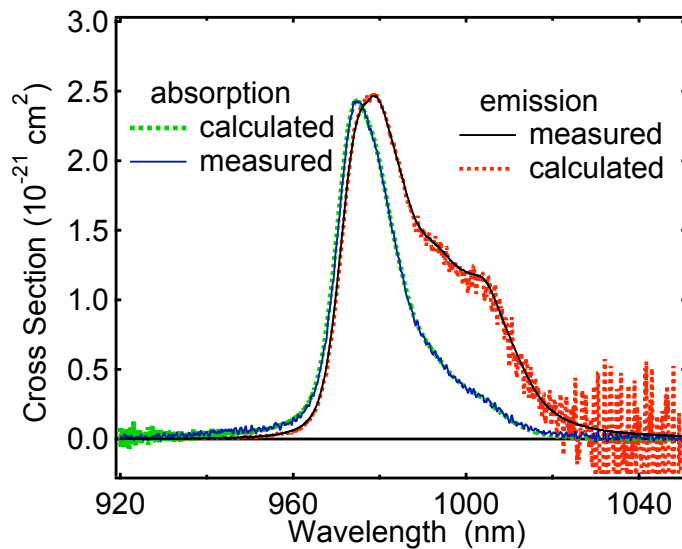


Figure 5.33: Comparison between measured and calculated cross sections for the 980 nm transition in Nd:fluorozirconate glass

the measured absorption itself, if all the issues regarding fluorescence reabsorption and blackbody correction are properly accounted for.

Chapter 6

Low temperature study of the McCumber theory

To do a further testing of the McCumber theory, we performed absorption and fluorescence measurements at temperatures as low as 130 K, on Nd:fluorozirconate and Nd:silicate samples presented in the earlier chapter (5). The importance of this study consists not only in setting the limits for a reliable determination of the emission or absorption cross sections from one another, but also could provide very useful information about the spectral width of the transition.

6.1 Expectations

As emphasized in section (3.3.2), the degree of distortion depends on the type of broadening and the temperature of the sample. Our room temperature study on a variety of rare earth doped samples showed that the rms deviation caused by spectral broadening with respect to the value of the peak is less than 5%. To understand and distinguish between different aspects that contribute to the distortion of the lineshape due to the

break down of the McCumber theory, we will discuss separately the distortion of single peak transition, and then the change in a multiple peak line.

6.1.1 Single peak distortion

For a single peak, the emission and the absorption cross sections are identical at all frequencies: $\sigma_{ji}^{actual}(\nu) = \sigma_{ij}^{actual}(\nu)$. From measured (actual) absorption spectra, the McCumber theory, however, predicts an emission cross section given by

$$\sigma_{ji}^{McC}(\nu) = \sigma_{ij}^{actual}(\nu)e^{-h(\nu-\nu_{ij})/k_B T} = \sigma_{ji}^{actual}(\nu)e^{-h(\nu-\nu_{ij})/k_B T} \quad (6.1)$$

where ν_{ij} is the peak frequency. The spectral shape of the actual emission and absorption spectra is contained in the lineshape functions: Lorentzian $g_L(\nu)$ for homogeneous broadened peaks, or Gaussian $g_G(\nu)$, for peaks inhomogeneously broadened.

Homogeneous broadening

For a spectral line which is purely homogeneously broadened, the actual emission, absorption and McCumber emission lineshapes are given by

$$\sigma_{em}^{actual}(\nu) = \sigma_{abs}^{actual}(\nu) = \sigma_0 \left(\frac{\Delta\nu_H}{2} \right)^2 \frac{1}{(\nu - \nu_0)^2 + (\Delta\nu_H/2)^2} \quad (6.2)$$

$$\sigma_{em}^{McC}(\nu) = \sigma_0 \left(\frac{\Delta\nu_H}{2} \right)^2 \frac{1}{(\nu - \nu_0)^2 + (\Delta\nu_H/2)^2} e^{h(\nu_0 - \nu)/k_B T} \quad (6.3)$$

The factor $\sigma_0(\Delta\nu_H/2)^2$ is constant across the line, and only contributes to the value of the amplitude of the peak. In the majority of the situations discussed subsequently here, this factor will be omitted, since our study is concentrated entirely on the spectral shape.

The McCumber predicted emission lineshape for a width of 50 cm^{-1} is shown in Fig.(6.1) (a), at two different temperatures (300 K and 150 K), together with the actual lineshape. The peak value was selected at 12000 cm^{-1} , corresponding to our

experimental range of interest. Indeed, the amplification of the Lorentzian tails of the spectral line is noticeable at room temperature, and becomes very significant for a lower temperature. To characterize the degree of distortion introduced by the McCumber

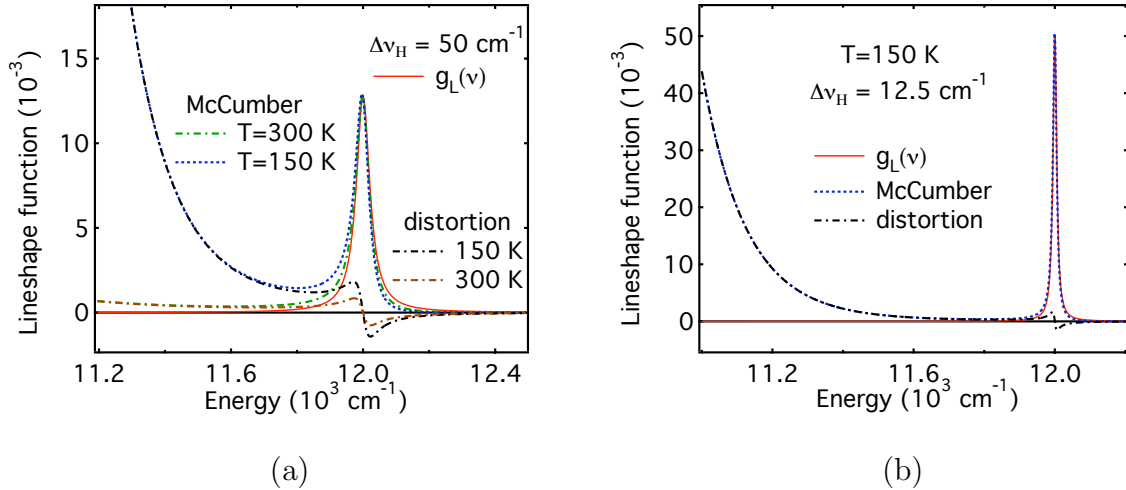


Figure 6.1: Distortion introduced by the McCumber formula on a single line homogeneously broadened: (a) 50 cm^{-1} ; (b) (a) 12.5 cm^{-1} . There is an overall rise of the calculated emission lineshape at the low energy side compared with the actual emission lineshape. The major distortion produced by the Lorentzian wings is observed outside the range of the transition, increasing exponentially away from the peak. For large homogeneous widths, the distortion within the spectral range also becomes significant. At 150 K, the homogeneous width is small (12.5 cm^{-1}), distorting insignificantly the shape within the transition width. However, it picks-up much faster at the low energy side.

relation, we define a distortion function $\delta_L(\lambda)$ as the difference between the calculated and measured curves. This function is also displayed in Fig.(6.1) (a), and we see that it is zero at the peak of the transition, has negative values at the higher energy side, is positive and increases exponentially at the lower energy side. It presents two critical points, a minimum and a maximum, and their relative amplitude with respect to the transition peak increases with the increase of the $\Delta\nu_H/k_B T$ factor.

The value of the homogeneous width, however, decreases almost quadratically with the temperature, so a typical width of 50 cm^{-1} at room temperature for rare earth transitions, becomes only 12.5 cm^{-1} at 150 K. The expected behavior for the predicted

lineshape in this case is shown in Fig.(6.1) (b), together with the distortion function. We see that the distortion is negligible for a spectral range of $\sim 500 \text{ cm}^{-1}$.

What is very important to note at this point, is that at lower temperature the distortion is negligible for a shorter range than at room temperature. This can be seen in Fig.(6.2), which shows the effect of the McCumber equation on the calculated lineshape

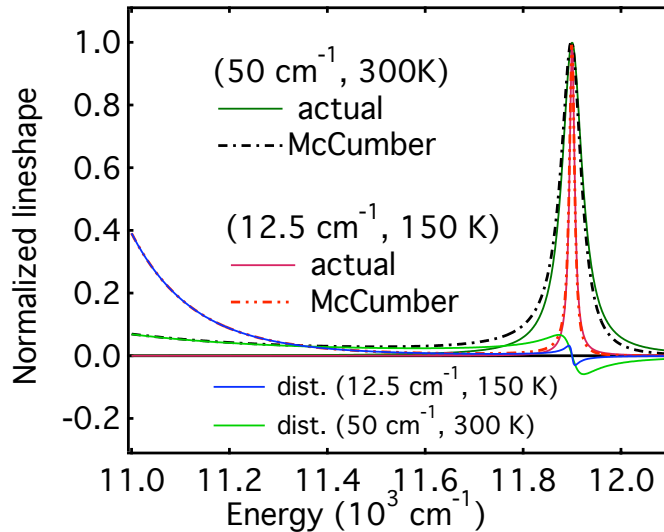


Figure 6.2: Comparison between the distortions introduced by the McCumber formula at 150 K and 300 K on a spectral line homogeneously broadened. The homogeneous width at 300 K was taken 50 cm^{-1} and quadratical dependence with the temperature was assumed. Within 200 cm^{-1} from the peak, the distortion is larger at room temperature, while 600 cm^{-1} at the low energy side of the peak, the low temperature spectrum starts getting more distorted.

in these two situations: $(50 \text{ cm}^{-1}, T = 300 \text{ K})$ and $(12.5 \text{ cm}^{-1}, T = 150 \text{ K})$. As the temperature is lowered, the spectral width decreases, and so does the factor $\Delta\nu_H/k_B T$. This produces smaller distortions at 150 K than at 300 K for frequencies within the spectral line (small range). As the distance from the transition peak increases, the distorting factor $\exp[(h\nu_0 - h\nu)/k_B T]$ (see eq.(3.58)) increases at much higher ratio, becoming more efficient in distorting the lineshape at the low energy side. Larger distortion at smaller distance from the peak are expected for larger homogeneous widths of the transition.

Inhomogeneous broadening

The inhomogeneous width is represented by a Gaussian lineshape function. The actual emission, absorption and McCumber emission lineshapes in this case are given by

$$\sigma_{em}^{actual}(\nu) = \sigma_{abs}^{actual}(\nu) = \sigma_0 \exp \left[-4 \ln 2 \left(\frac{\nu - \nu_0}{\Delta\nu_{IH}} \right)^2 \right] \quad (6.4)$$

$$\sigma_{em}^{McC}(\nu) = \sigma_0 \exp \left[-4 \ln 2 \left(\frac{\nu - \nu_0}{\Delta\nu_{IH}} \right)^2 \right] e^{h(\nu_0 - \nu)/k_B T} \quad (6.5)$$

where $\sigma_0 = (\sigma_0^*/\Delta\nu_{IH})\sqrt{4 \ln 2/\pi}$ is the amplitude of the actual Gaussian cross section, σ_0^* containing the units for the cross section. The McCumber transform of a Gaussian function is also Gaussian, with different amplitude and different peak frequency. The McCumber emission cross section given by Eq.(6.5) can be written as

$$\sigma_{em}^{McC}(\nu) = \sigma_0 \exp \left[\frac{1}{4 \ln 2} \left(\frac{h\Delta\nu_{IH}}{k_B T} \right)^2 \right] \exp \left[\frac{-4 \ln 2}{\Delta\nu_{IH}^2} \left(\nu - \nu_0 + \frac{1}{4 \ln 2} \frac{h^2 \Delta\nu_{IH}^2}{2 k_B T} \right)^2 \right] \quad (6.6)$$

The amplitude of the McCumber calculated peak is larger than the one of the actual peak, depending on the value of the inhomogeneous width $\Delta\nu_{IH}$.

The McCumber predicted lineshape for a Gaussian peak at 12000 cm^{-1} and width of 50 cm^{-1} is shown in Fig.(6.3) (a) at temperatures of 300 K and 150 K. At room temperature, the predicted curve is almost unnoticeable from the actual one, while at 150 K, the discrepancy becomes visible. Calculating the distortion function $\delta_G(\lambda)$, we can see this discrepancy in more detail and, as shown in the same figure, can be as large as 15% relative to the peak value. Actual and predicted lineshapes for inhomogeneous width of 100 cm^{-1} are shown in Fig.(6.3) (b) for 150 K and 300 K. The relative amount of distortion at 150 K with respect to the peak becomes as high as 33%, within less than half the value of the spectral width from the peak energy.

In conclusion, at low temperature ($\sim 150 \text{ K}$), the transition is predominantly inhomogeneously broadened, as the inhomogeneous width is invariant with the temperature.

McCumber theory introduces an overall rise in the calculated lineshape at the short energy side of the emission lineshape and a fall at the long energy side, and also a shift in the peak of the transition. The distortion caused by inhomogeneous broadening is found

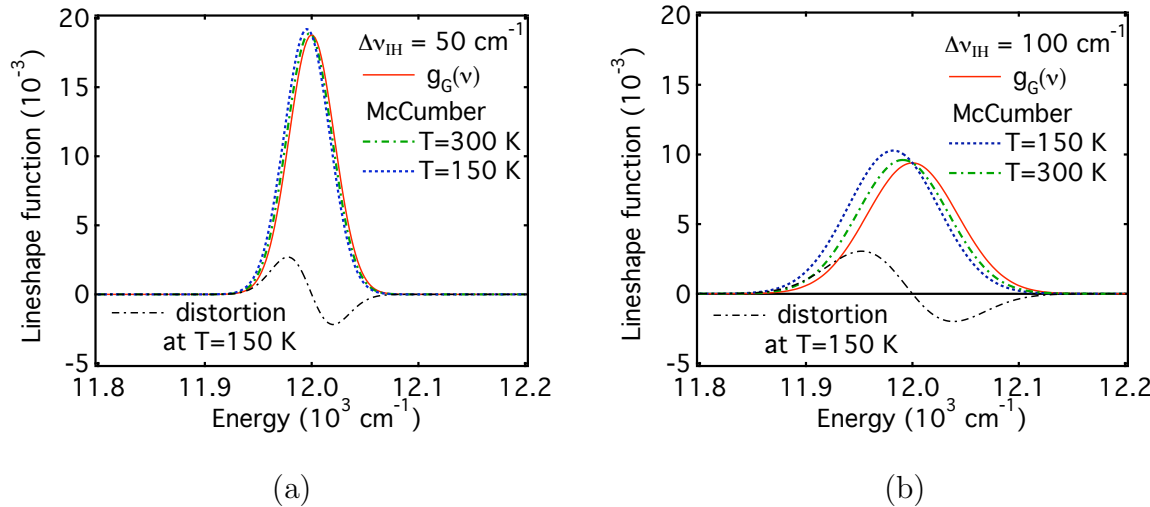


Figure 6.3: Distortion introduced by the McCumber formula at 150 K and 300 K on a single line inhomogeneously broadened: (a) 50 cm^{-1} ; (b) (a) 100 cm^{-1} . Besides the overall rise of the low energy side of the lineshape, we also notice a peak shift, and two critical points (minimum and maximum) in the distortion function.

mostly within the spectral range of the transition, while the one caused by homogeneous broadening is expected to be larger outside the spectral range.

6.1.2 Multiple peak distortion

The distortion caused by the McCumber theory at low temperature has been studied by investigating the shape of several multiple peak transitions homogeneously or inhomogeneously broadened at 150 K.

Homogeneous broadening

Fig.(6.4) shows the distortion introduced by the McCumber relation on a 3 peak homogeneously broadened line, with spectral width of 12.5 cm^{-1} (a), and 50 cm^{-1} (b) at 150

K. The emission peaks have equal amplitude and they are equally spaced by 100 cm^{-1} .

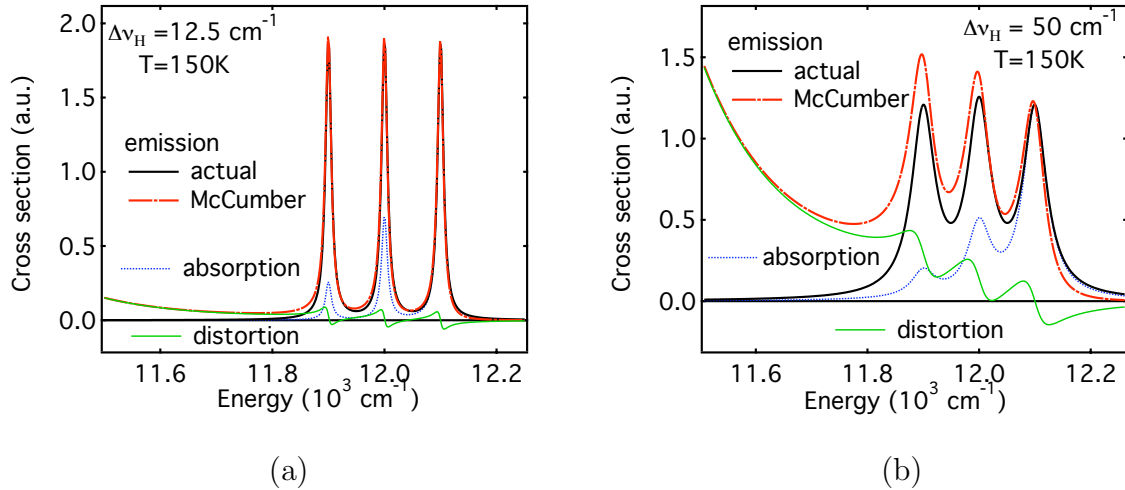


Figure 6.4: Distortion introduced by the McCumber formula at $T=150 \text{ K}$ on a multi-peaked spectral line inhomogeneously broadened: (a) 12.5 cm^{-1} ; (b) (a) 50 cm^{-1} . For narrow widths, the shape of the peaks is not affected within $\sim 500 \text{ cm}^{-1}$. For broad widths, the overall calculated shape is also distorted, due to the large overlap of the peaks and larger Lorentzian tails.

This results in a very sharply resolved structure for the 12.5 cm^{-1} width compared to the 50 cm^{-1} situation, where the tails of the individual peaks are overlapped. The actual spectral shape of the emission cross section can be written as

$$\sigma_{em}^s(E) = g_L^s(E - 11900) + g_L^s(E - 12000) + g_L^s(E - 12100) \quad (6.7)$$

where $g_L^s(E - E_{ij})$ is the energy dependent part of the Lorentzian function

$$g_L^s(E - E_{ij}) = \frac{1}{(E - E_{ij})^2 + (\Delta E_H/2)^2} \quad (6.8)$$

The spectral shape of the actual absorption cross section was obtained using the Boltzmann factor to determine the relative weighting of the three peaks, such as

$$\sigma_{abs}^s(E) = g_L^s(E - 11900) + g_L^s(E - 12000)e^{100/100} + g_L^s(E - 12100)e^{200/100} \quad (6.9)$$

where the numerator at the exponential represents energy spacing with respect to the lowest level (11900 cm^{-1}), and the denominator represents the value of $k_B T$ in cm^{-1}

at T=150 K. The emission spectrum was then normalized to the same value as the absorption peak at 12100 cm^{-1} . The McCumber emission cross section spectrum is calculated according to the McCumber relation from the absorption spectrum given by Eq.(6.9), at the effective energy of 12100 cm^{-1} , corresponding to the highest absorption peak¹.

The distortion for 12.5 cm^{-1} width is small and is similar to the one observed for a single peak. This is because the individual peaks are well separated and do not affect each other on short range. Within the spectral range, the distortion function presents small negative minima and positive maxima, while outside the range, has the exponential increase specific to the Lorentzian amplification at the low energy side of the line, and decays to zero at the high energy side. The distortion is expected to be small for $\sim 500\text{ cm}^{-1}$ interval from the highest energy peak.

In the case of wide overlapping transitions homogeneously broadened, (Fig.(6.4) (b)), the amplification of the short energy Lorentzian tail is larger and has a greater effect on the calculated lineshape of the other peaks in this region. As a consequence, the amplitude of the calculated peaks at the low energy side is higher than the actual value, and the distortion function has a sloped behavior across the spectral range of the multiple peak line. In this situation, only one minima has negative value, the curve containing the inflection points (where the curve changes concavity) of the distortion function is also sloped in the direction of amplification. If the calculated and actual emission curves are normalized to the value of the middle peak, the distortion curve will contain two negative minima at the high energy side.

¹Our treatment was carried only at the spectral level, and therefore the partition functions and absolute amplitudes of the individual peaks have been omitted.

Inhomogeneous broadening

To understand the effect of the McCumber formula on a multiple peak spectral line inhomogeneously broadened, we simulated different simple situations to include aspects like spectral overlapping, transition width, amplitude of the peaks and number of individual peaks. For one inhomogeneously broadened peak, the distortion produced by the McCumber formula is expected mostly within the range of the spectral line. This is an effect of the square-exponential decay to zero of the Gaussian function.

The distortion caused by the McCumber formula at $T = 150$ K on a spectral line consisting of 3 equal amplitude emission peaks, with inhomogeneous width equal to 50 cm^{-1} and spaced at 100 cm^{-1} from each other, is shown in Fig.(6.5) (a). The absorption spectrum is obtained in a similar fashion as for homogeneous broadening, relating the amplitudes of the three peaks by the Boltzmann factors. The three cross sections can

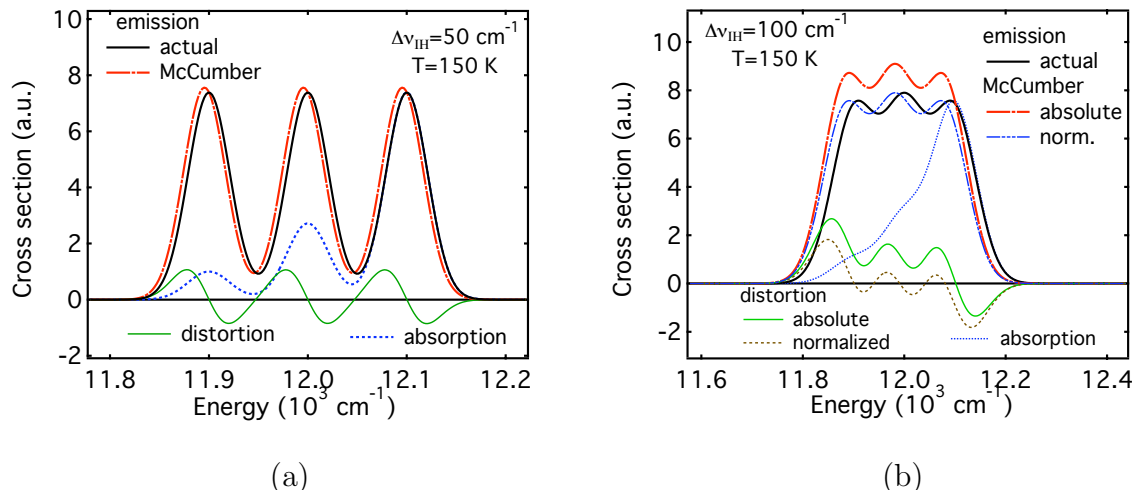


Figure 6.5: Distortion introduced by the McCumber formula at $T=150$ K on a multi-peaked spectral line inhomogeneously broadened: (a) 50 cm^{-1} ; (b) (a) 100 cm^{-1} . The distortion is localized within the transition range and, as long as the peaks do not overlap, the distortion corresponds to the one for single peak. For overlapping peaks, the positive and negative distortions in the region between two peaks partially compensate, resulting an overall less distorted line in the mid-region.

then be written as

$$\sigma_{em}^s(E) = g_G^s(E - 11900) + g_G^s(E - 12000) + g_G^s(E - 12100) \quad (6.10)$$

$$\sigma_{abs}^s(E) = g_G^s(E - 11900) + g_G^s(E - 12000)e^{100/100} + g_G^s(E - 12100)e^{200/100} \quad (6.11)$$

$$\sigma_{em}^{McC}(E) = \sigma_{abs}^s(E)e^{(12100-E)/k_B T} \quad (6.12)$$

where $g_G^s(E - E_{ij})$ is the energy dependent part of the Gaussian lineshape function given by

$$g_G^s(E - E_{ij}) = \exp \left[-4\ln(2) \left(\frac{E - E_{ij}}{\Delta E_{IH}} \right)^2 \right] \quad (6.13)$$

As for a single peak, the distortion is noticeable when visually comparing the calculated and the actual spectra. The pattern is the same as for the single peak: each individual peak is shifted toward the lower energy side, and has a larger amplitude. This difference is quantified by calculating the distortion function. This way we see that, as long as the peaks do not overlap, the behavior of the distortion function is the same as for a single peak, with sharper changes at the inflection points at the valleys between individual peaks. As the three emission peaks have equal amplitude and width, and are equally spaced, all the maxima of the distortion function are equal, and so all the minima.

Making the inhomogeneous width 100 cm^{-1} , we obtain a spectral line as in Fig.(6.5) (b). The McCumber predicted lineshape was calculated at the effective energy of 12100 cm^{-1} , at $T = 150 \text{ K}$. The actual emission and absorption lineshapes have been normalized to the same peak value.

We notice a larger increase in the calculated shape at the lower energy side of the 12100 cm^{-1} absorption peak, due to the larger width affecting amplitude of the McCumber spectra. Also the shift is larger than for the 50 cm^{-1} spectra. The distortion function presents antisymmetry with respect to the energy of the central peak, and a horizontal line of the inflection points. This becomes zero when the McCumber and

actual linefunctions are normalized to the same peak value. This is only the case for spectral line (emission in this case) consisting of individual peaks of equal amplitude and equal width. The amplitude of the intermediate peaks of the distortion function becomes smaller as the overlapping area of the peaks in the spectral line increases (introduces a "dephasing" factor which "destroys" the peaks of the distortion function).

Another situation of interest is when the emission line consists of peaks of 100

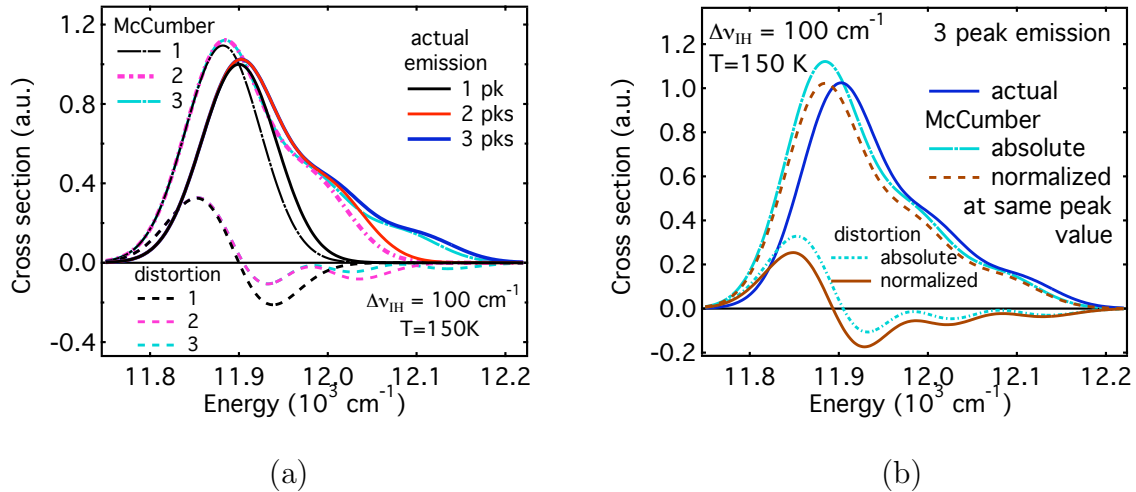


Figure 6.6: Distortion introduced by the McCumber formula at $T=150 \text{ K}$ on a multipaked spectral line consisting of inhomogeneously broadened peaks of different amplitudes: (a) Comparison of the distortions caused by 1, 2 and 3 peaks of decreasing amplitudes. Peaks that do not overlap do not affect eachother. The distortion at low energy side of the peak at 11900 cm^{-1} is the same in all three situations, since the wings of the second and third peaks do not reach this far. (b) Comparison between the McCumber and the actual emission spectra for a 3-peak line. When the calculated and actual emission spectra are normalized to the same peak value, the critical points of the distortion function also change.

cm^{-1} width, equally spaced at 100 cm^{-1} and amplitude decreasing with the energy. In this case, the effect of the high energy peaks on the McCumber lineshape is very small, due to the smaller overlapping areas of the Gaussian wings. Fig.(6.6) (a) shows the comparison of the McCumber lineshape with the actual shape, for 1, 2 and 3 emission

peaks with exponentially decreasing amplitudes². From this graph we see, indeed, that adding the second and the third peaks at the emission line produces insignificant changes of the distortion function at the short energy side of the highest peak, while increasingly attenuates its value at the side where the peaks are added. The situation corresponding to 3 peak transition is extracted in Fig.(6.6) (b), where we also show the distortion function corresponding to the difference between the "absolute" McCumber emission (calculated at the 11900 cm^{-1} absorption peak) and the actual emission normalized to the absorption peak. The oscillations in the distortion function become more attenuated as the number of peaks increases. This is a cumulative effect of the amplification with decaying exponential at the high energy side of the 11900 cm^{-1} and with a increasing exponential of the second and third peaks, at their low energy side. When the distortion is calculated between the emission peaks normalized to the same peak value, the line of the inflection points shows a degree of tilting, due to the asymmetry of the spectral line.

A tilt of this axis may also be expected for individual peaks with different linewidths, broader peaks producing larger distortion, even when they are somewhat smaller in amplitude. Real spectral lines consist of peaks with different widths, usually larger than the width of the peak (which represents the transition between the two lowest levels of the manifolds and is less affected by phonon induced relaxations). The distortion line is then expected to be sloped, in the direction of amplification.

This is indeed the case for our model of three emission peaks with the same amplitude and different spectral widths, as shown in Fig.(6.7). The actual emission, actual absorption and the McCumber calculated emission are given by

$$\begin{aligned}\sigma_{em}^s(E) = & \exp \left[-4\ln(2) \left(\frac{E - 11900}{150} \right)^2 \right] + \exp \left[-4\ln(2) \left(\frac{E - 12000}{100} \right)^2 \right] \\ & + \exp \left[-4\ln(2) \left(\frac{E - 12100}{75} \right)^2 \right]\end{aligned}\quad (6.14)$$

²They correspond to an absorption spectrum consisting of peaks of equal amplitudes.

$$\sigma_{abs}^s(E) = \exp \left[-4\ln(2) \left(\frac{E - 11900}{150} \right)^2 \right] + \exp \left[-4\ln(2) \left(\frac{E - 12000}{100} \right)^2 \right] e^{100/100} \quad (6.15)$$

$$+ \exp \left[-4\ln(2) \left(\frac{E - 12100}{75} \right)^2 \right] e^{200/100}$$

$$\sigma_{em}^{McC}(E) = \sigma_{abs}^s(E) e^{(12100-E)/k_B T} \quad (6.16)$$

The spectral distortion is more dramatic at the low energy side of the spectrum, due to the larger widths of the peaks at 11900 and 12000 cm^{-1} and the larger overlapping area

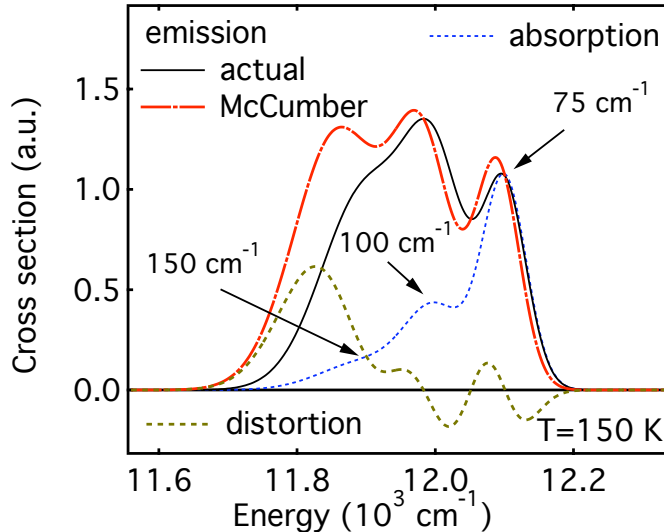


Figure 6.7: Distortion introduced by the McCumber formula at $T=150\text{ K}$ on a multipaked spectral line consisting of inhomogeneously broadened peaks width different spectral widths.

between these two peaks.

In conclusion, the specific distortion expected for our study is mosly the one corresponding to the Gaussian description as in Fig.(6.6) (a) and (b) and Fig.(6.7) for a multiple peak transition. The effect of the failing of the McCumber theory will be found mostly within the range of the spectral line, unlike for homogeneous broadening where strong distortion is expected away from the peak. However, for broad spectral lines ($\geq 500\text{ cm}^{-1}$) with typical homogeneous width of $\sim 50\text{ cm}^{-1}$ (at room temperature), a separate effect of the Lorentzian amplification is also expected, by observing an

increased slope in the distortion function. Both broadening processes introduce a shift in the peak of the transition and an overall rise in the calculated emission at the low energy side of the peak.

6.2 Experimental setup

Low temperature measurements are more complex and laborious, and they not only require the use of more specific equipment, but also a change in the experimental setup

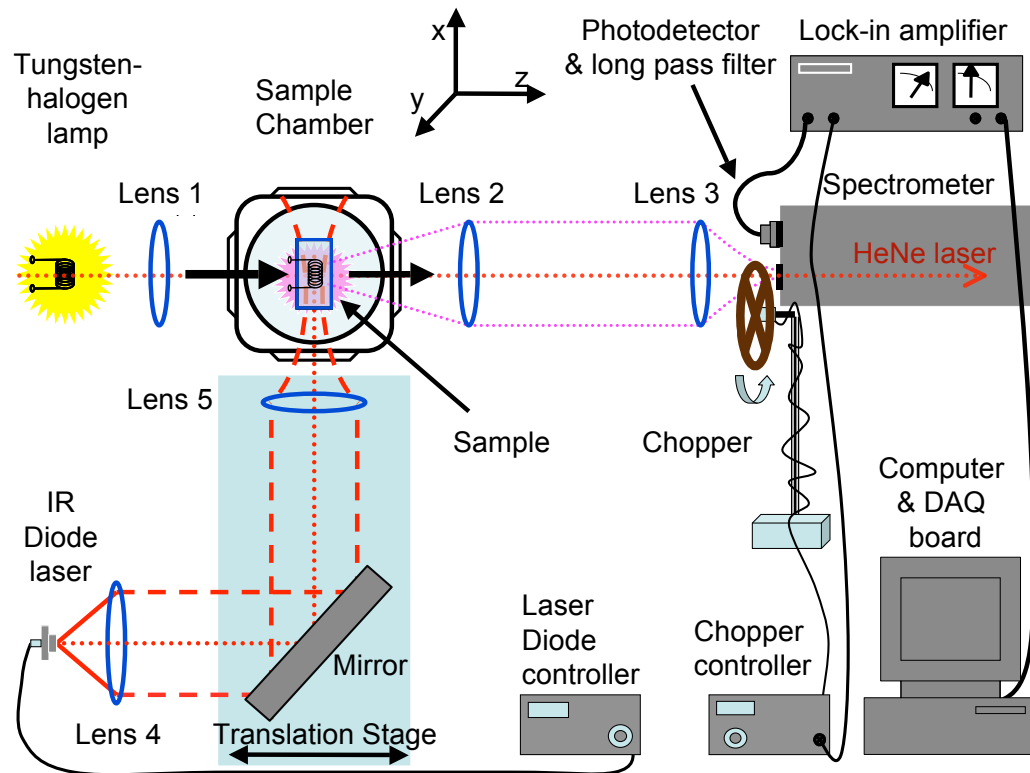


Figure 6.8: Experimental setup for low temperature measurements. The x-z plane is horizontal and the fluorescence and absorption axis are both in the horizontal plane.

and in the optical alignment compared to the one used for fluorescence and absorption measurements at room temperature. The experimental setup used is shown in Fig.(6.8).

The sample chamber was provided with three windows, which allows the fluorescence collection in a direction perpendicular to the direction of excitation, simultaneously with investigations of absorption along the optical axis of the monochromometer. We will refer to the $+x$ direction as the "fluorescence axis"³ and to the $+z$ axis as the "absorption axis". This arrangement is very convenient since both absorption and fluorescence measurements could be performed without making adjustments to the experimental setup, other than alternatively blocking the two beams.

For fluorescence measurements, the sample was pumped at 808 nm with the same diode laser as for room temperature experiments, described in section (4.3.1). The collimated laser beam has been directed toward the sample with a mirror placed at 45° with the horizontal axis of the laser beam. The beam was then focused on the sample with Lens 5, as shown in Fig.(6.8). To facilitate the fine adjustment needed for minimization of the fluorescence reabsorption, the mirror and the lens were placed on a translation stage. This allowed us to finely adjust the position of the IR laser beam on the sample with respect to the edge facing the collection system. The signal was recorded with the silicon photodetector of 1 cm^2 active area, amplified and filtered with the lock-in amplifier, digitized by the DAQ board, and recorded into files on the computer.

The alignment for absorption measurements was done using a HeNe laser along the optical axis of the monochromometer. The image of the filament was aligned to coincide with the focused laser beam on the sample.

The sample was cooled to temperatures as low as 130 K, by placing it in thermal contact with an U-shaped copper bar inserted in liquid nitrogen. The sample was supported on the bar by two pairs of aluminum connectors as shown in Fig.(6.9). The sample holder (copper bar) was perforated on a $\sim 5 \text{ mm}$ diameter, allowing absorption

³meaning actually the direction of excitation for fluorescence measurements

measurements in the direction perpendicular to the bar, also thermal contact across a large region of the sample. To reduce additional misalignment introduced by the refrac-

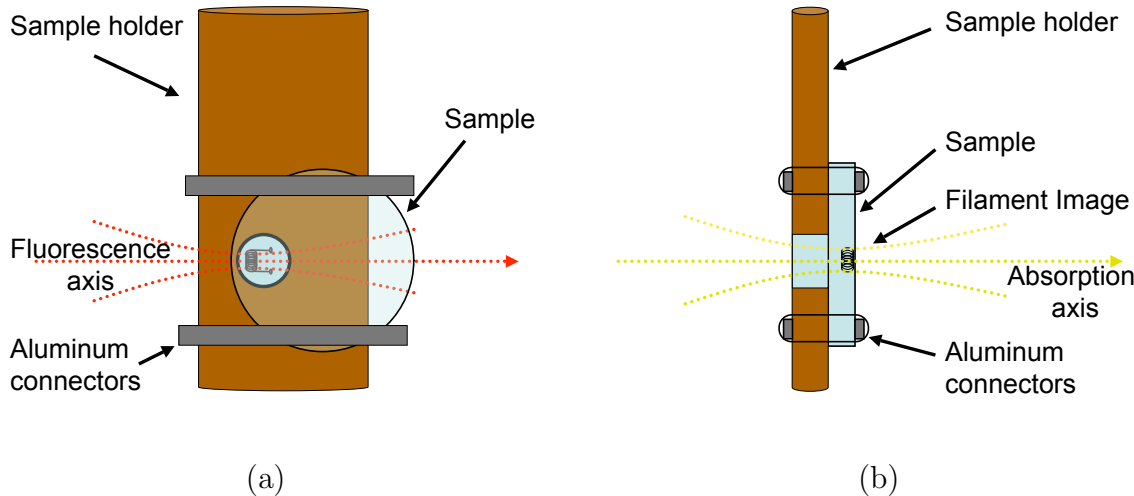


Figure 6.9: Sample view for the low temperature measurements: (a) front view (b) side view

tion of the IR laser beam at the incidence on the sample, we sledded the sample in the x direction, so the beam was focussed very close to the sample's edge.

The system used for cooling the sample is illustrated in Fig.(6.10). One end of the copper bar supports the sample, which is placed inside the sample chamber, while the other end is immersed in liquid nitrogen. To prevent major heat losses between the copper bar and the ambient atmosphere, this was surrounded by several layers of thermal insulation. The bar and the insulation along the arm supporting the sample make a reasonably tight fit with the upper opening of the sample chamber, and the experiments did not require any additional sealing.

As the sample cools down, the moisture from the atmosphere can condensate, producing ice on the surface of the sample, if this enters the sample chamber. To eliminate moisture from the chamber, we flushed with cooled nitrogen gas for about 30 minutes, before we started cooling the sample. The nitrogen gas was cooled by

circulating it through a copper tube inside a Dewar filled with liquid nitrogen. The use of cooled nitrogen gas helped keep the sample at low temperature, which otherwise would warm up by contact with the room temperature warm gas. The flow of the nitrogen gas

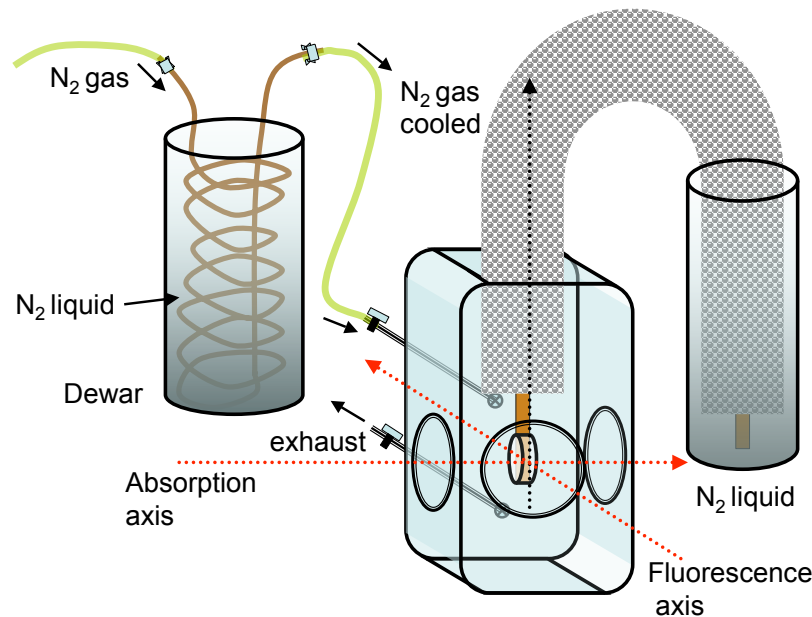


Figure 6.10: Illustration of the sample and the cooling system

could be adjusted from the two valves attached to the connection pipes of the sample chamber. To prevent the three windows from fogging with ice from the moisture in the room, we surrounded them with small heaters of nichrome wires, through which we ran a small current.

The temperature of the sample was measured with a copper-constantan thermocouple, attached to it. The temperature-voltage relationship for any pair of conductors is tabulated and, by reading the potential difference between the sample and a heat bath, we determine the temperature of the sample with respect to the bath. We measured the temperature with respect to a place on the breadboard located away from the

experimental setup, which has a temperature that is not affected by the experiments, but is constant during the measurements. The temperature of the bath (reference temperature) was calibrated at $20 \pm 1^\circ\text{C}$, by immersing the thermocouple into a mixture of water and ice and, separately, in liquid nitrogen.

6.3 Measurements and results

The low temperature measurements were more tedious and the optical alignment was more difficult than for the measurements performed at room temperature. Also, ice deposition due to condensation of different gases on the surface of the sample, made the measurements more susceptible to noisier signal, long time instabilities in the signal, and problems caused by strong light scattering. To reduce these effects, the following data were all taken within as short time interval as possible: fluorescence (lamp blocked), absorption (laser blocked), and in the beginning and at the end, the transmission spectra with the sample out of the beam and the blackbody correction for the fluorescence spectra were taken. The same collection system, detectors, and monochromator settings were used. Still, the moisture level varied during the day and produces different noise levels due to the OH absorption for the $\sim 800\text{-}1100$ nm range. Also, the attenuation with time of the transmission signal with the sample in place (small during one scan), due to more light scattering on the icy surface of the sample required the change in the reading scale between different scans. This adds difficulty to the determination of the absolute value of the absorption cross section and, as it is not the purpose of this study, only the spectral shape of the absorption spectra has been investigated.

The temperature of the sample was stable across one scan, within 3 K, and did not vary much between different scans (± 3 K). The effect of the temperature on the measured lineshape was carefully investigated, and found that within 10 K, the spectral

shape is almost invariant. Different temperatures could be obtained by varying the flow of the nitrogen gas in the chamber, or by adjusting the level of the liquid nitrogen, although this only provided a very limited control of the temperature.

6.3.1 Nd:fluorozirconate sample

The Nd:fluorozirconate sample is the same one that we used for the room temperature study. We investigated the validity of the McCumber theory at 132 K, 145 K and 156 K, by applying it to the transition between the $^4F_{3/2}$ and the $^4I_{9/2}$ levels, peaked at ~ 870 nm.

The spectral shape of the absorption and emission cross sections is affected by the temperature. As the homogeneous width decreases with lowering the temperature, the

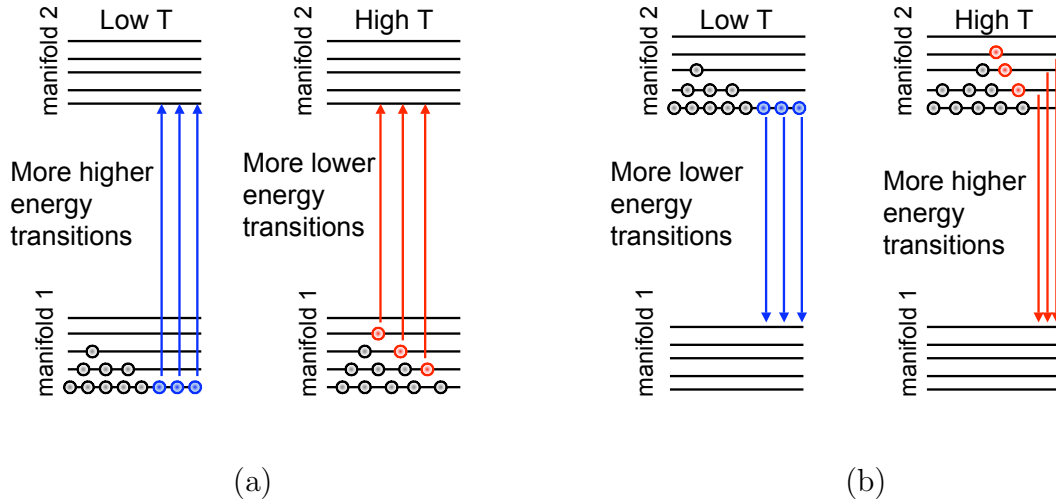


Figure 6.11: The effect of the temperature on the shape of the spectral line: (a) absorption transition; (b) emission transition

individual Stark peaks become sharper and higher in amplitude. The overall shape of the transition also changes as the temperature becomes lower. In order to explain this effect, we consider two Stark manifolds, and a number of ions Boltzmann distributed among them, as illustrated in Fig.(6.11). At low temperature, most ions will occupy the

lower Stark levels within the manifold. For absorption, more ions will execute transitions from these lower levels, contributing to an increase in the number of transitions at the high energy side of the spectrum. In fluorescence at low temperature, more atoms will execute transitions at the lower energy side of the line, while at high temperature, the spectrum will contain more higher energy transitions. This is observed experimentally, when the sample is cooled from room temperature to 130 K. Absorption and emission spectra corresponding to 293 K, 145 K and 130 K are shown in Fig.(6.12) (a) and (b). The change in shape is quite dramatic from 293 K to 145 K, and does not vary much from 145 K to 132 K (across ~ 13 K). Also, in the inset of Fig.(6.12) (b) we observe

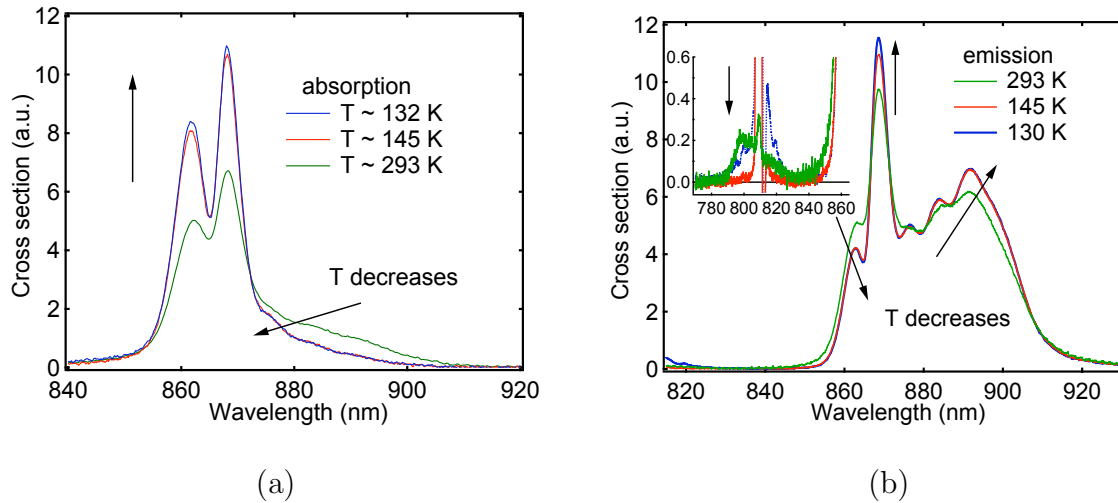


Figure 6.12: The effect of the temperature on the shape of the 870 nm transition in Nd:fluorozirconate: (a) absorption spectra; (b) emission spectra

that the 800 nm emission transition from the thermally populated levels ($^2H_{9/2}, ^4F_{5/2}$) disappears at 145 K, due to much lower population at this temperature. The weird feature around 808 nm for the 130 K spectrum is produced by very strong scattered light on the icy surface of the sample. At 145 K the sample was illuminated more inside, and some small reabsorption may be expected.

Absorption measurements have been performed in the manner explained in chap-

ter (5). The spectra obtained at ~ 132 K following the different steps are shown in Fig.(6.13) (a)-(d). Comparing the transmission spectra with the sample in and out the

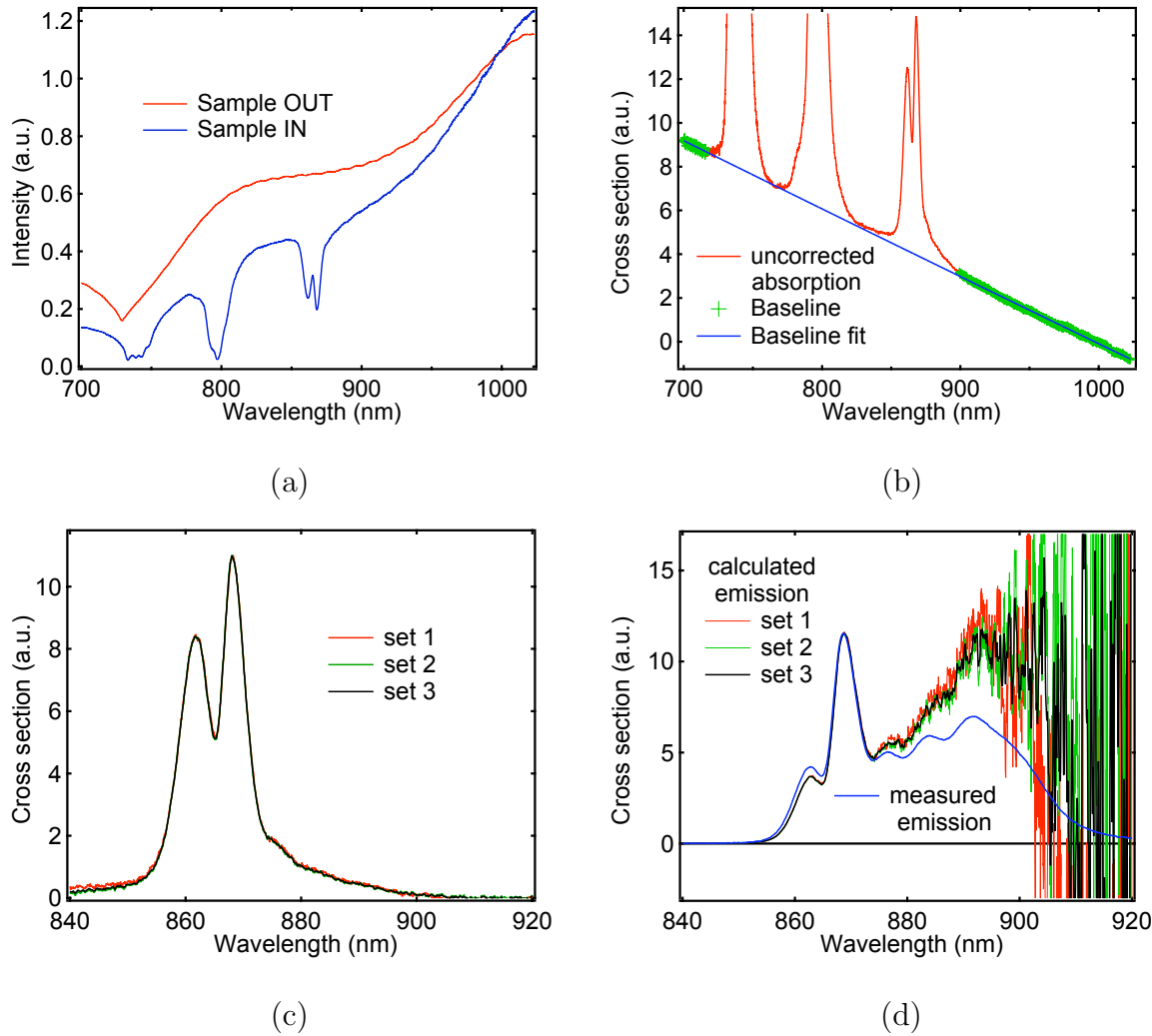


Figure 6.13: Determination of the calculated emission spectra with the McCumber formula at $T \sim 132$ K in Nd:fluorozirconate: (a) Transmission spectra with the sample In and Out the beam; (b) Uncorrected absorption cross section; (c) absorption cross section corrected for baseline for three different sets of data, and (d) calculated emission cross section corresponding to the three absorption data sets

beam (a), we determined the uncorrected absorption cross section (b), subtracted the baseline and calculated the emission cross section from the corrected absorption spectra with the McCumber relation. Fig.(6.13) (c) shows the corrected absorption cross

sections (in arbitrary units) for three different sets of data and baselines, and (d) shows the calculated emission cross section for these three sets.

The calculated spectra are terribly noisy, first of all because they are obtained from relatively noisy absorption spectra (due to problems caused by ice, like light scattering and lower chance to average in the exactly same conditions), but mostly because of the very large amplification produced by the $\exp(h\nu/k_B T)$ factor. The three different sets of data produce somewhat different calculated spectra. However, when compared with the measured emission spectrum, all three are systematically distorted, outside the noise range, or uncertainty due to baseline subtraction. What we observe in this figure, is a break down of the McCumber theory at low temperature, in the manner anticipated earlier in this chapter for simple simulated systems. The shorter wavelength side of the calculated emission spectrum is produced by the amplification with a decaying exponential, resulting in a lower calculated lineshape, while the longer wavelength side is obtained by the amplification with an increasing exponential, resulting in a calculated spectrum significantly exceeding the measured one.

The baseline fit has indeed a great effect in determining the long wavelength side of the calculated emission shape and, as we saw from room temperature studies, emission data are more reliable in reconstructing the correct absorption spectra. These absorption measurements, however, presented a less complicated baseline, as seen from Fig.(6.13) (b), which gave consistent results for all three sets of measurements used, and different sample out spectra.

We pursued our further investigations by performing systematic fluorescence measurements and comparing the calculated absorption spectra obtained with the McCumber formula, with the absorption spectra measured earlier.

A number of fluorescence spectra have been recorded at ~ 132 K, for sample illuminations at slightly different distances from the edge facing the entrance slit of the

monochromometer. Reabsorption and light scattering are very critical for our wavelength range of interest. At the very edge, strong scattering produces addition features at ~ 808 nm (as seen in Fig.(6.12) (b)), the side that is amplified by the McCumber formula. Scattering becomes more problematic as the temperature decreases. Reabsorption affects the emission peaks at very short distance from the edge, since the absorption coefficient at the peaks increases in amplitude as a consequence of a lower temperature.

The calculated and measured spectra at ~ 132 K are compared in Fig.(6.14), both for absorption (a) and emission (b). The calculated lineshape is strongly distorted in

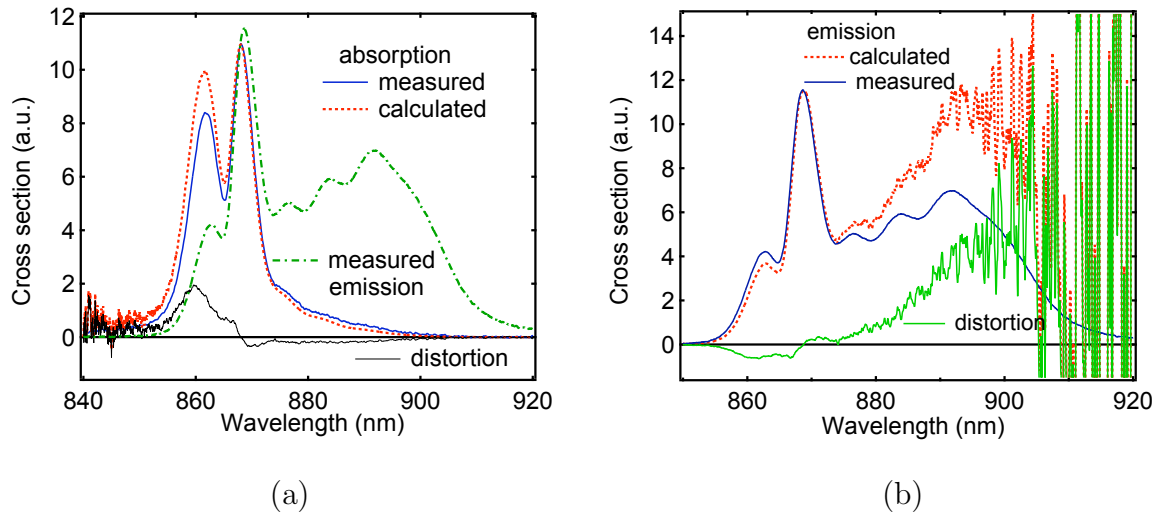


Figure 6.14: Comparison between the measured and the McCumber calculated cross section spectra at $T \sim 132$ K in Nd:fluorozirconate: (a) absorption; (b) emission

both representations, in absorption the short wavelength side is more amplified and long wavelength side is less amplified, while in emission the reverse situation is obtained. The good signal-to-noise ratio for the fluorescence measurements provides a better quality spectra for the calculated absorption, as compared to the calculated emission spectra for which the very large noise makes any estimation above 900 nm meaningless.

The distortion function is also represented in the above figures. It follows the same pattern as predicted in Fig.(6.3), only sloped and multifeatured, due to the multipeak

profile of the spectrum. The distortion is in the expected direction in both representations.

The same trend is observed in Fig.(6.15) when comparing the calculated and measured spectra for emission and absorption at 145 K, with less amplified distortion in both sides compared to the 132 K spectra. Some reabsorption at this temperature can

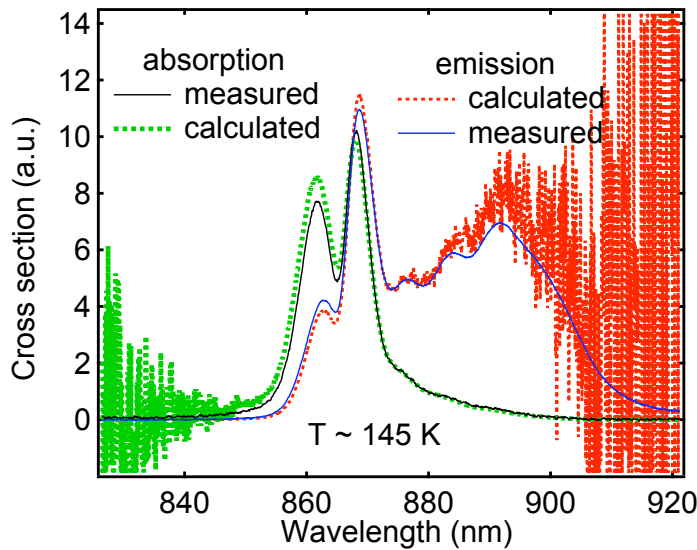


Figure 6.15: Distortion introduced by the McCumber formula on the calculated spectra at $T \sim 145$ K in Nd:fluorozirconate. Comparison between the measured and the McCumber calculated cross section spectra.

be noticed at the highest absorption peak.

To illustrate the effect of the temperature on the calculated cross section spectra, we represented the results obtained at 293 K, 145 K and 132 K superimposed on the same graph in Fig.(6.16) for absorption (a) and emission (b). The low temperature curves were scaled with respect to the room temperature spectra to cover almost the same area⁴, for a better display of the significant differences in the lineshape. We observed again the excellent agreement at room temperature. The distortion observed

⁴This is for convenience of display only, because the oscillator strength of the transition also varies with the temperature.

at 145 K and 132 K is produced mainly by the inhomogeneous width, and increases as the temperature becomes lower. From these spectra (more reliable when comparing

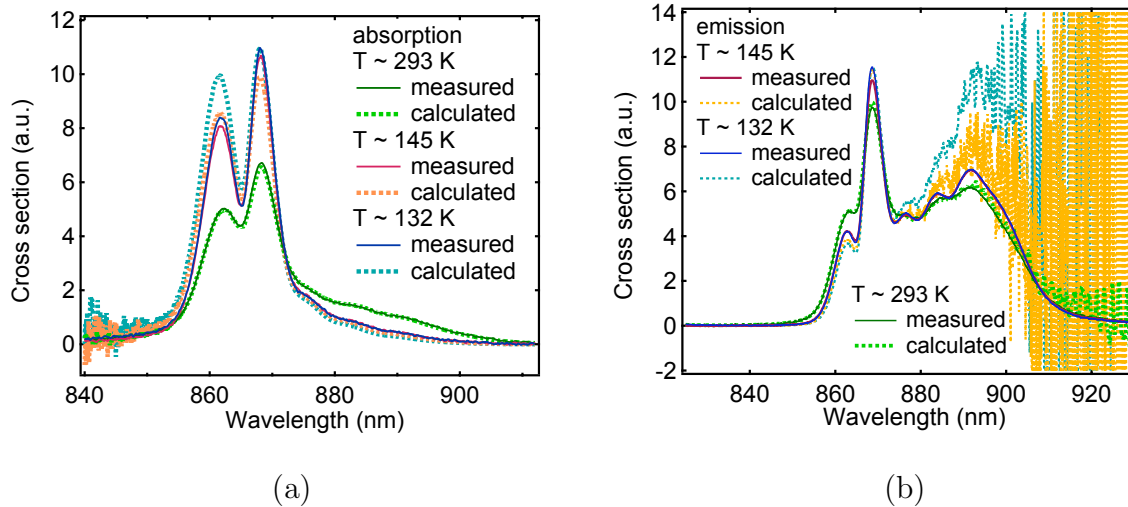


Figure 6.16: Distortion introduced by the McCumber formula on the calculated spectra at different temperatures in Nd:fluorozirconate. Comparison between the measured and the McCumber calculated cross section spectra: (a) absorption; (b) emission

absorption cross sections), we see that the significant distortion is within the spectral range of the transition, decaying to zero shortly outside the range. However, Lorentzian wings of large homogeneous widths can produce amplifications well outside the transition range even at low temperature.

6.3.2 Nd:silicate sample

We also investigated the $^4F_{3/2} \leftrightarrow ^4I_{9/2}$ transition in Nd:silicate sample at 156 K, 145 K and 136 K. This sample presented a less stable behavior when cooled, and not many data at the exactly same temperature for absorption and emission could be obtained. This results in a poorer signal-to-noise ratio for the measured spectra, and therefore a larger noise for calculated cross section.

Two potentially problematic aspects are discussed in this section: the effect of

the baseline subtraction and the effect of uncertainties in temperature. The temperature along a scan was constant within 3 K, as measured by the thermocouple placed on the sample. As shown earlier, the measured absorption and emission spectra vary insignificantly within 10 K, and they are constant for a 3 K variation. However, uncertainties in temperature may produce additional distortion in the calculated spectra, when improperly used. Fig.(6.17) (a) shows an absorption spectra measured at 141 K and several emission cross section spectra calculated at 141 ± 4 K. We see that different

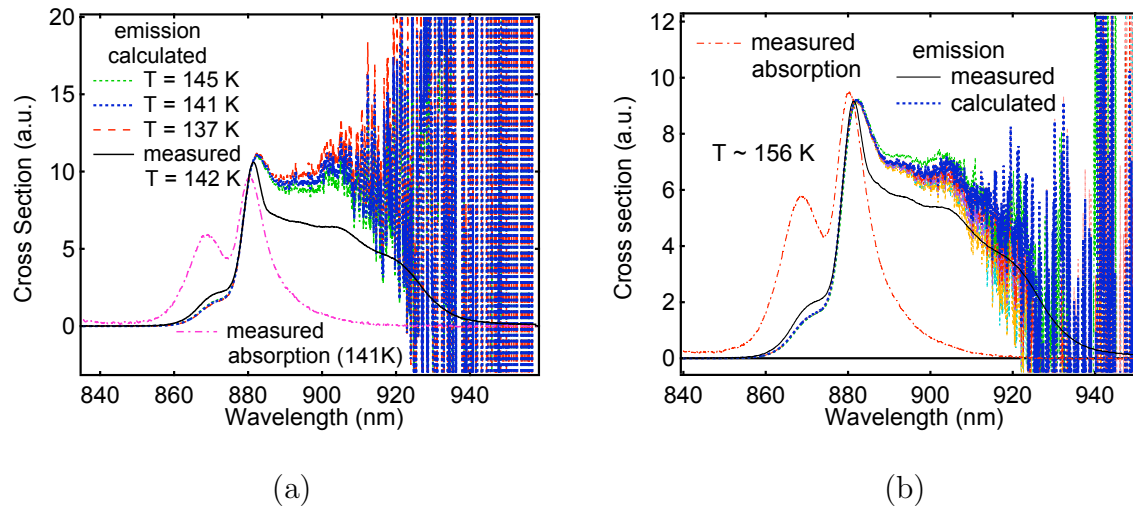


Figure 6.17: Effect of uncertainties in the temperature (a) (at $T \sim 142$ K) and baseline subtraction (b) (at $T \sim 156$ K)) on the calculated spectra in Nd:silicate

temperatures from 137 K to 145 K produce different calculated emission spectra, but they all are far away from the measured spectrum.

The level of uncertainty introduced by the selection of the baseline fit is shown in Fig.(6.17) (b) for a number of background fit curves of the absorption cross section measured at ~ 156 K. The calculated emission cross sections are again distorted from the measured spectrum in all situations for wavelengths below 920 nm, where the spectra are more reliable from noise and baseline considerations.

Both the above graphs show again a systematic distortion of the calculated spectra

compared to the measured ones, distortion specific to the McCumber relation applied to inhomogeneously broadened transitions that are broad compared with $k_B T$.

More absorption spectra were available at 156 K, providing a better signal-to-noise of the acquired spectra. The results are shown in Fig.(6.18) (a) for absorption and (b) for emission cross section comparison. We observe the same discrepancy between

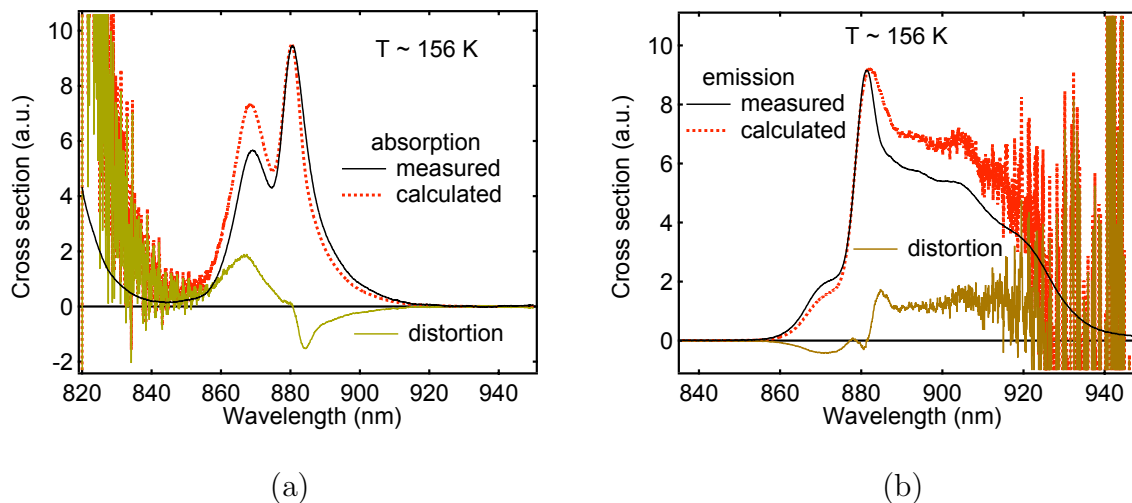


Figure 6.18: Distortion introduced by the McCumber formula on the calculated spectra at $T \sim 156$ K in Nd:silicate: (a) absorption; (b) emission

the calculated and measured spectra, in the direction expected from earlier theoretical predictions. The graphs also show the distortion function, which presents the anticipated behavior for a large spectral width. The exponential increase below 840 nm may be caused by the Lorentzian wings of the homogeneous broadening. Also, a pair of critical points can be distinguished for each of the two highest peaks.

At 143 K and 136 K we obtain similar results (Fig.(6.19) (a) and (b)), less reliable for the 136 K data for wavelengths above 910 nm, due to the rapid fall-off of emission with wavelength, along with a less fortunate baseline selection and strong amplification of a noisy and extremely low absorption signal above this wavelength.

From this study we can conclude that the distortion observed in calculated cross

section spectra for both samples at different low temperatures is mainly caused by the inhomogeneous spectral width. It represents a break down of the McCumber theory at

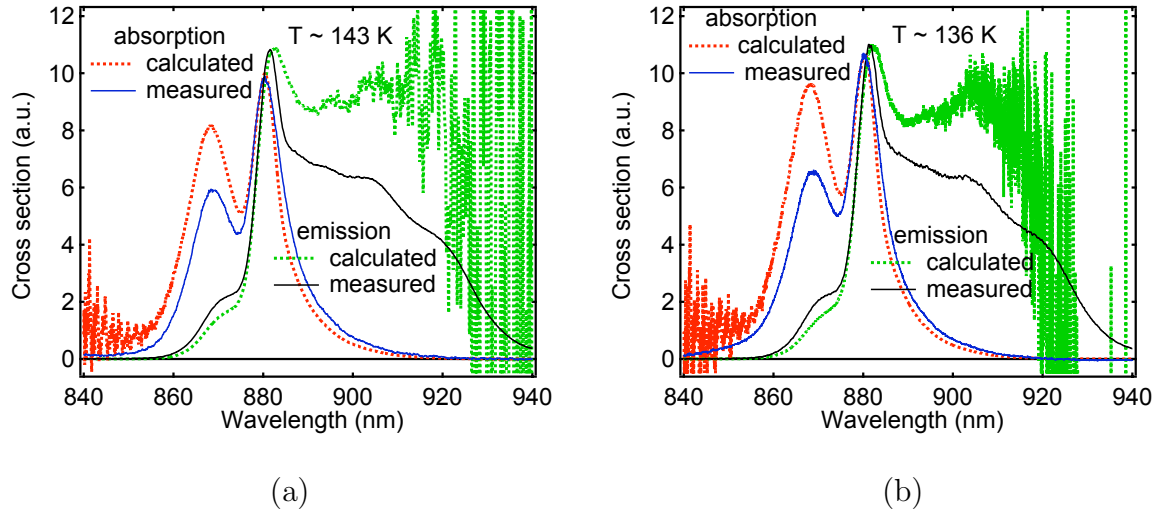


Figure 6.19: Comparison between the calculated and the measured spectra at $T \sim 143$ K (a) and $T \sim 136$ K (b) in Nd:silicate

sufficiently low temperature, where the inhomogeneous width cannot be neglected with respect to the value of $k_B T$. Although the calculated emission spectra are noisy, we can still conclude that in both absorption and emission representations the distortion is consistent with the trend expected for this type of broadening.

A few things, however, are not explicable yet, regarding the behavior of the calculated spectra for the Nd:silicate sample: the peak of the calculated emission is somewhat wider than the one measured from fluorescence. Also in absorption, the highest peak calculated from fluorescence is overall narrower than the measured absorption one. This may be due to site selection in the inhomogeneously broadened line. This would also be the case if the local temperature of the sample under laser excitation is lower than under broadband excitation with the lamp. This is very unlikely however, and why this would happen for this particular sample, is not yet understood.

6.4 Quantitative analysis

If we further explore the McCumber formula, we can obtain very useful information about the homogeneous and inhomogeneous linewidths of different transitions in different samples. From simple measurements of the peak shifts of the calculated spectra with respect to the measured ones, from locating the position of the critical points of the distortion function, or from more complex modeling of the multipeak lineshape based on knowledge of the individual oscillator strengths we can determine the width of the transition.

6.4.1 Exploring the peak shift

A. Homogeneous broadening

Homogeneous broadening is described by a Lorentzian lineshape function $g_L(\nu - \nu_0)$ displayed in Fig.(6.1) (a) and (b) for different values of the FWHM. The expression of $g_L(\nu - \nu_0)$ is given by Eq.(2.42), which for convenience we rewrite below

$$g_L(\nu - \nu_0) = \frac{1}{2\pi} \frac{\Delta\nu_H}{(\nu - \nu_0)^2 + (\Delta\nu_H/2)^2} \quad (6.17)$$

where ν_0 is the center frequency and $\Delta\nu_H$ is the full width at half maximum (FWHM) of the transition. For a single transition between two individual Stark levels, the McCumber relation predicts an emission cross section given by

$$\sigma_{ji}^{McC}(\nu) = \sigma_{ji}^{actual}(\nu) e^{-h(\nu - \nu_{ij})/k_B T} = \sigma_{0ji} g_0(\nu - \nu_{ij}) e^{-h(\nu - \nu_{ij})/k_B T} \quad (6.18)$$

where $g_0(\nu - \nu_{ij})$ is the lineshape function normalized to unity at the peak. The McCumber cross section will pose a peak at the frequency ν_p for which $d\sigma_{em}^{McC}(\nu)/d\nu = 0$. Pursuing simple derivations, the homogeneous width ΔE_H will be determined by

$$\Delta E_H^2 = 4(-2k_B T \cdot \Delta E_{meas} - \Delta E_{meas}^2) \quad (6.19)$$

where $\Delta E_{meas} = h(\nu_p - \nu_0)$ is the energy shift in the peak of the McCumber curve with respect to the position $h\nu_0$ of the actual (measured) curve. For the curves plotted in Fig.(6.1) (b) the peak shift is 3 cm^{-1} , at 150 K, resulting in a value of the homogeneous width of 48.6 cm^{-1} , very close to the 50 cm^{-1} value used in plotting the graph. Also, at 300 K, the measured peak shift is $\sim 1.5\text{ cm}^{-1}$, determining a width of 49 cm^{-1} . This method is impractical at room temperature, since it relies on measurements of peak shifts of only few cm^{-1} , but should work very well at high temperatures.

B. Inhomogeneous broadening

Inhomogeneous broadening is described by the Gaussian lineshape function $g_G(\nu - \nu_0)$ given by Eq.(6.20), rewritten as

$$g_G(\nu - \nu_0) = \frac{1}{\Delta\nu_{IH}} \sqrt{\frac{4 \ln 2}{\pi}} \exp \left[-4 \ln 2 \left(\frac{\nu - \nu_0}{\Delta\nu_{IH}} \right)^2 \right] \quad (6.20)$$

Using this in Eq.(6.18) and requiring the first derivative of the McCumber cross section be zero at peak value, we obtain the following expression for the inhomogeneous width ΔE_{IH}^2

$$\Delta E_{IH}^2 = (-8 \ln 2) k_B T \cdot \Delta E_{meas} \quad (6.21)$$

For the situations plotted in Fig.(6.3), the peak shift is 18 cm^{-1} at 150 K and 9 cm^{-1} at 300 K, both determining a width equal to 99.9 cm^{-1} , for the 100 cm^{-1} value used in plotting the graphs.

This method should give good results for low temperature measurements, since the peak shift of the Gaussian function is noticeably larger than the one corresponding to the Lorentzian (which has much sharper peak).

This method of measuring the peak shift should work better than observing the wings of the transition, since it uses the part of the spectrum that is least affected by noise, unlike at the wings where the noise is amplified as well.

The exact expressions derived above are only valid for single peaked transitions, and more useful for determining inhomogeneous widths. In the case of multiple peaks of different widths, the different peaks each affect each other in the McCumber cross section, if the spacing between them is less than their inhomogeneous width.

Using this method for the emission spectra of Nd in silicate and fluorozirconate glass, we determine a value of the inhomogeneous width of $76 \pm 11 \text{ cm}^{-1}$ in silicate glass and $38 \pm 14 \text{ cm}^{-1}$ in fluorozirconate glass. The error bars are determined by the selection of the location of the peak and the values obtained for different temperatures.

6.4.2 Exploring the critical points of the distortion function

While the separation between the McCumber and the actual peaks is not always measurable, due to very small shifts, especially for the Lorentzian function, the critical points (minima and maxima) observed very unambiguously in the distortion function $\delta(\nu) = \sigma_{em}^{McC}(\nu) - \sigma_{em}^{actual}(\nu)$ are well separated, and contain more valuable information regarding the spectral width. Requiring the first derivative of the distortion function be zero at critical points for each lineshape type, we determine the homogeneous (HW) and inhomogeneous (IW) widths as

$$\left(\frac{\Delta\nu_H}{2}\right)^2 = 2(\nu_p - \nu_0)\frac{k_B T}{h}(e^{h(\nu_p - \nu_0)/k_B T} - 1) - (\nu_p - \nu_0)^2 \quad (6.22)$$

and

$$(\Delta\nu_{IH})^2 = 8\ln 2(\nu_p - \nu_0)\frac{k_B T}{h}(e^{h(\nu_p - \nu_0)/k_B T} - 1) \quad (6.23)$$

These are exact relations that allow the determination of the HW and IW by measuring the location of the maxima and minima of the distortion function with respect to the position of the measured peak. Expanding in Taylor series we can simplify the above relations by keeping a reduced number of terms in the summation, according to the value of the $h(\nu_p - \nu_0)/k_B T$. As the critical points are located within half the spectral width

distance from the measured peak, the value of $h(\nu_p - \nu_0)/k_B T$ cannot be very large, and only few terms can be kept. The HW and IW can be written as

$$\left(\frac{\Delta\nu_H}{2}\right)^2 = (\nu_p - \nu_0)^2 \left\{ 1 + \frac{h(\nu_p - \nu_0)}{k_B T} + \frac{1}{3} \left[\frac{h(\nu_p - \nu_0)}{k_B T} \right]^2 + \dots + \frac{2}{n!} \left[\frac{h(\nu_p - \nu_0)}{k_B T} \right]^{n-1} \right\} \quad (6.24)$$

and

$$(\Delta\nu_{IH})^2 = 8 \ln 2 (\nu_p - \nu_0)^2 \left\{ 1 + \frac{1}{2!} \frac{h(\nu_p - \nu_0)}{k_B T} + \frac{1}{3!} \frac{h(\nu_p - \nu_0)^2}{(k_B T)^2} + \dots + \frac{1}{n!} \left[\frac{h(\nu_p - \nu_0)}{k_B T} \right]^{n-1} \right\} \quad (6.25)$$

where n gives the number of terms in the summation.

The position of the critical points of the distortion function changes with the number of peaks in the spectral line, each having different amplitude and width. Because of this, further modeling is required when these relations are applied to real multiple peak spectra. Also, the position of these critical points changes when the two cross sections (calculated, measured) are normalized to different values (the above equations, however, are exact for a single peak, where the emission and absorption cross sections are identical and the McCumber emission cross section is calculated at the peak energy).

Studying the discrepancies between the McCumber calculated function and the actual lineshape within the spectral line would, in principle provide information about the homogeneous and inhomogeneous widths of the transition peaks. This would be experimentally more useful than studying the amplification due to the Lorentzian tails at large distances from the peak, since in that region, the noise is also exponentially amplified, and is also more affected by the presence of other transitions or complications due to long wavelength range measurements. Also, this method should work for situations when one type of broadening is dominant (at low temperature for inhomogeneous broadening, high temperature for homogeneous broadening).

However, the location of the critical points is affected by the presence of the neighboring peaks, the scaling factors and the exact knowledge of ν_0 , and further modeling

of the above equations is required to pursue this study.

6.4.3 Modeling the spectral shape by fitting with a function describing the type of broadening

From our measured spectra at low temperature, we observed systematic distortions in the McCumber calculated spectra, in the direction estimated by earlier simple simulations, and of magnitude outside the range of uncertainty caused by temperature estimation, baseline subtraction, or fluorescence reabsorption and scattering problems. To gain more confidence about the results of our analysis, we modeled the emission and absorption spectra measured at 132 K in Nd:fluorozirconate sample by fitting with a superposition of Gaussian peaks, and compared the calculated spectra of the simulated profile with the spectra calculated from the real (experimental) data.

The simulation was performed by running a multipeak fitting routine incorporated in the data analysis software (IGOR, Wavemetrics, Inc.). Similar software procedures have been used by refs. [64] and [72] for measurements of spectral broadening in Yb^{3+} and Er^{3+} doped glasses. The set of peaks generated by the deconvolution of the spectra is not unique, and depends slightly on the initial conditions selected. This should not be an issue for our study, since our purpose is to simulate the overall spectral shape by a number of functions describing the type of broadening expected in our system⁵. Also, unresolved peaks generate different combinations in the selection of the individual peaks.

⁵The data analysis program also determines the width of the individual peaks, which can be used at some point to compare eventual values obtained from the failing of the McCumber theory. The spectral widths for the 868 nm peak does not vary much between different iterations ($\sim 55 \pm 5 \text{ cm}^{-1}$). Not all parameters that contribute to uncertainties in the determination of the Gaussian FWHM have been accounted.

Figure (6.20) (a) shows the deconvolution of the emission spectrum into 6 Gaussian profiles. The maximum number of transitions between the $^4F_{3/2}$ and the $^4I_{9/2}$ manifolds

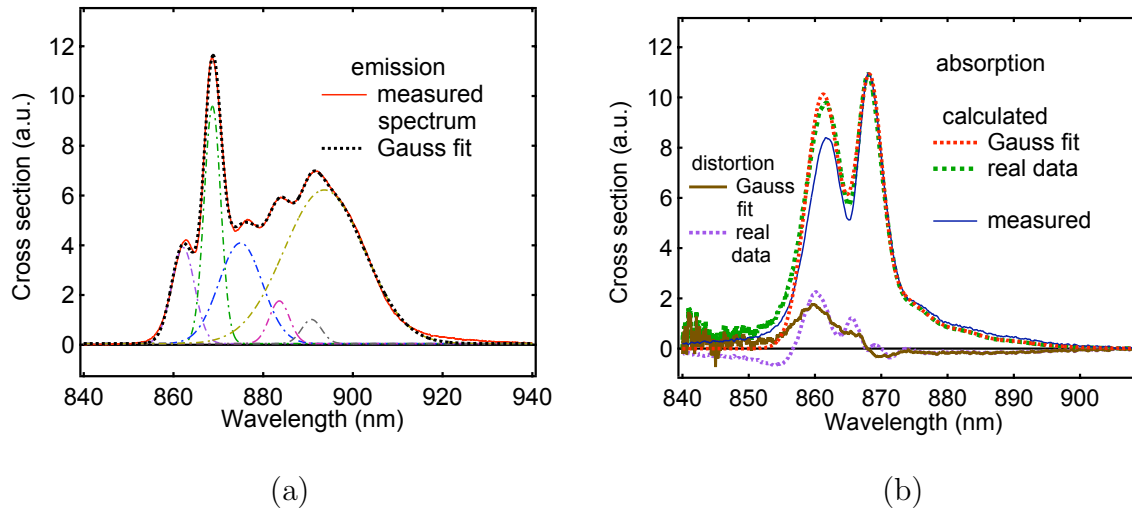


Figure 6.20: (a) Simulation of the emission spectrum of the 870 nm transition in Nd:fluorozirconate at T=132 K with a set of 6 Gaussian peaks. (b) Comparison of the calculated absorption cross section obtained from simulated spectrum with the absorption calculated from real data and with the measured absorption.

is 10, connecting each of the 2 individual levels of the higher $^4F_{3/2}$ manifold and the 5 levels of the ground $^4I_{9/2}$ manifold⁶. Less than 10 individual transitions are usually observed, especially at low temperature where the highest levels within each manifold have reduced population.

For emission, the two $(^4F_{3/2})_{1,2}$ levels are reasonably well populated. This explains the existence of the 862 nm emission peak at shorter wavelength side of the 868 nm transition peak, between the lowest levels within each manifold. Other transitions from this highest excited state have much lower intensity compared to the 862 nm transition, and they contribute mostly to the short wavelength side of the emission spectrum.

The McCumber calculated absorption from the simulated emission spectrum has been compared to the absorption cross section calculated from experimental data, and

⁶The levels of Nd^{3+} are Krammer degenerated.

also with the measured absorption cross section spectrum. The results are shown in Fig.(6.20) (b), together with the distortion function determined for the two calculated curves. The two calculated curves are very similar, except for wavelengths shorter than 855 nm, where the Gaussian fit cuts too sharply to zero, determining a calculated spectrum lower than the measured one. This is also observed in the distortion function, which reaches negative values within this range. Some very dimmed oscillations in the real data distortion function are observed in the region between the two peaks, and they are also seen in the distortion for the Gaussian fit (of somewhat larger amplitude due to the imperfect fit of the real spectrum). This can be the effect of the two Gaussian peaks of nearly equal amplitude, but different spectral width (the 862 nm peak is broader than the 868 nm peak). The effect of an eventual homogeneous broadening effect would be a continuation of the sloped distortion function outside the spectral range of the transition. As we can see, the distortion decays to zero outside the transition limits. We can conclude that the distortion observed in the real data is very similar to the one obtained by applying the McCumber relation to a set of 6 Gaussian functions that produce almost identical emission spectrum as the one measured experimentally.

We pursued our study by modeling the absorption spectrum acquired at 132 K of the same sample, with a set of Gaussian functions. The fitting process this time was more difficult, due to the lack of spectral resolution in the absorption spectrum at the side of interest (low energy side). Best fit was obtained for 8 Gaussian peaks, which can be actually justified by the much less population of the highest level of the ground state manifold $^4I_{9/2}$, at the temperature of 132 K. The fitting peaks, the overall Gauss fit and the measured absorption spectrum are shown in Fig.(6.21) (a) and the comparison between the two calculated emission spectra and the measured one is shown in Fig.(6.21) (b). We can see that the McCumber calculate emission spectrum of the simulated curve fits incredibly well the calculated emission spectrum from experimental

data. They both lie away from the measured emission spectrum. Due to the very large noise above 900 nm, the behavior of the distortion function cannot be observed outside the range of the transition. The large increase in the slope of the distortion function

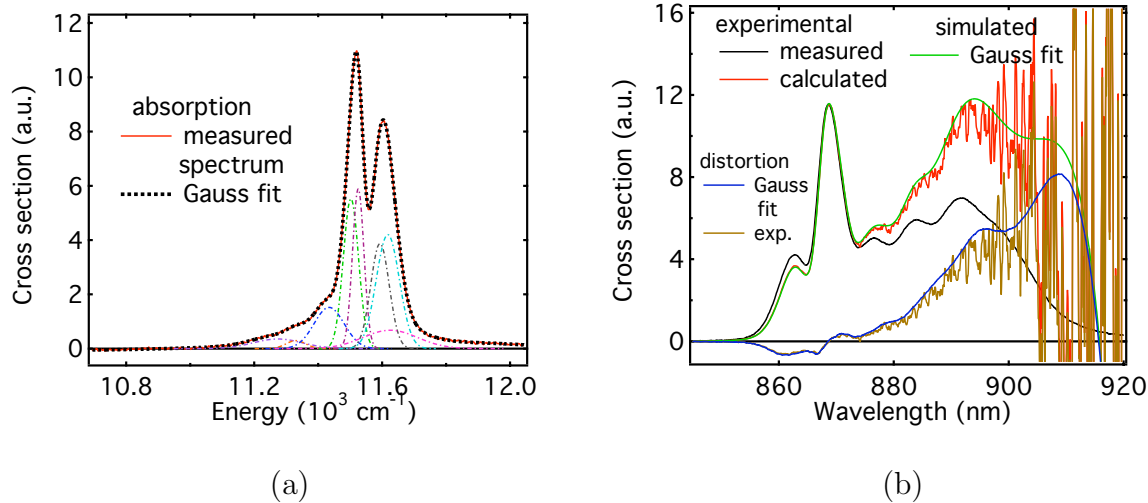


Figure 6.21: (a) Simulation of the absorption spectrum of the 870 nm transition in Nd:fluorozirconate at $T=132$ K with a set of 8 Gaussian peaks. (b) Comparison of the calculated emission cross section obtained from simulated spectrum with the emission calculated from real data and with the measured emission.

above the 868 nm peak may be caused by the increasingly larger inhomogeneous width of the peaks in this region. Also, above 910 nm it is also likely to observe the effect of the homogeneous broadening of 12.5 cm^{-1} width.

The emission spectrum has also been modeled by fitting it with a set of 6 Lorentzian functions, as shown in Fig.(6.22) (a), and the two calculated absorption spectra are compared with each other and with the measured spectrum in Fig.(6.22) (b). The simulated absorption is very similar to the measured one, however the wings of the Lorentzian peaks give a much larger curve for wavelengths below 860 nm. This produces a calculated absorption spectrum strongly distorted at the short wavelength side. The two distortion functions behave similarly within the spectral range of the line, the one corresponding to the Lorentzian curve presenting much sharper peaks, generated by the

imperfect fitting at the peaks of the emission line by the Lorentzian functions.

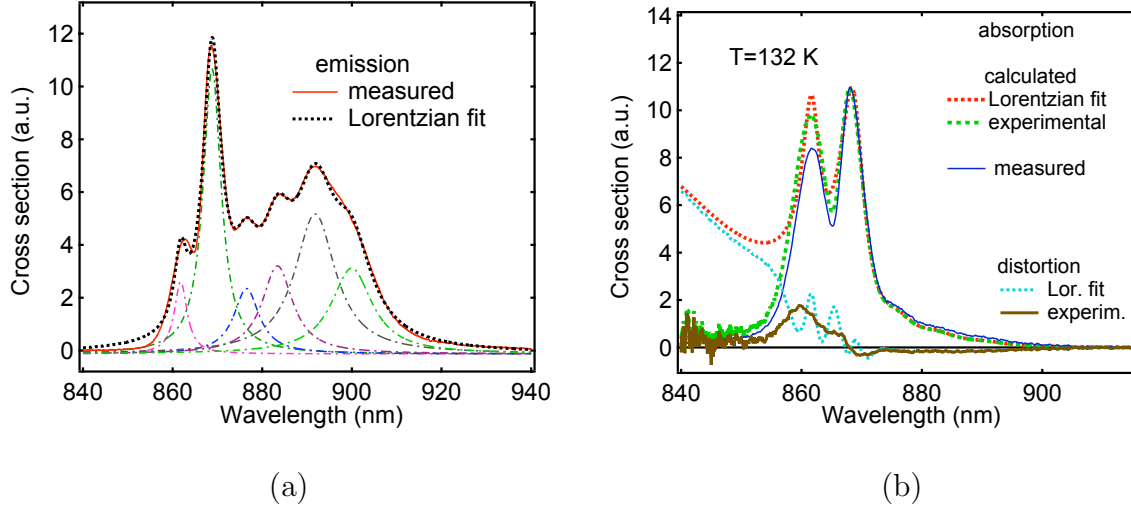


Figure 6.22: (a) Simulation of the emission spectrum of the 870 nm transition in Nd:fluorozirconate at $T=132$ K with a set of 6 Lorentzian peaks. (b) Comparison of the calculated absorption cross section obtained from simulated spectrum with the absorption calculated from real data and with the measured absorption.

The simulations were carried on for the absorption spectrum, which was fitted by 8 Lorentzian functions and the results are shown in Fig(6.23) (a) and (b). The same good agreement between the two calculated cross sections at the long wavelength side of the emission as for the Gaussian fit was also obtained in this case, which could be explained by the fact that the low energy side of the absorption spectrum can be modeled by different sets of functions, due to the very limited resolution and the low amplitude.

The distortion functions for the Gaussian and Lorentzian fit of the emission cross section have been extracted in Fig.(6.24) and we also show the distortion function for the measured data. The slope for the three distortion functions is the same in all three situations, within the range of the spectral line. Outside the line, the experimental distortion decays to zero, as expected for a Gaussian linefunction, the Gaussian distortion is negative at the short wavelength side, due to the underestimation of this side by the 6 Gaussian profiles, while the Lorentzian distortion function increases exponentially,

continuing to have the same slope as within the range of the transition. The attenuation

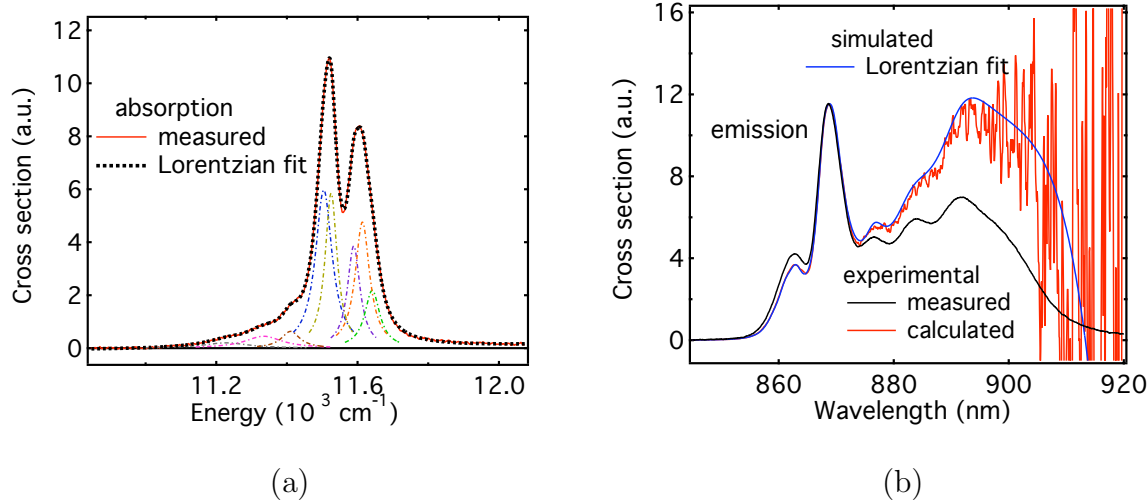


Figure 6.23: (a) Simulation of the absorption spectrum of the 870 nm transition in Nd:fluorozirconate at T=132 K with a set of 8 Lorentzian peaks. (b) Comparison of the calculated emission cross section obtained from simulated spectrum with the emission calculated from real data and with the measured emission.

of the oscillations in the experimental distortion function may be understood by the compensation effect of the McCumber distortion at the neighboring Gaussian peaks, while the slope can be produced by peaks of either increasing amplitude or increasing width. The effect of some homogeneous broadening is not completely excluded, although is not very likely.

To complete our study, we performed simulations on the room temperature results, to model the emission cross section of the same transition. As both types of spectral broadening are significant at room temperature, the expected lineshape of the individual peaks is described by neither Gaussian, nor Lorentzian functions, but by Voigt profiles. The measured emission spectrum was deconvoluted into 6 Voigt functions⁷, and the

⁷The Lorentzian width (FWHM) of the 868 nm peak determined from the analysis for this graph was 24 cm^{-1} , and the Gaussian width was 53 cm^{-1} . These are not necessarily the exact widths of the peak, but they give us a hint in estimating these extremely important unknowns for our study.

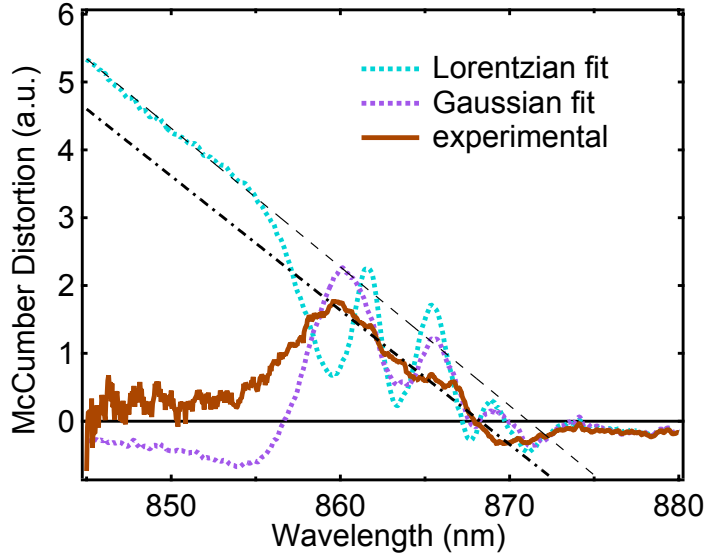


Figure 6.24: Comparison between the three distortion functions representing the difference between the calculated and measured absorption cross sections for Gaussian fit, Lorentzian fit and real data at 132 K in Nd:fluorozirconate.

overall Voigt fit, together with the measured emission and the 6 individual peaks are shown in Fig.(6.25) (a). The measured and the simulated emission spectra generate the McCumber calculated absorption spectra illustrated in Fig.(6.25) (b). On the same graph we also displayed the measured absorption cross section. The three curves are almost indistinguishable from each other, revealing once more the validity of the McCumber theory at room temperature, and also reinforcing the confidence of reliable results both for measured and for calculated spectra.

By applying the McCumber relation to simulated spectra consisting of known functions (Gaussian, Lorentzian, Voight), and comparing the calculated lineshape obtained for these simulations with the calculated lineshape obtained from our experimental data, we verified that the distortion observed for the experimental data is consistent with the expected McCumber distortion in each particular case. The emission spectrum described by 6 Gaussian peaks generate a much similar calculated absorption spectrum to the experimental situation than the Lorentzian fit, which presented too large tails in

the amplified region of the spectrum. The 8 Gaussian functions used to simulate the

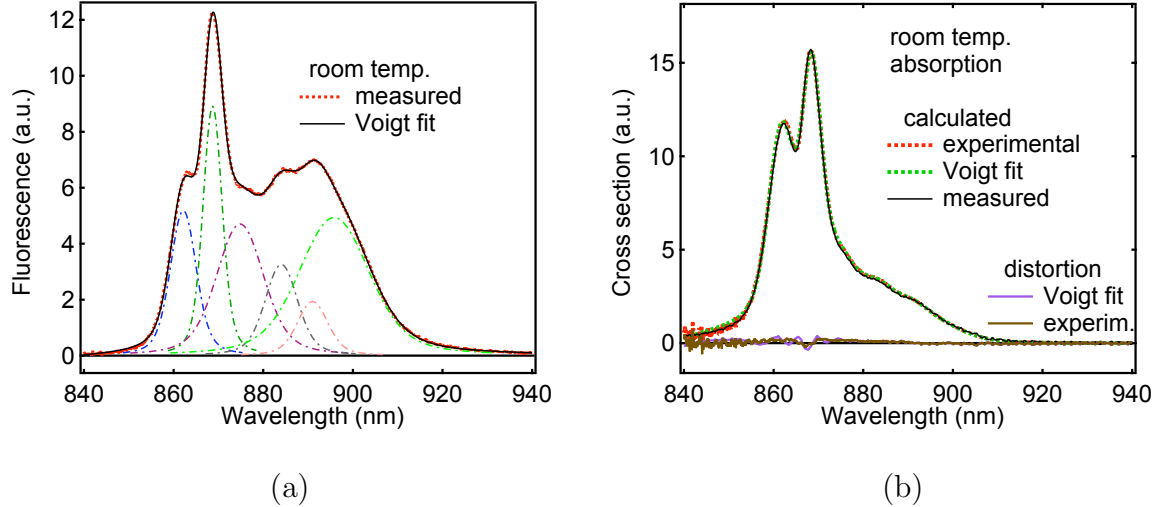


Figure 6.25: (a) Simulation of the emission spectrum of the 870 nm transition in Nd:fluorozirconate at T=132 K with a set of 6 Voigt peaks. (b) Comparison of the calculated absorption cross section obtained from simulated spectrum with the absorption calculated from real data and with the measured absorption.

absorption spectrum gave very similar results as the 8 Lorentzian peaks, which may be explained by the less resolved peaks at the low energy side of the absorption spectrum, which allows an increased number of fitting combinations. However, both emission cross sections calculated from the simulated spectra are in very good agreement with the McCumber emission cross section calculated from experimental data.

When the room temperature spectra were modeled by Voigt functions, the calculated spectra from simulated and measured cross sections are in excellent agreement with each other and with the measured spectra. This situation was again expected from our room temperature measurements, and previously predicted by numerical studies [47].

Chapter 7

Concluding remarks and Future directions

7.1 Concluding remarks

The validity of the McCumber theory has been experimentally tested, by applying it to ground state transitions of rare earth ions in fluoride and silicate glasses. The theory has been tested by comparing cross sections calculated using the McCumber relation with cross sections obtained from measurements. For a meaningful comparison, the absorption and fluorescence data have been taken with the same equipment, same instrumental settings (same width of the entrance and exit slits of the monochromator) and same settings for the collection system (collective lenses and position of the detectors).

At room temperature we performed fluorescence and absorption measurements Nd, Tm and Er -doped samples. We focused particularly on those aspects that lead to systematic errors, like background subtraction for measured absorption cross sections, proper calibration of the measured fluorescence signal and fluorescence reabsorption and light trapping for measured fluorescence.

Of all the possible sources of systematic error, the selection of the baseline fit for absorption turns out to have the largest effect on the McCumber calculated line-shape. Very small variations in the fitting line can create large deviations at the long wavelength side of the calculated emission spectra, due to exponential amplification of the McCumber equation. Determined by a combination between the geometry of the sample and its orientation with respect to the beam, the path of light inside the monochrometer and the spectral response of the detector, the baseline curve varies for each spectrum and must be individually subtracted for each situation, adding a degree of uncertainty each time, especially to spectra consisting of overlapping transitions, for which more fitting possibilities exist.

The effect of improper positioning of the filament was also studied. This is another source of error in determining the correct fluorescence signal, and it affects the comparison between the measured and calculated cross sections, especially for wide wavelength intervals, where the distortions of the measured signal become significant.

Fluorescence reabsorption in samples with high ion concentration affects the intensity of the light corresponding to a particular transition between two Stark manifolds, as well as its spectral shape. The most affected are the sharp, strong fluorescence peaks, that correspond to large values of the absorption coefficient. The effect of the reabsorption was studied for each transition, by varying the location of the focused beam on the sample with respect to the edge of the sample, and recording the fluorescence spectra for each position. Reabsorption was minimized by illuminating the sample very close to its edge. However, in thick samples (whose edges were hit by the focused beam) and in samples with rough edges, the sample could not be illuminated too close to the edge, due to light scattering and trapping that produced excitations in a large volume inside the sample.

When all these issues were properly accounted for, excellent agreement between

the calculated and the measured spectra was found in all cases. This is true even for the thermally coupled levels ($^2H_{9/2}$, $^4F_{5/2}$) and $^4F_{3/2}$ of Nd, which are spread along a $\sim 2000\text{ cm}^{-1}$ interval, much larger than the spectral width of a Stark manifold. For Tm, the agreement was good at two different pump wavelengths, within the noise level.

Very good agreement was also found for the wide 1530 nm transition of Er in fluorozirconate glass and especially in silicate glass, which is probably the most investigated in the literature, and also the most controversial in terms of applying the McCumber theory. Some studies [48] suggested that the McCumber theory should be avoided when predicting cross sections of the wide transitions of rare earths in amorphous hosts, based on the low statistical accuracy obtained by investigating a number of published spectra of Er-doped silica based samples, and also based on theoretical predictions from modeled spectra. A literature review (that reported the instruments used in each case) showed that in the majority of studies ([35], [39], [43]-[45]), different experimental setups and different instruments were used for measuring the emission and absorption spectra. Some results showed reasonably good agreement, while others presented distortions of various degree. The difference in the slit widths of the spectrometers produce discrepancies in the sharpness of the measured peaks between absorption and emission. Also, the use of different setups causes different distributions of the \mathbf{k} vector at the entrance slit of the monochrometer, as does any misalignment with respect to the optical axis, introducing a spectral tilt in the measured spectra. When the same or very similar setups were used ([3], [40]) better agreement was found.

For all the samples studied here, the rms deviation was less than 5%, and for the Er transition at 1550 nm, is less than 1%, calculated across a wavelength interval where the noise was not significant. This confirms previously numerical results [47], that modeled this type of system for typical linewidths of rare earths in glass.

The good agreement found at room temperature for all samples suggests that the

McCumber theory is not restricted to crystalline hosts, but remains valid for the broader transitions of rare earth ions in glass.

More reliable comparison between the measured and the calculated spectra was achieved when the McCumber theory was applied to measured emission spectra, which were not affected by uncertainties in baseline selection. We can actually conclude that if the fluorescence spectrum has enough signal-to-noise ratio, the absorption spectra calculated using the McCumber theory can be more reliable than the absorption spectra that are measured experimentally.

The theory of McCumber was further tested at low temperature, by applying it to ground state transitions of Nd in fluorozirconate and silicate glasses. First we studied numerically the expected distortions introduced by the two types of spectral broadening, by simulating simple situations at temperatures close to the ones used in our experiments. As the homogeneous broadening becomes very small at temperatures of ~ 150 K, the effect on the McCumber calculated lineshape was expected to be small within the limits of the spectral transition, although it may become significant at some distance (~ 500 cm^{-1} for 12.5 cm^{-1} spectral width) from the peak. Inhomogeneous broadening is predominant at this temperature, introducing a more localized distortion, mostly within the spectral transition. The calculated emission lineshape presents a rise in the low energy side of the peak, lower values at the high energy side and a peak shift which depends on the spectral width.

The experimental results obtained on both samples confirm the overall trend anticipated by the numerical predictions, showing a type of distortion similar to that introduced by a set of Gaussian functions, of different FWHM that are not negligible when compared to the value of $k_B T$. The long wavelength side of the calculated emission spectra were more amplified and the short energy side was less amplified, compared to the measured emission cross section. The observed amplification was larger than un-

certainties in baseline subtraction, fluorescence reabsorption or exact knowledge of the sample temperature. The same behavior was observed when comparing the absorption spectra.

A quantitative analysis of the McCumber relation and the distortion function (difference between the McCumber and the actual emission cross sections) for a single Lorentzian or Gaussian peak, revealed very valuable relations regarding the determination of the homogeneous and inhomogeneous linewidths from measuring the peak shift, or the positions of the critical points (maxima and minima) of the distortion function. The analysis can be extended to describe multiple peak lines, and more modeling is required in this direction.

The spectral shape of the measured emission and absorption cross sections at 132 K in Nd:fluorozirconate glass were simulated by a set of Gaussian and Lorentzian functions (6 for emission, 8 for absorption spectra) and the spectra calculated from the simulated curves were compared with the ones calculated from experimental data. The emission spectrum described by 6 Gaussian peaks generates a better fit to the experimental absorption spectrum than does a Lorentzian fit, which gave tails in the amplified region of the spectrum which were too large. The 8 Gaussian functions used to simulate the absorption spectrum, however, gave very similar results as the 8 Lorentzian peaks, which may be explained by the less resolved peaks at the short energy side of the absorption spectrum, which allows an increased number of fitting combinations. In this case of fitting the measured absorption spectra, using either Gaussian or Lorentzian fits gave equally good agreement between emission spectra that is measured and emission spectra that is calculated from the fitted absorption curves.

We also simulated the room temperature situation of the same transition, by fitting the emission spectra with a set of 6 Voigt functions. As already expected, the calculated spectra from simulated and measured cross sections are in excellent agreement with

each other and with the measured spectra. This confirms one more time the validity of the McCumber theory at room temperature, also that the distortions observed at low temperature are a break down of the McCumber theory, due to the amplification caused by the large $\Delta\nu_{IH}/k_B T$ factor.

7.2 Future directions

Several things can be improved regarding the experimental design used for low temperature measurements:

First of all the chamber can be better isolated from the room air, so that air moisture does not produce ice on the surface of the sample. This was causing difficulties in the measurements, by generating more scattered light, poorer signal-to-noise ratio due to attenuation of the transmitted signal and reduced averaging caused by long time instabilities, due to increased accumulations during the day.

Also, the insulation of the sample holder can be improved, so lower temperatures can be achieved.

The temperature of the sample can be controlled better by adding a small heater to the sample holder, through which a small current can run.

However, to achieve much lower temperatures, a major change in the experimental design would be required, involving vacuum chambers and eventually cooling with He.

The low temperature measurements should be continued on some other rare earth doped samples, especially Er in silicate and fluorozirconate glasses. Er transitions are well separated spectrally from each other and they present a less complicated baseline subtraction, due to less overlapping of different transitions. Also, there will be less scattered light affecting the emission spectra.

The equations in section (6.4), that allow the determination of the spectral broad-

ening based on measurements of the peak shifts and position of the critical points can be generalized to include the effect of other peaks. Some approximations can be made about the complexity of the spectral line, regarding both the different spectral widths of the peaks and the position of the minima and maxima of the distortion function with respect to the distance from the peak that generates them. As the location of the critical points is affected by renormalizations done on the compared spectra, attention should be paid to the measured positions with respect to the peak value.

After these low temperature systems are explored from the point of view of the McCumber theory, the same experiments can be performed at high temperature, where the effect of homogeneous broadening can be investigated. The distortion produced by homogeneous broadening is more dramatic than the distortion due to inhomogeneous broadening, and by increasing the temperature by ~ 200 K from the room temperature, we can produce an increase of the homogeneous width from $\sim 50 \text{ cm}^{-1}$ to $\sim 140 \text{ cm}^{-1}$, causing a significant distortion both within the spectral range of the line, and at short distance (few hundred cm^{-1}) from the peak. Also measurable shifts in the peak will be observed, of about 8 cm^{-1} . The experimental system for these measurements would be somewhat less critical and less problems shall be encountered regarding the alignment and the stability of measurements compared with the low temperature setup.

Appendix A

Time-dependent perturbation theory. Absorption and stimulated emission transition rates.

This chapter presents a series of mathematical steps needed in the proper elucidation of the interaction between a quantum system and the electromagnetic field. The interaction can be between the electric dipole moment of the system and the oscillating electric field, or between the magnetic dipole moment and the oscillating magnetic field of the radiation. For most cases, the magnetic dipole interaction is about 5 orders of magnitude weaker, and it does not contribute to the emission process significantly. We will show this at the end of this chapter, by comparing the stimulated emission rates for the two types of interaction.

A.1 Electric Dipole Interaction

Consider a quantum system (isolated atom) interacting with an oscillating electric field $\mathbf{E}(\mathbf{r}, t) = \mathbf{E}_0 \sin(\omega t)$. It is assumed that the electric field has constant amplitude across the atom (which is true for all visible or infrared radiations where the wavelength of the radiation (≥ 500 nm) is much larger than the size of the atom $a_0 \sim 0.5$ nm). The hamiltonian of the system can be written as

$$\hat{H}(\mathbf{r}, t) = \hat{H}_0(\mathbf{r}) + \hat{V}(\mathbf{r}, t) \quad (\text{A.1})$$

where $H_0(\mathbf{r})$ is the time independent hamiltonian of the atom in the absence of the perturbation, and $V(\mathbf{r}, t)$ is the interaction hamiltonian. Assuming that the interaction hamiltonian is small compared to the hamiltonian of the unperturbed system we can apply the first order perturbation theory to determine the transition rates between any two quantum states of the system.

The time evolution of the wavefunction $\psi(\mathbf{r}, t)$ of the system is described by the *time-dependent* Schrodinger equation

$$i\hbar \frac{\partial \psi(\mathbf{r}, t)}{\partial t} = \hat{H}(\mathbf{r})\psi(\mathbf{r}, t) \quad (\text{A.2})$$

First, we solve the Schrodinger equation for the system in the absence of the perturbation. As \hat{H}_0 is independent of time, we can use the technique of separation of variables assuming a solution of the form

$$\psi(\mathbf{r}, t) = \phi(\mathbf{r})T(t) \quad (\text{A.3})$$

Introducing this in Eq.(A.2), we obtain

$$\frac{\hat{H}_0(\mathbf{r})\phi(\mathbf{r})}{\phi(\mathbf{r})} = \frac{i\hbar}{T(t)} \frac{dT(t)}{dt} \equiv E = \text{constant} \quad (\text{A.4})$$

The side containing the \mathbf{r} dependence is the *time-independent* Schrodinger equation and gives the eigenfunctions and eigenvalues (allowed states and energies) of the system in

the initial state.

$$\hat{H}_0(\mathbf{r})\phi_n(\mathbf{r}) = E_n\phi_n(\mathbf{r}) \quad (\text{A.5})$$

The other term gives the evolution in time of the form

$$T(t) = ae^{-iE_nt/\hbar} \quad (\text{A.6})$$

where a is a constant of integration, independent of time. The eigensolution of the time-dependent Schrodinger equation for the unperturbed system can then be written as

$$\psi_n(\mathbf{r}, t) = a_n\phi_n(\mathbf{r})e^{-iE_nt/\hbar} \quad (\text{A.7})$$

The state of the system in the absence of the electromagnetic field is a superposition of all eigenstates

$$\psi(\mathbf{r}, t) = \sum_n a_n\phi_n(\mathbf{r})e^{-iE_nt/\hbar} \quad (\text{A.8})$$

If the perturbation $\hat{V}(\mathbf{r}, t)$ is present, the solution to the Schrodinger equation can be found by assuming time dependent coefficients $a_n(t)$. The state can therefore be expanded as

$$\psi(\mathbf{r}, t) = \sum_n a_n(t)\phi_n(\mathbf{r})e^{-iE_nt/\hbar} \quad (\text{A.9})$$

The probability that at the time t the system is found in the state $\psi_k(\mathbf{r}, t)$ is given by the coefficients $|a_k(t)|^2$. They satisfy the normalization relation $\sum |a_n(t)|^2 = 1$.

Substituting Eq.(A.9) into the equation Eq.(A.2), and taking into account the fact that $\phi_n(\mathbf{r})$ are eigenfunctions of $\hat{H}_0(\mathbf{r})$, we obtain

$$\sum_n i\hbar \left(\frac{da_n(t)}{dt} \right) \phi_n(\mathbf{r})e^{-iE_nt/\hbar} = \sum_n a_n(t)\hat{V}(\mathbf{r}, t)\phi_n(\mathbf{r})e^{-iE_nt/\hbar} \quad (\text{A.10})$$

Operating from the left with $\int \phi_k^*(\mathbf{r})d\mathbf{r}$ gives

$$i\hbar \left(\frac{da_k(t)}{dt} \right) = \sum_n a_n(t)e^{-i(E_n - E_k)t/\hbar} \int \phi_k^*(\mathbf{r})\hat{V}(\mathbf{r}, t)\phi_n(\mathbf{r})d\mathbf{r} \quad (\text{A.11})$$

where $d\mathbf{r}$ is the differential of volume. We have also used the orthogonality of the wavefunctions for a Hermitian operator $\int \phi_k^*(\mathbf{r})\phi_n(\mathbf{r})d\mathbf{r} = \delta_{kn}$ (Dirac operator). Writing the matrix elements of the interaction hamiltonian as

$$V_{kn}(t) = \int \phi_k^*(\mathbf{r})\hat{V}(\mathbf{r}, t)\phi_n(\mathbf{r})d\mathbf{r} \quad (\text{A.12})$$

and the coupling frequency $\omega_{kn} = (E_k - E_n)/\hbar$, we can rewrite Eq.(A.11) in a more compact form

$$i\hbar \left(\frac{da_k(t)}{dt} \right) = \sum_n a_n(t)V_{kn}(t)e^{i\omega_{kn}t} \quad (\text{A.13})$$

This is a series of differential equation that allow us to calculate the coefficients $a_k(t)$ if the initial conditions are given. To proceed with our calculations, let's consider the simpler case of a two-level system with the energy levels E_k and E_l . Explicitly for the two states k and l , Eq.(A.13) can be written as

$$\begin{aligned} i\hbar \left(\frac{da_k(t)}{dt} \right) &= a_l(t)V_{kl}(t)e^{i\omega_{kl}t} + a_k(t)V_{kk}(t) \\ i\hbar \left(\frac{da_l(t)}{dt} \right) &= a_l(t)V_{ll}(t) + a_k(t)V_{lk}(t)e^{-i\omega_{kl}t} \end{aligned} \quad (\text{A.14})$$

Assume that initially the system is in the state $\psi_k(\mathbf{r}, t = 0)$. The coefficients for this state are $|a_k(0)|^2 = 1$ and $|a_l(0)|^2 = 0$.

The probability per unit time W_{kl} that the system undergoes a transition from state k to l ($k \neq l$) under the perturbation of the electromagnetic radiation is

$$W_{kl} = -\frac{d|a_k(t)|^2}{dt} = \frac{d|a_l(t)|^2}{dt} \quad (\text{A.15})$$

The transition can be either absorption if $E_k < E_l$ or stimulated emission otherwise. In order to calculate the induced transition rates, we need to determine an expression for $|a_k(t)|^2$.

No approximations have been made up to this point. We now apply the first order perturbation theory, assuming that the coefficients $a_k(t)$ and $a_l(t)$ do not change

significantly from their initial values due to the weak interaction hamiltonian $\hat{V}(\mathbf{r}, t) \ll \hat{H}_0(\mathbf{r})$, so $a_k(t) \simeq 1$ and $a_l(t)V \simeq 0$. Integrating each of the two equations (A.15) from 0 to t, we obtain

$$\begin{aligned} a_k(t) &= 1 + \frac{1}{i\hbar} \int V_{kk}(t) dt \\ a_l(t) &= \frac{1}{i\hbar} \int V_{lk}(t) e^{-i\omega_{kl}t} dt \end{aligned} \quad (\text{A.16})$$

These equations can be solved if the expression of the interaction potential $V(\mathbf{r}, t)$ is known. For electromagnetic radiation of frequency ω_0 , the interaction potential between the electric field $\mathbf{E}(\mathbf{r}, t)$ and the electric dipole of the atom $\mu_e(\mathbf{r})$ is given by

$$V(\mathbf{r}, t) = \mathbf{E}(\mathbf{r}, t) \cdot \mu_e(\mathbf{r}) \quad (\text{A.17})$$

where the electric field $\mathbf{E}(\mathbf{r}, t) = \mathbf{E}_0 \sin(\omega_0 t)$. Separating the time dependence by introducing the potential $V_0(\mathbf{r}) = \mathbf{E}_0 \cdot \mu_e(\mathbf{r})$, we can write the matrix elements $V_{lk}(t) = V_{lk}^0 \sin(\omega_0 t)$. The coefficient $a_l(t)$ becomes

$$a_l(t) = \frac{V_{kl}^0}{i\hbar} \int \sin(\omega_0 t) e^{-i\omega_{kl}t} dt \quad (\text{A.18})$$

Substituting $\sin(\omega_0 t)$ by $(e^{i\omega_0 t} - e^{-i\omega_0 t})/2i$ and integrating from 0 to t, Eq.(A.18) becomes

$$a_l(t) = -\frac{V_{kl}^0}{2\hbar} \left[\frac{e^{i(\omega_0 - \omega_{kl})t} - 1}{\omega_0 - \omega_{kl}} + \frac{e^{-i(\omega_0 + \omega_{kl})t} - 1}{\omega_0 + \omega_{kl}} \right] \quad (\text{A.19})$$

From this equation we can conclude that the atom interacts with the electromagnetic field only if the frequency of the field is very close to the coupling frequency of two states of the atom. Those frequencies of the field that bring a significant contribution to $a_l(t)$ is $\omega_0 = \pm \omega_{kl}$. If $\omega_0 \simeq +\omega_{kl}$, then $E_k > E_l$, which means that the electric field perturbs the system to decay to a lower energy $E_l = E_k - \hbar\omega_0$ by emitting away the energy $\hbar\omega_0$. This process is the *stimulated emission* of radiation. For frequencies of the field $\omega_0 \simeq -\omega_{kl}$,

the system absorbs the energy $\hbar\omega_0$ to move to a higher energy state $E_l = E_k + \hbar\omega_0$. This is the *absorption* process, which has the same origins as the stimulated emission, one being the reverse of the other.

Since the equation (A.19) is symmetric in ω_{kl} , it is sufficient to pursue our further calculations for the case of stimulated emission where $\omega_0 = \omega_{kl}$ plus a small frequency mismatch $\Delta\omega$. In this case, the first term of the above equation is dominant and we can neglect the second one with respect to it. The probability of finding the atom in the state l at the time t is then

$$|a_l(t)|^2 = \frac{|V_{kl}^0|^2}{4\hbar^2} \left[\frac{\sin(\Delta\omega t/2)}{(\Delta\omega/2)} \right]^2 \quad (\text{A.20})$$

As the time increases, the probability that the atom is found in the state l becomes larger. In the limits of $t \rightarrow \infty$, the value of the peak at $\Delta\omega=0$ is $(V_{kl}^0/4\hbar^2)t^2 \rightarrow \infty$. Making use of the delta-function representation [73]

$$\delta(\Delta\omega) = \frac{2}{\pi} \lim_{t \rightarrow \infty} \frac{\sin^2(\Delta\omega t/2)}{(\Delta\omega^2 t)} \quad (\text{A.21})$$

we can write

$$|a_l(t)|^2 = \frac{\pi}{2\hbar^2} |V_{kl}^0|^2 t \delta(\Delta\omega) \quad (\text{A.22})$$

The induced transition rate can then be written as

$$W_{kl} = \frac{d}{dt} |a_l(t)|^2 = \frac{\pi}{2\hbar^2} |V_{kl}^0|^2 \delta(\Delta\omega) \quad (\text{A.23})$$

The transition probability rate is described by a delta function, being infinite if the frequency of the field coincides with the atomic frequency and is zero otherwise. This does not correspond to a physical situation and we will replace the delta-function with the lineshape function $g(\Delta\omega)$ in our later calculations.

The last step in determining the expression of the induced transition rate is writing explicitly the time-independent part of the interaction hamiltonian $\hat{V}_0(\mathbf{r})$. From

Eq.(A.17) and Eq.(A.12) we can write the matrix elements of $\hat{V}_0(\mathbf{r})$ as

$$V_{kl}^0 = \mathbf{E}_0 \cdot \int \phi_k^*(\mathbf{r}) \hat{\mu}_e(\mathbf{r}) \phi_l(\mathbf{r}) d\mathbf{r} = |\mathbf{E}_0| |\mu_{kl}^e| \cos\theta \quad (\text{A.24})$$

where $|\mu_{kl}^e|$ is the amplitude of the matrix element μ_{kl}^e of the electric dipole operator between the states k and l , and θ is the angle between the axis of the electric dipole and the direction of the electric field.

As mentioned in the beginning of this section, the size of the atom is small compared to the wavelength of the field. It is appropriate not only to assume constant field amplitude across the atom, but also that a number of atoms¹ with different dipole orientations interact with an electric field of constant amplitude. Averaging over all possible orientations of the electric dipole moment we can write the $|V_{kl}^0|_{ave}^2$ as

$$|V_{kl}^0|_{ave}^2 = |\mathbf{E}_0|^2 |\mu_{kl}^e|^2 \left(\cos^2\theta \right)_{ave} = |\mathbf{E}_0|^2 |\mu_{kl}^e|^2 \frac{1}{3} \quad (\text{A.25})$$

where the average of $\cos^2\theta$ is $1/3$ for random distribution of the dipole orientation in space². With this, the induced transition rate for the *electric dipole interaction* becomes

$$W_{kl}^{el} = \frac{\pi}{6\hbar^2} |\mathbf{E}_0|^2 |\mu_{kl}^e|^2 \delta(\Delta\omega) \quad (\text{A.26})$$

The induced probability rate for a transition $k \rightarrow l$ depends on the amplitude of the electric field, the the amplitude of the matrix elements of the electric dipole moment for the states k and l and the frequency mismatch $\delta(\Delta\omega)$ between the frequency ω_0 of the radiation field and the atomic frequency ω_{kl} .

¹The ratio of the visible light wavelength to the size of atom $\sim 500\text{nm}/0.5\text{nm} = 10^3$, at least for few percent of the atoms the amplitude of the field is constant (also see ref. [69])

²integrating over the solid angle $\int_0^\pi \cos^2\theta \sin\theta d\theta \int_0^{2\pi} d\phi / \int_0^\pi \sin\theta d\theta \int_0^{2\pi} d\phi = 1/3$, where here θ and ϕ represent the spherical coordinates

A.2 Magnetic Dipole Interaction

If we consider the interaction between the magnetic dipole moment $\mu_m(\mathbf{r})$ of the atom and the oscillating magnetic field $\mathbf{B}(\mathbf{r}, t) = \mathbf{B}_0 \sin(\omega t)$ of the electromagnetic radiation, the interaction potential is given by a relation similar to Eq.(A.17)

$$V_{mag}(\mathbf{r}, t) = \mathbf{B}(\mathbf{r}, t) \cdot \mu_m(\mathbf{r}) \quad (\text{A.27})$$

We can repeat all our calculations exactly the same way and obtain for the *magnetic dipole interaction* an induced transition rate W_{kl}^{mag} equal to

$$W_{kl}^{mag} = \frac{\pi}{6\hbar^2} |\mathbf{B}_0|^2 |\mu_{kl}^m|^2 \delta(\Delta\omega) \quad (\text{A.28})$$

We can calculate the ratio between the two transition rates by dividing Eq.(A.26) to Eq.(A.28)

$$\frac{W_{kl}^{el}}{W_{kl}^{mag}} = \frac{|\mathbf{E}_0|^2 |\mu_{kl}^e|^2}{|\mathbf{B}_0|^2 |\mu_{kl}^m|^2} \quad (\text{A.29})$$

For an atom with a radius equal to Bohr radius $a_0 \simeq 5.3 \times 10^{-11}\text{m}$ and possesing a magnetic dipole moment equal to the Bohr magneton $\mu_B = 9.3 \times 10^{-24} \text{ Am}^2$ we can assume $|\mu_{kl}^e| \approx ea_0$ and $|\mu_{kl}^m| \approx \mu_B$. Also for a monochromatic plane wave in vacuum, $|\mathbf{E}_0|^2/|\mathbf{B}_0|^2 = c^2$. With this the ratio becomes

$$\frac{W_{kl}^{el}}{W_{kl}^{mag}} = \left(\frac{cea_0}{\mu_B} \right)^2 \simeq 7.5 \times 10^4 \approx 10^5 \quad (\text{A.30})$$

We conclude from here that the magnetic dipole interaction contributes to the emission process only when the electric dipole interaction is very weak, or for *forbidden electric-dipole transitions*. As this is the case for some transitions in rare earth ions, the magnetic dipole interaction cannot be totally neglected from our treatment.

Bibliography

- [1] C. R. Giles, and E. Desurvire, "Modeling erbium-doped fiber amplifiers," *J. Lightwave Technol.*, **9**, 271 (1991).
- [2] E. Desurvire, *Erbium-Doped Fiber Amplifiers: Principles and Applications*. New York: Wiley, (1994)
- [3] R. E. Tench, and M. Shimizu, "Fluorescence-Based Measurement of $g^*(\lambda)$ for Erbium-Doped Fluoride Fiber Amplifiers," *J. Lightwave Technol.*, **15**, 1559 (1997).
- [4] S. A. Payne, J. A. Caird, L. L. Chase, L. K. Smith, N. D. Nielsen, and W. F. Krupke, "Spectroscopy and gain measurements of Nd^{3+} in SrF_2 and other fluoride-structure hosts," *J. Opt. Soc. Amer. B*, 726, (1991).
- [5] B. N. Samson, P. A. Tick, and N. F. Borrelli "Efficient neodymium-doped glass-ceramic fiber laser and amplifier", *Opt. Lett.*, **26**, 145, (2001).
- [6] H. Zech, "Measurement technique for the quotient of the cross sections $\sigma_e(\lambda_s)/\sigma_a(\lambda_s)$ of erbium doped fibers", *IEEE Photon. Technol. Lett.*, **7**, 986, (1995).
- [7] W. M. Martin, and D. Milam, "Gain Saturation in Nd:Doped Laser Materials", *IEEE J. Quantum Electron.*, **QE-18**, 1155, (1982).
- [8] R. D. Muro, "The Er^{3+} -Fiber Gain Coefficient Derived from a Dynamic Gain Tilt Technique," *J. Lightwave Technol.*, **18**, 343 (2000).

- [9] S. D. Agger, and J. H. Povlsen, "Emission and absorption cross sections of thulium doped silica fibers", *Opt. Express*, **14**, 50, (2005)
- [10] M. P. Singh, D. W. Oblas, J. O. Reese, W. J. Miniscalco, and T. Wei, 'Measurement of the spectral dependence of absorption cross section for erbium-doped single-mode fiber", *Symposium on Optical Fiber Measurements*, Boulder, CO, NIST Special Publication, **792**, 93, (1990)
- [11] B. R. Judd, "Optical absorption intensities of rare earth ions", *Phys. Rev.*, **127**, 750, (1962)
- [12] G. S. Ofelt, "Intensities of crystal spectra of rare earth ions," *J. Chem. Phys.*, **37**, 511, (1962)
- [13] W. F. Krupke, "Induced-Emission Cross Sections in Neodymium Laser Glasses", *IEEE J. Quantum Electron.*, **QE-10**, 450, (1974).
- [14] R. R. Petrin, M. L. Kliewer, J. T. Beasley, R. C. Powell, I. D. Aggarwal, R. C. Ginther, "Spectroscopy and Laser Operation of Nd:ZBLAN Glass", *IEEE J. Quantum Electron.*, **27**, 1031 (1991)
- [15] M. J. Weber, "Spontaneous Emission Probabilities and Quantum Efficiencies for Excited States of Pr^{3+} in LaF_3 ", *J. Chem. Phys.*, **48**, 4774 (1964)
- [16] P. Goldner, and F. Auzel, "Application of standard and modified Judd-Ofelt theories to a praseodymium-doped fluorozirconate glass," *J. Appl. Phys.*, **79**, 7972, (1996)
- [17] W. T. Carnall, P. R. Fields, and K. Rajnak, "Spectral Intensities of the Trivalent Lanthanides and Actinides in Solution" *J. Chem. Phys.*, **49**, 4412, (1968)

- [18] R. S. Quimby, and W. J. Miniscalco, "Modified Judd-Ofelt technique and application to optical transitions in Pr^{3+} -doped glass," *J. Appl. Phys.*, **75**, 623, (1994)
- [19] M. J. Weber, T. E. Varitimos, and B. H. Matsinger, "Optical Intensities of Rare-Earth Ions in Yttrium Orthoaluminate", *Phys. Rev. B*, **8**, 47, (1973)
- [20] W. J. Miniscalco, *Rare Earth Doped Fiber Lasers and Amplifiers*, New York: Marcel Dekker, Inc., p.33., (1993)
- [21] C. Gorrller-Walrand and K. Binnemans, *Handbook on the physics and chemistry of rare earths*, Elsevier Science, **25** 167 (1998)
- [22] J. A. Caird, W. T. Carnal, and J. P. Hessler, *J. Chem. Phys.*, **74**, 3225 (1981)
- [23] W. Seeber, E. A. Downing, L. Hesselink, M. M. Fejer, and D. Ehrt, *J. Non-Cryst. Solids*, **189**, 218 (1995)
- [24] P. Goldner, "Accuracy of the Judd-Ofelt theory," *Molecular Physics*, **101**, 903, (2003)
- [25] P. H. Sarkies, J. N. Sandoe, and S. Parke, "Variations of Nd^{3+} cross section for stimulated emission with glass composition", *J. Phys. D: Appl. Phys.*, **4**, (1971).
- [26] J. N. Sandoe, P. H. Sarkies and S. Parke, *Variation of Er^{3+} cross section for stimulated emission with glass composition*, *J. Phys. D: Appl. Phys.*, **5**, (1972).
- [27] J. Wilson, and J. F. B. Hawkes, *Optoelectronics: An Introduction*, Pretience-Hall, p. 429, (1983)
- [28] P. R. Morkel, and R. I. Laming, "Theoretical modeling of erbium-doped fiber amplifiers with excited state absorption", *Opt. Lett.*, **14**, 1062 (1989)

- [29] K. Dybdal, N. Bjerre, J. E. Pedersen,C. C. Larsen, "Spectroscopic properties of Er-doped silica fibers and performs", *Proc. SPIE*, **1171**, 209 (1990)
- [30] W. L. Barnes, R. I. Laming, P. R. Morkel, and E. J. Tarbox, "Absorption-emission cross-section ratio for Er^{3+} doped fibers at $1.5\mu m$," *Proc. CLEO 1990*, Optical Society of America, Washington, D.C., **7**, 50, (1990)
- [31] W. J. Miniscalco, and R. S. Quimby, "General procedure for the analysis of Er^{3+} cross sections", *Optics Letters*, **16**, 258, (1991)
- [32] J. A. Lazaro, J. A. Valles, and M. A. Rebollo, "In Situ Measurement of Absorption and Emission Cross Sections in Er^{3+} -Doped Waveguides for Transitions Involving Thermalized States", *IEEE J. Quantum Electron.*, **35**, 827 (1999)
- [33] B. F. Aull and H. P. Jenssen, "Vibronic Interaction in Nd:YAG Resulting in Nonreciprocity of Absorption and Stimulated Emission Cross Sections", *IEEE J. Quantum Electron.*, Vol. QE-18, 925-930 (1982)
- [34] L. D. DeLoach, S. Payne, L. L. Chase, L. K. Smith, W. L. Kway, and W. Krupke, "Evaluation of Absorption and Emission Properties of Yb^{3+} Doped Crystals for Laser Applications", *IEEE J. Quantum Electron.*, **29**, 1179, (1993)
- [35] V. Sudesh, J. A. Piper, E. M. Goldys and R. S. Seymour, "Growth, characterization and laser potential of $Tm : La_2Be_2O_5$ ", *J. Opt.Soc. Am. B*, **15**, 239 (1998)
- [36] D. E. McCumber, "Theory of Phonon-Terminated Optical Masers", *Phys. Rev.*, **134**, A299 (1964)

- [37] M. C. Williams, and R. T. Brundage, "Stimulated-emission cross sections and nonradiative relaxation of the 5L_6 state of trivalent americium in fluorozirconate glass", *Phys. Rev. B*, **45**, 4561 (1992)
- [38] H. M. Pask, R. J. Carman, D. C. Hanna, A. C. Tropper, C. J. Mackechnie, P. R. Barber, and J. M. Dawes, "Ytterbium-Doped Silica Fiber Lasers: Versatile Sources for the 1-1.2 μm Region", *IEEE J. Sel. Topics Quant. Electron.*, **1**, 2 (1995)
- [39] C. Florea, K. A. Winick, "Ytterbium-Doped Glass Waveguide Laser Fabricated by Ion Exchange", *J. Lightwave Technol.*, **17**, 1593 (1999)
- [40] D. J. Coleman, S. D. Jackson, P. Golding and T. A. King, "Measurements of the spectroscopic and energy transfer parameters for Er^{3+} -doped and Er^{3+} , Pr^{3+} -codoped $\text{PbO} - \text{Bi}_2\text{O}_3 - \text{Ga}_2\text{O}_3$ glasses", *J. Opt. Soc. Am. B*, **19** (2002)
- [41] T. Y. Fan, M. R. Kotka, "End-Pumped $\text{Nd} : \text{LaF}_3$ and $\text{Nd} : \text{LaMgAl}_{11}\text{O}_{19}$ Lasers", *IEEE J. Quantum Electron.*, **25**, 1845 (1989)
- [42] C. Huang, L. McCaughan and D. M. Gill, "Evaluation of Absorption and Emission Cross Sections of Er-Doped LiNbO_3 for Applications to Integrated Optic Amplifiers", *J. Lightwave Technol.*, **12**, 803 (1994).
- [43] T. Schweizer, D. W. Hewak, B. N. Samson and D. N. Payne, "Spectroscopic data of the 1.8-, 2.9-, and 4.3- μm transitions in dysprosium-doped gallium lanthanum sulfide glass", *Opt. Lett.*, **21**, 1594 (1996)
- [44] T. Schweizer and B. N. Samson, "Infrared emission and ion-ion interaction in thulium- and terbium-doped gallium lanthanum sulfide glass" *J. Opt. Soc. Am. B*, **16**, 308, (1999)

- [45] J. F. Philipps, T. Topfer, H. Ebendorff-Heidepriem, D. Ehrt, R. Sauerbrey, "Spectroscopic and lasing properties of $Er^{3+} : Nd^{3+}$ -doped fluoride phosphate glasses", *Appl. Phys. B*, **72**, 399 (2001)
- [46] D. E. McCumber, "Einstein Relations Connecting Broadband Emission and Absorption Spectra", *Phys. Rev.*, **136**, A954 (1964)
- [47] R. S. Quimby, "Range of validity of McCumber theory in relating absorption and emission cross sections", *J. Appl. Phys.*, **92**, (2002)
- [48] M. J. F. Digonnet, E. Murphy-Chutorian, and D. G. Falquier, "Fundamental Limitations of the McCumber Relation Applied to Er-Doped Silica and Other Amorphous-Host Lasers", *IEEE J. Quantum Electron.*, **38**, 1629 (2002)
- [49] S. A. Payne, L. L. Chase, L. K. Smith, W. L. Kway, and W. F. Krupke, "Infrared Cross section Measurements for Crystals Doped with Er^{3+} , Tm^{3+} , and Ho^{3+} ", *IEEE J. Quantum Electron.*, **28**, 2619 (1992)
- [50] B. M. Walsh, N. P. Barnes, and B. Di Bartolo, "Branching ratios, cross sections, and radiative lifetimes of rare earth ions in solids: Application to Tm^{3+} and Ho^{3+} ions in $LiYF_4$ ", *J. Appl. Phys.*, **83**, 2772 (1998)
- [51] X. Feng, S. Tanabe, and T. Hanada, "Spectroscopic properties of erbium-doped ultraphosphate glasses for $1.5 \mu m$ amplification", *J. Appl. Phys.*, **89**, 3560 (2001)
- [52] J. Sun, J. Zhang, Y. Juo, J. Lin, and H. Song, "Spectral components and their contributions to the $1.5 \mu m$ emission bandwidth of erbium-doped oxide glass", *J. Appl. Phys.*, **94**, 1325 (2003)

- [53] P. M. Krummrich, "Experimental determination of the emission cross-section spectrum of the pump transition of praseodymium", *IEEE Photon. Technol. Lett.*, **7**, 62 (1995)
- [54] R. I. Epstein, J. J. Brown, B. C. Edwards, and A. Gibbs, "Measurements of optical refrigeration in ytterbium-doped crystals", *J. Appl. Phys.*, **90**, 4815 (2001)
- [55] R. S. Quimby, *Photonics and Lasers: An Introduction*, John Wiley & Sons, (2006)
- [56] M. J. F. Digonnet, "Rare-earth-doped fiber lasers and amplifiers", Marcel Dekker (2001)
- [57] H. Kroemer, *Quantum Mechanics for Engineering, Material Science, and Applied Physics*, Prentice Hall, Englewood Cliffs, New Jersey p.492, (1994)
- [58] W.B. Fowler, D. L. Dexter, "Relation between Absorption and Emission Probabilities in Luminescent Centers in Ionic Solids", *Phys., Rev.* **128**, 2154 (1962)
- [59] R. S. Quimby, *Active Phenomena in Doped Halide Glasses in fluoride Glass Fiber Optics*, ed. I. D. Aggarwal and G. Lu, Boston : Academic Press, Harcourt Brace Jovanovich, p.363, (1991)
- [60] M. D. Shinn, W. A. Sibley, M. G. Drexhage, and R. N. Brown, "Optical transitions of Er^{3+} ions in fluorozirconate glass", *Phys., Rev. B*, **27**, 6635 (1983)
- [61] J. M. Pellegrino, W. M. Yen, and M. J. Weber, "Composition dependence of Nd^{3+} homogeneous linewidths in glasses" *J. Appl. Phys.*, **51**(12), 6332 (1980)
- [62] G. S. Dixon, R. C. Powell, and X. Gang, *Phys., Rev. B*, **33**, 2713 (1986)
- [63] F. Durville, G. S. Dixon, and R. C. Powell, *J. Lumin.*, **36**, 221 (1987)

- [64] G. Lei, J. E. Anderson, M. I. Buchwald, B. C. Edwards, R. I. Epstein, "Determination of spectral linewidths by Voigt profiles in Yb^{3+} -doped fluorozirconate glasses," *Phys. Rev. B*, **57**, 7673 (1998)
- [65] W. T. Carnal, P. R. Fields, and K. Rajnak, "Electronic Energy Levels in the Trivalent Lanthanide Aquo Ions I.", *J. Chem. Phys.*, **49**, 4424 (1968)
- [66] W. T. Carnal, P. R. Fields, and K. Rajnak, "Electronic Energy Levels in the Trivalent Lanthanide Aquo Ions I.", *J. Chem. Phys.*, **49**, 4443 (1968)
- [67] W. T. Carnal, P. R. Fields, and K. Rajnak, *J. Chem. Phys.*, **49**, 4447 (1968)
- [68] W. T. Carnal, P. R. Fields, and K. Rajnak, *J. Chem. Phys.*, **49**, 4450 (1968)
- [69] O. Svelto, *Principles of Lasers*, Plenum Press, New York and London, p.30, (1998)
- [70] Gilway Technical Lamp, Engineering Catalog 169, www.gilway.com
- [71] R. N. Brown, and J. J. Hutta, "Material dispersion in high optical quality heavy metal fluoride glasses.", *Appl. Opt.*, **24**, 4500 (1985)
- [72] A. Jha, S. Shen, and M. Naftaly, "Structural origin of spectral broadening of $1.5-\mu m$ emission in Er^{3+} -doped tellurite glasses.", *Phys. Rev. B*, **62**, 6215 (2000)
- [73] R. L. Liboff, *Introductory Quantum Mechanics*, , p. 639, Holden-Day (1980)